

Development of Functional Slippery Liquid-Infused Porous Surfaces via Layer-by-Layer Method

August 2017

MANABE, Kengo

A Thesis for the Degree of Ph.D. in Engineering

Development of Functional Slippery Liquid-Infused Porous Surfaces via Layer-by-Layer Method

August 2017

Graduate School of Science and Technology
Keio University

MANABE, Kengo

Development of Functional Slippery Liquid-Infused Porous Surfaces via Layer-by-Layer Method

Abstract

Extensive research has been conducted to explore how the properties of biomimetic surfaces like mosquito eyes, lotus leaves, and shark skin could be used to create anti-fouling surface materials. The micro/nano-configuration of such biological structures is the source of their properties as it creates liquid-gas and solid-gas interfaces. Applications in both science and industry fields could benefit from such effective properties as antireflection, self-cleaning, antifouling, antifrosting, and anti-icing. However, the arduous endeavours that have been made have not managed so far to achieve a breakthrough in the development of surfaces that could repel low surface tension liquid, complex liquid, and others. To resolve various challenges, recent developments of bioinspired structures revealed slippery liquid-infused porous surfaces (SLIPS). The pitcher plant *Nepenthes* provided the inspiration for the development of an anti-fouling surface with superhydrophobicity known as SLIPS. An underlayer demonstrating hydrophobicity and porosity and lubricant oil constitute the components of this material. Presenting a nanostructure and low surface energy, the porous membrane promotes the formation of an inert slippery interface without instability or defects by permitting adherence of the impregnated lubricant. Herein, the present research demonstrates the following three functionalized SLIPS based on the functionalized underlayer via layer-by-layer self-assembly: slippery fluid-infused antireflective films, biocompatible slippery fluid-infused films composed of chitosan and alginate, and temperature-activated solid/liquid-infused nanofibrous films. These designed SLIPS present highly optical transparency, antithrombogenicity, and tunable transmittance/wettability, respectively. The results of this study suggest that the functionalized SLIPS would be valuable for innovative medical applications, solar panels, glasses, smart windows, and other devices.

Acknowledgements

This work was conducted in the group of Prof. Dr. Seimei Shiratori at Center for Material Design Science, School of Integrated Design Engineering, Graduate School of Science and Technology and at Department of Applied Physics and Physico-Informatics, Faculty of Science and Technology, Keio University. It was supported by the research grant of the Keio Leading-edge Laboratory of Science and Technology.

First of all, I would like to give my special thanks to Prof. Dr. Takaaki Ishigure and Prof. Dr. Daniel Citterio for reviewing my Ph.D. thesis. I would also like to thank Prof. Dr. Atsushi Hotta for kindly accepting to be the reviewer.

My deepest appreciation goes to Prof. Dr. Shiratori who provided me to spend six years in his lab and at Keio University. Without his kind help and supervision for all of my research, this dissertation could not have been achieved. I was always encouraged and motivated to solve various challenges, continue and finish the study all the time.

Special thanks also go to Dr. Yoshio Hotta, Dr. Kouji Fujimoto, and Dr. Kyu-Hong Kyung whose meticulous comments were an enormous help, helpful comments and suggestions to me. I am grateful to all members of the Shiratori lab – current and past, for being sources of inspiration for me.

Finally, I would also like to express my gratitude to my family, especially my mother, Ms. Yumiko Manabe and my father, Mr. Hideaki Manabe, for their moral support and warm encouragements. They are always supportive of my path in life.

Table of Contents

ACKNOWLEDGEMENTS

LIST OF FIGURES

LIST OF TABLES

Chapter 1: Introduction	1
1.1 Overview	1
1.2 Research questions and hypotheses in each chapter	4
 Chapter 2: Literature Review	 7
2.1 Layer-by-Layer self-assembly method	7
2.1.1 Electrostatic Layer-by-Layer self-assembly method	7
2.1.1.1 Basic principles of polyelectrolytes	8
2.1.1.2 The concept of electrostatic Layer-by-Layer self-assembly	11
2.1.2 Hydrogen-bonding Layer-by-Layer self-assembly method	13
2.1.2.1 The basic principles of hydrogen-bonding assembly	13
2.1.2.2 Stabilization of hydrogen-bonding film	18
2.1.3 Porous structure via Layer-by-Layer self-assembly	19
2.2 Surface Wettability	22
2.2.1 Wetting Models	23
2.2.2 Superhydrophobicity	24
2.2.3 Liquid-Impregnated Surfaces (LIS)	25
2.2.4 Slippery Liquid-Infused Porous Surfaces (SLIPS)	25
 Chapter 3: Optically Functionalized SLIPS	 30
3.1 Background	30
3.2 Experiment	33
3.2.1 Materials	33

3.2.2 Chitin nanofibre preparation -----	33
3.2.3 Film with superhydrophilicity and antireflectivity -----	34
3.2.4 Film with superhydrophobicity and transparency -----	34
3.2.5 Slippery film with fluid infusion and antireflectivity -----	34
3.2.6 Characterization -----	35
3.2.7 Anti-frosting property test -----	35
3.3 Results and Discussion -----	36
3.3.1 Films with superhydrophilicity and antireflectivity -----	37
3.3.2 Film with transparency and superhydrophobicity -----	44
3.3.3 Slippery fluid-infused film with antireflectivity -----	47
3.3.4 Anti-frosting properties -----	47
3.4 Conclusions -----	50
 Chapter 4: SLIPS Enhanced Through Wettability -----	 51
4.1 Background -----	51
4.2 Experiment -----	53
4.2.1 Materials -----	53
4.2.2 Preparation of precursor film -----	54
4.2.3 Crosslinking -----	55
4.2.4 Elimination of PVPON -----	55
4.2.5 Hydrophobization and liquid infusion -----	55
4.2.6 Blood coagulation test -----	56
4.2.7 Characterization -----	56
4.3 Results and Discussion -----	57
4.3.1 Biodegradable porous underlayer for SLIPS -----	57
4.3.2 SLIPS applied criteria -----	67
4.3.3 Durability -----	71
4.3.4 Antithrombogenic properties -----	73
4.4 Conclusions -----	76

Chapter 5: Responsive SLIPS with Regulation of Optical Transparency and Wettability

-----	77
5.1 Background -----	77
5.2 Experiment -----	80
5.2.1 Materials -----	80
5.2.2 Chitin nanofibre refinement -----	81
5.2.3 Production of the mix of paraffin oil and liquid paraffin -----	82
5.2.4 TA-SLIPS development -----	82
5.2.5 Characterization -----	83
5.3 Results and Discussion -----	84
5.3.1 Porous (CHINF/PAA) underlayer -----	84
5.3.2 TA-SLIP surface wettability -----	91
5.3.3 Optical properties of TA-SLIPSs -----	97
5.3.4 TA-SLIPS reversible transparency and adhesion switching -----	104
5.4 Conclusions -----	105

Chapter 6: Conclusion and Implications ----- 106

6.1 Summary of findings -----	106
6.2 Future works -----	107

References ----- 109

List of Figures

Figure 1-1. Overview of dissertation structure.

Figure 2-1. Diagram showing how LbL is applied to charged solid substrates. From Ref [38]. Reprinted with permission from AAAS (Copyright 1997).

Figure 2-2. Complete pH matrix illustrating how the PAH/PAA bilayer contributes to the average increasing thickness in relation to the dipping solution pH. Reproduced with permission from Ref [39]. Copyright 2000 American Chemical Society.

Figure 2-3. Diagram showing how PVPON and PAA are constructed based on hydrogen-bonded LbL films. Reproduced from Ref [60] with permission of Springer (Copyright 2012).

Figure 2-4. Chemical configurations of the polymers used in self-assembly outlined in Table 2-1. Reproduced from Ref [45] with permission of Taylor & Francis (Copyright 2006).

Figure 2-5. Diagram showing non-permanent BCM/PMAA film swelling under the influence of temperature. Reproduced with permission from Ref [49]. Copyright 2009 American Chemical Society.

Figure 2-6. Cysteamine-functionalised PVPON and PMA used in the construction and crosslinking of hydrogen-bonded multilayer thin films. Reproduced with permission from Ref [54]. Copyright 2006 American Chemical Society.

Figure 2-7. SEM images showing the development of porous structures of (BPEI_{6.5}/PAA_{4.5})₃₀ films via staged acid treatment. The porous structures are shown magnified in the inset of each image. Low magnification images have a scale bar of 100 μm while high magnification images have a scale bar of 20 μm . Reproduced with permission from Ref [72]. Copyright 2013 American Chemical Society.

Figure 2-8. The surface of a 21-layer 3.5/7.5 polyelectrolyte multilayer film is shown in an AFM image prior to (a) and after (b) it was immersed in an acidic transition bath (pH = 2.5).

The films are respectively 950 and 2790 Å thick and have a refractive index of 1.54 and 1.18. Reproduced with permission from Ref [73]. Copyright 2000 American Chemical Society.

Figure 2-9. Cross-sectional SEM images and diagram illustrating the deduced formation process of polyelectrolyte films displaying porosity via phase separation triggered by reaction. Every image has a scale bar of 1 µm. Reproduced with permission from Ref [74]. Copyright 2016 American Chemical Society.

Figure 2-10. The phenomenon of wetting and the associated modes of hydrophobicity and hydrophilicity. Reproduced from Ref [77] with permission of Elsevier (Copyright 2009).

Figure 2-11. Young's, Wenzel's and Cassie-Baxter's equations (Nakajima, 2011); a liquid droplet is shown on a solid surface, with three interphases (γ) developing the contact angle (θ), namely, solid-liquid (SL), liquid-vapour (LV) and solid-vapour (SV). Fractional area f_1 with contact angle θ_1 and fractional area f_2 with θ_2 ($f_1 + f_2 = 1$) are the fractions constituting the rough surface in the Cassie-Baxter equation. Reproduced from Ref [78] with permission of Nature (Copyright 2011).

Figure 2-12. Schematic image of SLIPS composed of a hydrophobic underlayer and a lubricant layer. Reproduced from Ref [22] with permission of Nature (Copyright 2011).

Figure 2-13. Diagram of wetting architectures external to and beneath a drop (column 2). The sum of the individual interfacial energies gives the total interface energy per unit area (column 3). Column 4 indicates corresponding specifications for the stability of every configuration. "Oil" and "water" respectively represent the lubricant and the working fluid. Reproduced from Ref [26] with permission from The Royal Society of Chemistry (Copyright 2013).

Figure 3-1. Schematic representation of each of the three film types, namely, LbL assembly-based *moth-eye film* with antireflection and comprising CHINFs and SiO₂, and *lotus* and *pitcher films* with superhydrophobicity and lubricant infusion, respectively, developed based on functionalization of ten-bilayer *moth-eye film*. Reproduced with permission from Ref [106]. Copyright 2014 American Chemical Society.

Figure 3-2. Summary of empirical protocols and the characteristics of the three film types. Reproduced with permission from Ref [106]. Copyright 2014 American Chemical Society.

Figure 3-3. Ellipsometry-based measurement of superhydrophilic and anti-reflective films with varying numbers of bilayers and superhydrophobic film, with the thickness and refractive index of the films being indicated by the yellow bars and blue squares, respectively. Reproduced with permission from Ref [106]. Copyright 2014 American Chemical Society.

Figure 3-4. (A) Superhydrophilic and anti-reflective films imaged with FE-SEM on separate bilayers at 1 μm scale bar. (B) Zeta potential of CHINF solutions of varying pH. As cationic material, CHINF was intended to help SiO_2 nanoparticles to attach to the glass substrate but without coating them. Surface electrostatic bias occurred because of CHINF adherence to the glass substrate in some areas. As shown in the FE-SEM image of 1.0 bilayer of superhydrophilic and anti-reflective film, attachment of SiO_2 nanoparticles occurred in the areas with CHINF, while the FE-SEM image of 1.5 bilayer of superhydrophilic and anti-reflective film shows that next generation CHINF attached to the glass substrate without touching the SiO_2 nanoparticles. Reproduced with permission from Ref [106]. Copyright 2014 American Chemical Society.

Figure 3-5. (A) Superhydrophilic and anti-reflective films with varying numbers of bilayers and superhydrophobic film imaged with FE-SEM at 1 μm scale bar. (B) Ten-bilayer superhydrophilic and anti-reflective films (left) and glass substrate (right) imaged under fluorescent light. (C) Superhydrophilic and anti-reflective films with varying numbers of bilayers and superhydrophobic film with their surface roughness measured by RMS (R_q) and R_a , denoted by the yellow bars and blue squares, respectively; the equivalent AFM images are provided underneath. The scan size (x and y) and data scale (z) are 5 μm and 500 nm, respectively. Reproduced with permission from Ref [106]. Copyright 2014 American Chemical Society.

Figure 3-6. Transmittance changes of the fabricated films (left). Apart from slippery fluid-

infused film, optical simulation software (Design, Tecwave) was applied to determine transmittance modifications of every film with constant 1.23 refractive index (right). Transmittance in air was determined for the glass substrate (black line), superhydrophobic and anti-reflective films with two (red line), four (yellow line), six (lime green line), eight (green line) and ten (aqua line) bilayers, as well as for the superhydrophobic film (blue line) and slippery fluid-infused film (pink line). Reproduced with permission from Ref [106]. Copyright 2014 American Chemical Society.

Figure 3-7. Diagram showing modifications in refractive index on bare glass (A), moth-eye structure (B) and LbL film (C). Reproduced with permission from Ref [106]. Copyright 2014 American Chemical Society.

Figure 3-8. (A) Superhydrophobic film imaged with EDX at 1 μm scale bar. The graphs beneath indicate the contact angle, sliding angle and surface tension, respectively denoted by yellow and blue bars and red diamonds, of water, rapeseed oil, hexadecane and octane on a (B) hydrophobic film and (C) slippery fluid-infused film alongside images of all drops of liquid on the films. Reproduced with permission from Ref [106]. Copyright 2014 American Chemical Society.

Figure 3-9. Superhydrophilic and anti-reflective films with two (red bar), four (yellow bar), six (lime green bar), eight (green bar) and ten bilayers (aqua bar), superhydrophobic film (blue bar) and slippery fluid-infused film (pink bar) are shown with their total transmittance (T.T.), parallel transmittance (P.T.), diffusion (DIF) and haze (HAZE). Explanations for the optical values are provided on the right-hand side. DIF divided by T.T. gives the haze, which indicates how much light dispersal is caused by light passing through the films. Reproduced with permission from Ref [106]. Copyright 2014 American Chemical Society.

Figure 3-10. Glass substrate (G), ten-bilayer superhydrophilic film (M), superhydrophobic film (L), and slippery fluid-infused film (P) imaged photographically and via thermography. The time and temperature since activation of the Peltier cooling unit are indicated above the

images. The Peltier unit dictated the temperature. As indicated on the right-hand side, the experiment involved introducing the films in a thermo-hygrostat at 10°C and 80% relative humidity, with a gradual decline in temperature until -10°C. Upon reaching that level, the temperature was increased to 30°C. Reproduced with permission from Ref [106]. Copyright 2014 American Chemical Society.

Figure 4-1. Simplified representation of how non-fluorinated SLIPS with biodegradability and biocompatibility is created. Reproduced with permission from Ref [132]. Copyright 2015 American Chemical Society.

Figure 4-2. The red, orange, green and blue lines respectively represent the FT-IR spectra of the precursor film of chitosan/PVPON and alginate, a film after crosslinking, a film with porosity following removal of PVPON from the crosslinked film, and a film following PVPON removal from a film without crosslinking. Reproduced with permission from Ref [132]. Copyright 2015 American Chemical Society.

Figure 4-3. FT-IR spectra of the chitosan/PVPON/alginate film constituents, namely, chitosan, PVPON and sodium alginate powders. Reproduced with permission from Ref [132]. Copyright 2015 American Chemical Society.

Figure 4-4. C_{1s} core level spectra associated with the precursor film containing chitosan/PVPON and alginate (a); film with crosslinking (b); film with porosity following elimination of PVPON from the crosslinked film (c); and film following PVPON elimination from a film without cross-linking (d). The C-C peak is denoted by component_1, the C-O peak is denoted by component_2, the N-C=O peak is denoted by component_3 and the O=C-O peak is denoted by component_4. Reproduced with permission from Ref [132]. Copyright 2015 American Chemical Society.

Figure 4-5. FE-SEM imaging at a scale bar of 300 nm of precursor film containing chitosan/PVPON and alginate (left), film with crosslinking (centre), and film with porosity following elimination of PVPON from the crosslinked film (right). Reproduced with

permission from Ref [132]. Copyright 2015 American Chemical Society.

Figure 4-6. AFM images showing the precursor film containing chitosan/PVPON and alginate (left), film with crosslinking (centre), and film with porosity following elimination of PVPON from the crosslinked film (right). The scan size (x and y) and data scale (z) are respectively 3 μm and 100 nm. Reproduced with permission from Ref [132]. Copyright 2015 American Chemical Society.

Figure 4-7. Low magnification FEM-SEM imaging at 500 nm scale bar of a film demonstrating porosity following elimination of PVPON from the crosslinked film. Reproduced with permission from Ref [132]. Copyright 2015 American Chemical Society.

Figure 4-8. Ellipsometry analysis showing the thickness and refractive index, represented by yellow bars and blue squares, respectively, of the precursor films of chitosan/PVPON and alginate comprising varying mixture fractions (chitosan: PVPON vol.% of 25:75, 50:50, and 75:25), which are denoted by mix-LbL X: Y, crosslinked films, films with porosity following elimination of PVPON from the crosslinked films, and hydrophobized films with porosity (chitosan: PVPON, vol.% of 50:50). Reproduced with permission from Ref [132]. Copyright 2015 American Chemical Society.

Figure 4-9. Growth of films consisting of chitosan/alginate, PVPON/alginate, and chitosan/PVPON/alginate in varying mixture fractions (chitosan: PVPON vol.% of 25:75, 50:50, and 75:25). Reproduced with permission from Ref [132]. Copyright 2015 American Chemical Society.

Figure 4-10. Film transmittance variations: The black, red, yellow, green, blue, and pink lines are respectively indicative of the transmittance of a glass substrate, a precursor film comprising chitosan/PVPON and alginate (chitosan:PVPON vol.% of 50:50), a film with crosslinking, a film with porosity following PVPON elimination from the crosslinked film, a hydrophobized film with porosity, and a SLIPS with biocompatibility after oil was dropped on the hydrophobized film with porosity on glass substrates in an air medium. Reproduced with

permission from Ref [132]. Copyright 2015 American Chemical Society.

Figure 4-11. Total transmittance (T.T.), parallel transmittance (P.T.), diffusion (DIF) and haze (HAZE) associated with precursor film comprising chitosan/PVPON and alginate (chitosan: PVPON vol.% of 25:75, red bars; 50:50, yellow bars; 75:25, green bars), films with crosslinking (chitosan: PVPON vol.% of 25:75, blue bars; 50:50, dark blue bars; 75:25, pink bars), films with porosity following PVPON elimination from the crosslinked films (chitosan: PVPON vol.% of 25:75, purple bars; 50:50, orange bars; 75:25, lime green bars), a hydrophobized film with porosity (chitosan: PVPON vol.% of 50:50, light blue bars), and a SLIPS with biocompatibility after oil was dropped on the hydrophobized film with porosity (black bars). Reproduced with permission from Ref [132]. Copyright 2015 American Chemical Society.

Figure 4-12. The dark blue bars, light blue bars and red diamonds respectively represent the contact angle, sliding angle and surface tension of water, almond oil, and blood on hydrophobized film with porosity and SLIPS with biocompatibility created when almond oil was dropped on the hydrophobized film with porosity. Equivalent pictures of every liquid drop on each film are provided below. Reproduced with permission from Ref [132]. Copyright 2015 American Chemical Society.

Figure 4-13. Blood droplet on every surface, as imaged with the CCD camera. Reproduced with permission from Ref [132]. Copyright 2015 American Chemical Society.

Figure 4-14. The yellow bars and blue squares respectively show how the sliding angle of water and the total transmittance of a SLIPS with biocompatibility changed following growing exposure at room temperature. A haze meter was employed to determine the total transmittance, representing the parallel transmittance coupled with forward diffusion. Reproduced with permission from Ref [132]. Copyright 2015 American Chemical Society.

Figure 4-15. The sliding angle of water and blood, shown in blue and red, respectively, on the SLIPS with biocompatibility following 60 seconds of spinning at spin rates in the range 250-

6000 rpm. Reproduced with permission from Ref [132]. Copyright 2015 American Chemical Society.

Figure 4-16. The sliding angle of water and blood, shown in blue and red, respectively, on the SLIPS with biocompatibility following exposure under running water for a water flowing duration in the range 0.25-12 hours. The flow rate from a peristaltic pump (MP-1000, Tokyo Rikakikai Co., Ltd., Tokyo, Japan) was 0.32 ml/s through a water tube (inside diameter: 3.15 mm, outside diameter: 5.20 mm). Reproduced with permission from Ref [132]. Copyright 2015 American Chemical Society.

Figure 4-17. Digital microscopy imaging at a 10 μm scale bar showing how long it took for blood to coagulate on a glass substrate (first line), films with porosity following PVPON elimination from a crosslinked film (second line), a hydrophobized film with porosity (third line), and a biocompatible SLIPS after oil was dropped on the hydrophobized film with porosity (fourth line). Reproduced with permission from Ref [132]. Copyright 2015 American Chemical Society.

Figure 4-18. Pictures showing a droplet of blood on a SLIPS with biocompatibility (a), superior view following coagulation (b), superior view (c) and lateral view (d) following clot elimination from the biocompatible SLIPS. Reproduced with permission from Ref [132]. Copyright 2015 American Chemical Society.

Figure 4-19. Pictures showing how blood was repelled from the biocompatible SLIPS after it was dropped (left), as it was sliding (centre) and after it slid off (right). Reproduced with permission from Ref [132]. Copyright 2015 American Chemical Society.

Figure 5-1. Simplified representation of TA-SLIPS: CHINFs and PAA make up the porous underlayer developed through the method of LbL self-assembly; functionalization of the hydrophilic nanofibrous underlayer produced the hydrophobic underlayer, while introduction of the solidifiable/liquid paraffin in the hydrophobic nanofibrous membrane resulted in the super-slippery surface with temperature sensitivity. Reproduced with permission from Ref

[147]. Copyright 2016 American Chemical Society.

Figure 5-2. The porous underlayers with varying number of bilayers imaged with FE-SEM at 1 μm scale bar (first line), film thickness (second line) and refractive index (third line) as well as the porous underlayer showing hydrophobicity (first line). Ellipsometry was applied to determine the film thickness (D) and refractive index (n_l) across a 4×4 mm area. Reproduced with permission from Ref [147]. Copyright 2016 American Chemical Society.

Figure 5-3. Chitin nanofibres imaged with TEM. Reproduced with permission from Ref [147]. Copyright 2016 American Chemical Society.

Figure 5-4. DLS image showing the average particle diameter associated with every peak. Reproduced with permission from Ref [147]. Copyright 2016 American Chemical Society.

Figure 5-5. C_{1s} core-level spectra of the underlayer with porosity (a) pre- and (b) post-hydrophobization by DTMS. The initial intensity is denoted by the black line, C-C is denoted by the orange line, C-O is denoted by the grey line, O=C-O is denoted by the yellow line, sum is denoted by the blue line, and background peaks are denoted by the green line. (c) The orange and green bars and the blue diamonds respectively denote the contact angle, sliding angle and surface tension of water and liquid paraffin oil on a porous CHINF/PAA film that was subjected to hydrophobization and on a SLIPS created through the addition of liquid paraffin oil in a drop-wise fashion to the hydrophobized porous film. Below: equivalent pictures of liquid drops on various films. (d) The total interfacial energy per unit area for the wetting configuration 1 is denoted by E_1 , the total interfacial energy per unit area for the wetting configuration 1 is denoted by E_2 and the total interfacial energy per unit area for the wetting configuration 1 is denoted by E_A . Every delta is indicative of a key criterion for the maintenance of the stability of a lubricating film on a functional SLIPS in the working conditions outlined in equations (5-2) and (5-3). Reproduced with permission from Ref [147]. Copyright 2016 American Chemical Society.

Figure 5-6. The paraffin mixture volume ratio dictating the contact angle (a) and sliding angle

(b) of a 10 μL water droplet at various temperatures (solidifiable: liquid paraffin = 1:10, lime-green line; 1:15, yellow line; 1:20, pink line; 1:25, purple line; 1:30, blue line; 1:35, green line; 1:40, brown line; 1:45, red line; and 1:50, black line). (c) Charged-couple device camera images of 10 μL water droplet on a TA-SLIPS at a volume ratio of 1:25 at various temperatures. (d) TA-SLIPS with a volume ratio of 1:25 imaged at various temperatures with colour two-dimensional laser scanning microscopy. Below: equivalent scale bars of roughness, while the black scale bars are all 100 μm . The supporting information provides three-dimensional images of greater size. Reproduced with permission from Ref [147]. Copyright 2016 American Chemical Society.

Figure 5-7. TA-SLIPSs imaged with colour three-dimensional laser scanning microscope at various temperatures. Below: surface roughness (R_a and RMS) associated with various temperatures. The X axis is 200 μm and the Y axis is 283.6 μm . Reproduced with permission from Ref [147]. Copyright 2016 American Chemical Society.

Figure 5-8. Time-resolved images taken with a high-speed camera showing TA-SLIPSs at various temperatures. Reproduced with permission from Ref [147]. Copyright 2016 American Chemical Society.

Figure 5-9. The melting point determined according to the paraffin mixture volume ratio. Reproduced with permission from Ref [147]. Copyright 2016 American Chemical Society.

Figure 5-10. The effect of varying temperature on the paraffin mixture surface tension (solidifiable: liquid paraffin = 1:10, lime-green line; 1:15, yellow line; 1:20, pink line; 1:25, purple line; 1:30, blue line; 1:35, green line; 1:40, brown line; 1:45, red line; and 1:50, black line). Reproduced with permission from Ref [147]. Copyright 2016 American Chemical Society.

Figure 5-11. (a) The impact of paraffin mixture volume ratio (solidifiable: liquid paraffin = 1:10, lime-green dots; 1:15, yellow dots; 1:20, pink dots; 1:25, purple dots; 1:30, blue dots; 1:35, green dots; 1:40, brown dots; 1:45, red dots; and 1:50, black dots) at various temperatures

on the transmittance of TA-SLIPSs at 550 nm. (b) Temperature-based changes in the transmittance of TA-SLIPSs with 1:25 volume ratio (0°C, black dots; 5°C, gray dots; 10°C, purple dots; 15°C, magenta dots; 20°C, pink dots; 25°C, sky-blue dots; 26°C, blue dots; 27°C, dark-blue dots; 27.5°C, dark-green dots; 28°C, green dots; 28.5°C, lime-green dots; 29°C, yellow dots; 29.5°C, orange dots; and 30°C, red dots). (c) Temperature-based T.T., HAZE, P.T. and DIF of TA-SLIPSs with 1:25 volume ratio, as respectively denoted by orange, blue, green and purple bars. The supporting information provides further explanation about the optical parameters. DIF divided by T.T. gave the HAZE, indicating how much light was dispersed with the passing of light through the film. (d) Temperature-dependent models of TA-SLIP scattering and related digital microscopy imaging of TA-SLIPSs at various temperatures (100 μm scale bar). (e) The effect of temperature rise in the range of 0-30°C at 2°C intervals on the optical performance of TA-SLIPSs with 1:25 volume ratio. Reproduced with permission from Ref [147]. Copyright 2016 American Chemical Society.

Figure 5-12. Temperature-dependent alterations in the transmittance of TA-SLIPSs with 1:25 volume ratio as seen in two-dimensional imaging (0°C, black dots; 5°C, grey dots; 10°C, purple dots; 15°C, magenta dots; 20°C, pink dots; 25°C, sky-blue dots; 26°C, blue dots; 27°C, dark-blue dots; 27.5°C, dark-green dots; 28°C, green dots; 28.5°C, lime-green dots; 29°C, yellow dots; 29.5°C, orange dots; and 30°C, red dots). Reproduced with permission from Ref [147]. Copyright 2016 American Chemical Society.

Figure 5-13. Two-dimensional imaging of temperature-based alterations of paraffin mixture absorbance in a quartz cell. Reproduced with permission from Ref [147]. Copyright 2016 American Chemical Society.

Figure 5-14. Three-dimensional imaging of temperature-based alterations of paraffin mixture absorbance in a quartz cell. Reproduced with permission from Ref [147]. Copyright 2016 American Chemical Society.

Figure 5-15. Surface roughness and transmittance correlation; T , T_0 , σ and λ respectively

denote coating transmittance in the presence and absence of surface roughness, the RMS surface roughness, and the wavelength. Reproduced with permission from Ref [147]. Copyright 2016 American Chemical Society.

Figure 5-16. Repeated switching of the transparency (a) and attachment (b) of a 10 μL droplet of water on TA-SLIPS with 1:25 volume ratio at 30°C and 20°C. Reproduced with permission from Ref [147]. Copyright 2016 American Chemical Society.

List of Tables

Table 2-1. Average bilayer thickness measured in an ellipsometric manner at a pH value of 2 and temperature of 23°C for poly(methacrylic acid) (PMAA; M_w 150 K) constructed with poly(ethylene oxide) (PEO; M_w 200 K), poly(N-vinylpyrrolidone) (PVPON; M_w 360 K), poly(acrylamide) (PAAM; M_w 5,000 K), poly(N-isopropyl acrylamide) (PNIPAM; M_w 300 K), poly(vinyl methyl ether) (PVME; M_w 200 K), poly(N-vinylcaprolactam) (PVCL; M_w 1.8 K), and poly(2-hydroxyethyl acrylate) (PHEA; M_w 600 K). Reproduced from Ref [45] with permission of Taylor & Francis (Copyright 2006).

Table 4-1. The measurements obtained for the contact angles and surface tensions of water and almond oil as well as the interfacial tension and spreading coefficient among water and almond oil. Reproduced with permission from Ref [132]. Copyright 2015 American Chemical Society.

Table 5-1. The thickness and refractive index of porous underlayers with varying number of bilayers and the porous underlayer demonstrating hydrophobicity. Reproduced with permission from Ref [147]. Copyright 2016 American Chemical Society.

Table 5-2. The contact angle and surface tension associated with water and liquid paraffin oil as well as the determined interfacial tension and spreading coefficient between the two liquids. Reproduced with permission from Ref [147]. Copyright 2016 American Chemical Society.

Chapter 1

Introduction

1.1 Overview

Various challenges facing different sectors, including energy, environment and biomedicine, could potentially be overcome with materials inspired by the natural world.¹⁻³ As such materials, especially controlled surfaces, are attracting more and more interest, micro/nano architectures have arisen as promising and innovative solutions. The self-cleaning capability of lotus leaves,⁴⁻⁶ the anti-fouling effect of sharkskin,^{7,8} the anti-reflective property of moth eyes,⁹⁻¹¹ the strategy employed by the Namib Desert Beetle to collect water,^{12,13} and the sticky surface of geckoes^{14,15} are all prime instances of original design concepts inspired by nature. In particular, research conducted over the last ten years on interfaces has focused extensively on the replication of the self-cleaning capability of lotus leaves.¹⁶ Solid-air/liquid composite interfaces with low surface energy have been able to be designed within composite micro/nanostructures by employing artificial hydrophobic surfaces with this capability. These interfaces were proven to retain a high value for contact angle as well as low contact-angle hysteresis against droplets of water or particular organic liquids.¹⁷ Nevertheless, surfaces integrating the properties of repelling liquids with low surface tension,¹⁸ withstand scratching,¹⁹ and high transmittance²⁰ are yet to be developed without enormous difficulty.

These challenges could be addressed with liquid-impregnated surfaces (LISs). Dynamic

fluid surfaces exhibiting “super-slippy” features can be obtained through liquid addition in a solid material.²¹ LISs have been successfully applied in the creation of slippery liquid-infused porous surfaces (SLIPS), which draw inspiration from the *Nepenthes* pitcher plant, proposed by Aizenberg and colleagues to address these limitations.^{22–25} The self-healing SLIPS they developed exhibited better performance than their natural equivalents, while the cutting edge artificial hydrophobic surfaces were demonstrated to serve as effective repellents of both simple and complex liquids (e.g. water, blood, low surface tension liquid and others), preserve low contact-angle hysteresis. Trapping of an impregnated lubricating fluid is facilitated by substrates with nano/microstructures. To be able to develop an inert slippery interface possessing stability and without any defects, the lubricant must be based on a structure with low surface energy.²⁶ Meanwhile, the transmittance alteration of SLIPS was addressed by a different study.²⁷ Hence, close attention should be paid to the choice of underlayer and lubricant oil to form other SLIPS, according to the desired applications.

Surface wettability and optical properties of the underlayer have been found to be particularly dependent on surface topography. By employing top-down or bottom-up production methods, such as lithography and molecular self-assembly, respectively, the topography of a rough surface can be customised from nano- to micro-scale configurations, thereby creating an ordered, random or hierarchical structure out of the surface.^{28,29} Surface wettability,³⁰ reflection,³¹ scattering,³² structural color,³³ adhesion³⁴ and mechanical properties³⁵ can be adjusted by regulating the features of materials with nano- or micro-structures, including size, shape, morphology and composition. The chemical make-up of a material is also a major parameter, with chemical alterations usually eliciting a reaction to stimuli. Smart surfaces are functional materials that can change their surface characteristics in response to external stimuli. They have received an ample amount of attention in recent times.^{36,37}

The development of solutions for regulation of surface wettability and optical properties has been attempted by numerous researchers by deriving ideas from Layer-by-Layer (LbL) self-assembly. The first production of multilayer thin films using the technique of LbL self-assembly happened at the beginning of the 1990s.³⁸ The concept of polyelectrolytes with opposite charges alternately adsorbed through electrostatic attraction underpins this technique, which facilitates the creation of multilayer films with customised nanostructures in an inexpensive, environmentally safe, and straightforward way.³⁹ It is also compatible with most substrates and elements.⁴⁰ LbL self-assembly usually enables development of multilayer films based on electrostatic interactions, but it can also rely on interactions of lesser strength (e.g. hydrogen-bonding).⁴¹ Two different groups of researchers concomitantly undertook hydrogen-bonding LbL assembly for the first time in 1997.^{42,43} Formation of hydrogen-bonding LbL films involves polymers with hydrogen bond acceptor and hydrogen bond donor being deposited in alternate fashion.⁴⁴ However, unlike films created on the basis of electrostatic interactions, hydrogen-bonding LbL films are not as easy to develop.⁴⁵ Nevertheless, they are still useful for some applications. There are three particular strengths of these films. One such strength is that they simplify the creation of thin films with pH sensitivity.^{46,47} The second strength is that they can be transformed into ultrathin hydrogel materials with one or more constituents *via* a range of different techniques.^{48,49} The third strength is that they enable polymers with low temperatures of glass transition to be incorporated into thin films.^{50,51} Thanks to these strengths, hydrogen-bonding films created by LbL self-assembly show potential for various new applications, including drug delivery systems susceptible to pH or temperature,^{52,53} materials with mechanical features that can be adjusted, and films that dissolve in physiological media.^{54,55}

1.2 Research questions and hypotheses in each chapter

In this dissertation, porous structures generated *via* LbL were applied to SLIPS to achieve various functional surfaces. As the above-mentioned properties, LbL films can control the surface structures by changing the components, which indicates that the desired structures should achieve the intended SLIPS. In addition, changing lubricant layer of the SLIPS should lead the enhancement of the wettability and optical properties. Here, the thesis states the following hypothesis. At first, SLIPS have the potential to become high transmittance film if underlayer of lubricant is superhydrophobic film with high transmittance and low reflectance. Next, if the lubricant oil contacting with target liquid has antithrombogenic property, SLIPS should show the same property for medical device uses. Finally, SLIPS can be smart surfaces with optical transparency and surface wettability if the structure of the outermost surface and the scattering factor of the lubricant layer are simultaneously controlled by varying the lubricant oil morphology. These surfaces should contribute to resolving current limitations in various industrial spheres and in medicine with the remarkable properties of complex material interfaces derived from natural nano- and microstructures.

The dissertation is arranged as follows (Figure 1-1):

Chapter 1 provides overview of the dissertation and thesis outline. The chapter reveals the positioning of the study.

Chapter 2 introduces a literature review of the study of LbL and SLIPS. For the LbL, the fundamentals of electrostatic and hydrogen-bonding LbL with some applications are explained to create porous structure *via* LbL. The section of the SLIPS provides basic criteria of SLIPS after introducing the fundamental surface wettability.

Chapter 3 achieves optically enhanced SLIPS. Increasing attention is being paid to slippery liquid-infused surfaces due to their potential for use as transparent, non-fouling and anti-frosting artificial surfaces for solar cells and optical devices. The present section is

concerned with the transparency of lubricant-impregnated texture on anti-reflective films formed based on the method of LbL self-assembly and capable of diminishing light scattering, which plays a crucial role in the maintenance of device properties.

Chapter 4 details SLIPS enhanced through wettability. The creation of fluorinated SLIPS without biocompatibility has been addressed in earlier research. In the present study, biodegradable materials and biocompatible lubricant were used to create films impregnated with fluid. Based on the LbL self-assembly technique, the creation process of the underlayer involved chitosan and alginate interacting electrostatically and hydrogen-bonding among alginate and polyvinylpyrrolidone (PVPON). With the biocompatible almond oil, the biocompatible SLIPS demonstrate antithrombogenicity.

Chapter 5 achieves responsive SLIPS with controlling optical transparency and surface wettability. SLIPS are among the smart surfaces with the highest performance, exhibiting high level of repellence, effectively achieving switchable adhesion and adjustable transparency, the regulation of which is undertaken by a graded mechanical stimulus. Nevertheless, the endeavours that have been made so far have not been enough to create surfaces with a high degree of repellence and sensitive to temperature under conditions of ambient temperature and pressure, due to the fact that the basic unit employed in most earlier repellent surfaces is non-reactive lubricant oil. Hence, the creation of multifunctional materials capable of dynamic adaptations to temperature fluctuations is the aim of this study. In particular, the study proposes temperature-activated solidifiable/liquid paraffin-infused porous surfaces (TA-SLIPSs) with the ability to concomitantly control their transparency and regulation of water droplet motion at room temperature.

Chapter 6 gives conclusion and implication for future works as a final chapter. Here, the overall conclusion indicates the significance of this dissertation.

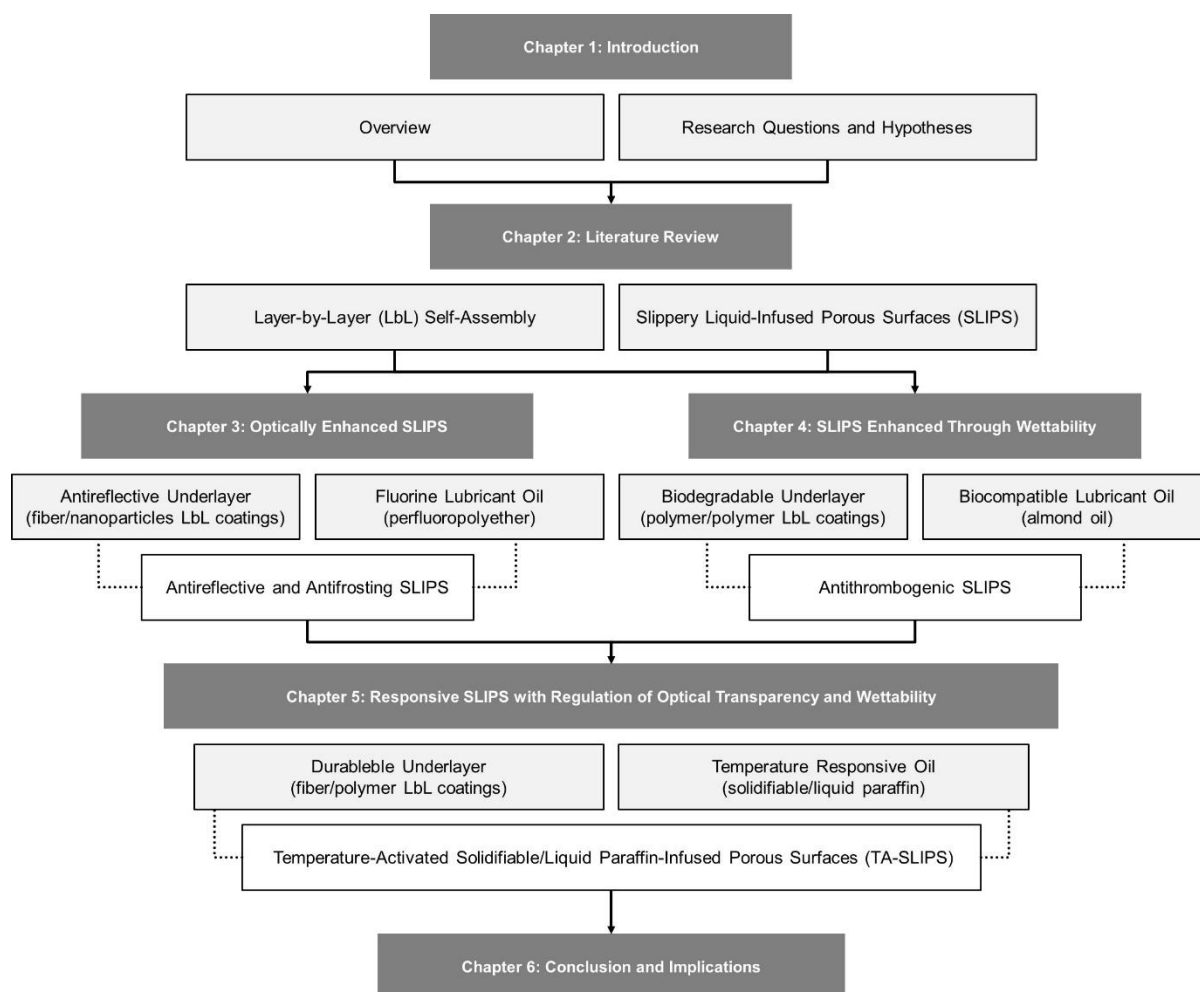


Figure 1-1. Overview of dissertation structure.

Chapter 2

Literature Review

2.1 Layer-by-Layer self-assembly method

In the present section, the available studies on polyelectrolyte multilayer assemblies are reviewed, with particular emphasis on hydrogen-bonding multilayers and related porous approach for SLIPS implementation.

2.1.1 Electrostatic Layer-by-Layer self-assembly method

During the early 1990s, the LbL assembly was employed for the first time by Decher *et al.* to produce multilayer thin films (Figure 2-1).³⁸ An uncomplicated and flexible technique applicable under conditions of ambient temperature and pressure, the LbL assembly is underpinned by alternate adsorption of materials with opposite charges through electrostatic attraction. The main advantage of this technique is that it enables modulation of film surface texture and thickness on both a micro- and nano-scale. Antireflective¹¹ and superhydrophobic coatings⁵⁶ as well as systems of drug delivery⁵¹ are among the applications in which films created *via* LbL assembly are used.

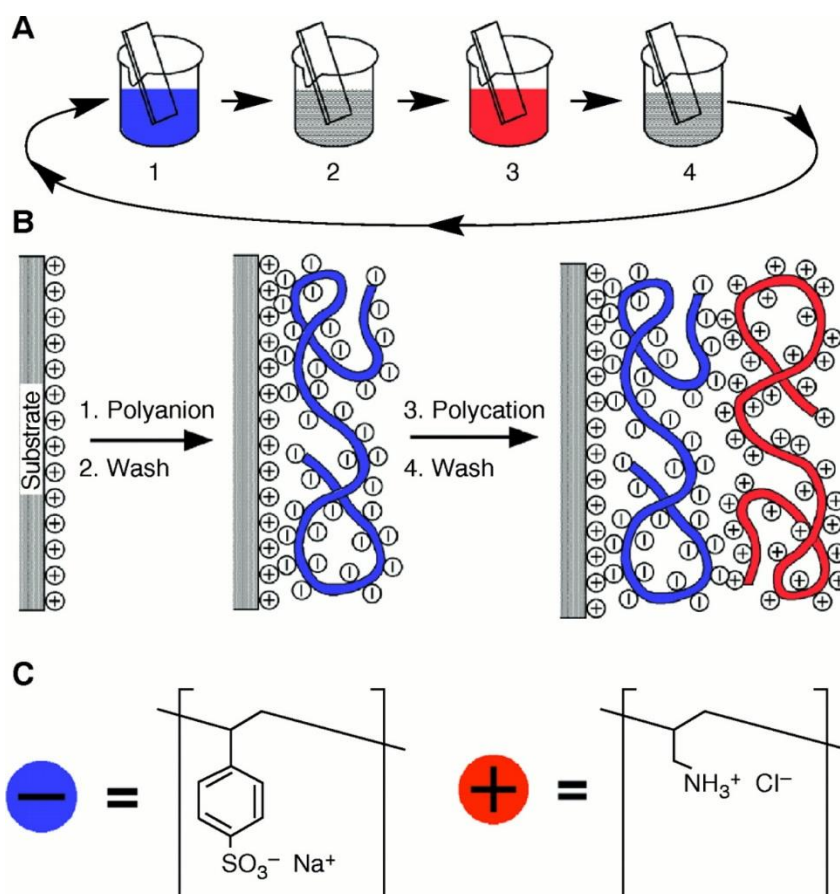


Figure 2-1. Diagram showing how LbL is applied to charged solid substrates. From Ref [38].

Reprinted with permission from AAAS (Copyright 1997).³⁸

2.1.1.1 Basic principles of polyelectrolytes

A polymer comprising dissociable groups, such as amino groups ($-\text{NH}_2/-\text{NH}_3^+$), carboxylic acid groups ($-\text{COOH}/-\text{COO}^-$) and sulfo groups ($-\text{SO}_3\text{H}/-\text{SO}_3^-$) that can occur as ions in solution is known as a polyelectrolyte. The extensive electrical charge of sizable polymer ions occurring in solution is the source of the singular features and behaviour displayed by polyelectrolytes. A range of constituents enter the composition of polyelectrolyte solutions, including polymer ions, counter-ions with low molecular weight, and solvent (water), which interact electrostatically with one another. Consequently, various events may take place in solution:

1. Modifications in the configuration of dissociated polymer ions in solution
2. Interplay between polymer ions in solution as well as interplay among polymer ions and ions with low molecular weight
3. Polymer ion hydration

Ions with low molecular weight are generated when polyelectrolytes are ionised in solution. These ions can be counter-ions or poly-ions with an electrical charge dictated by the degree of ionisation. For example, ionised groups ($-\text{COO}^-$) form along the backbone of the polymer when a polymer with weak acid groups (e.g. $-\text{COOH}$ groups) reacts with a base. Nonetheless, not all $-\text{COOH}$ groups are used up. Consequently, the pH of the solution may influence the number of available ionised groups to a greater extent than the degree of polymerisation. Polyelectrolytes can be either strong or weak, depending on whether polymers exhibit complete or only partial ionisation.⁵⁷

Dissociation in solution is exhibited by organic weak acid (HA), such as acetic acid and benzoic acid, as expressed by the relationship below:



The dissociation constant and the dissociation ratio of the dissociable group are respectively denoted by K and $\alpha = [\text{A}^-]/[\text{HA}] + [\text{A}^-]$.

$$K = \alpha_{\text{H}^+} \frac{[\text{A}^-]}{[\text{HA}]} = \alpha_{\text{H}^+} \frac{\alpha}{1-\alpha} = e^{-\Delta G^0/RT} \quad (2-2)$$

$$\text{pK} = -\log K = \text{pH} - \log \frac{\alpha}{1-\alpha} = 0.434 \frac{\Delta G^0}{RT} \quad (2-3)$$

where H^+ activity is denoted by α_{H^+} .

Interaction among every dissociable group is assumed to occur due to the dissociation behaviour displayed by weak acidulant polymers such as polyacrylic acid. The increase in pK is directly proportional to α and the effect of dissociable $-\text{COO}^-$ determines an increase in the pK of $-\text{COOH}$ dissociation on this molecule. Numerous studies have investigated how pK and α are correlated about weak acidulant polymers besides polyacrylic acid. The expression of

these mathematical models is based on the Henderson Hasselbalch equation.

$$\text{pH} = \text{p}K_a + n \log \frac{\alpha}{1-\alpha} \quad (2-4)$$

where the polyacid types and ionic strength determine $\text{p}K_a$ and n . The generic expression of this equation takes the form below:

$$\text{p}K = \text{p}K_0 + \Phi_1 \alpha + \Phi_2 \alpha^2 + \Lambda \quad (2-5)$$

where Φ_1 and Φ_2 are constant depending on polyacid and ionic strength, respectively. The $\text{p}K$ value of limit $\alpha \rightarrow 0$ is denoted by $\text{p}K_0$, which is correlated with ΔG° .

$$\text{p}K_0 = 0.434 \frac{\Delta G^\circ}{RT} \quad (2-6)$$

In the case that the polymer has electric charge, it is the electrostatic interaction energy ΔG_e rather than ΔG° that is the normal free energy change releasing H^+ from $-\text{COOH}$.

$$\text{p}K = 0.434 \frac{(\Delta G^\circ + \Delta G_e)}{RT} = \text{p}K_0 + 0.434 \frac{\Delta G_e}{RT} \quad (2-7)$$

$$\frac{\Delta G_e}{N_0} = -e\varphi_0 \quad (2-8)$$

where φ_0 and N_0 are the potential molecular surface and Avogadro's number, respectively.

Hence,

$$\text{pH} = \text{p}K_0 + \log \frac{\alpha}{1-\alpha} - 0.434 \frac{e\varphi_0}{kT} \quad (2-9)$$

$$\text{pH} = \text{p}K_0 + \log \frac{\alpha}{1-\alpha} \quad (2-10)$$

This is associated with either the electrostatic free energy of the polymer or surface potential.

Surfactant serves as representative of low molecule adsorption exhibiting zeta potential (ζ) on a glide plane of electric double layer based on interplay with the interfacial electric double layer developed on the surface. To evaluate low molecule adsorption on surfaces such as fabrics, consideration must be given to alteration in surface charge density (σ) as determined by zeta potential, particularly how much adsorption there is per unit surface area, as measured based on a difference of surface charge density ($\Delta\sigma$) between these corollaries in both the absence and presence of low molecule. Furthermore, calculation of adsorption free energy ΔG

is based on its concentration and gradient on $\zeta = 0$, while other thermodynamic matter is determined based on concentration modification, which promotes low molecule adsorption on the surface of fabrics, if linearity is exhibited by the value derived from the $\zeta - \log C$ curve (C = low molecule concentration) of these corollaries. Examination has also focused on surface adsorptive property, alteration in fabric fine structure, assessment of surface area about dyeing, fabric reformulation, dye affinity, critical micellar concentration, and surfactant's surface adsorptive property. Various studies have adopted both a theoretical and empirical approach in the investigation of polymer or polyelectrolyte adsorption on polymer surface in relation to a range of key aspects, including adhesion, coating material, paper production and conversion, as well as fabrics. Formation of an electrical double layer occurs on both surfaces when polymer materials are adsorbed on the polymer surface.

2.1.1.2 The concept of electrostatic Layer-by-Layer self-assembly

Synthetic polyelectrolytes are usually employed in Layer-by-Layer (LbL) assembly, but metallic nanoparticles, metal oxide particles, and natural polyelectrolytes, such as protein and DNA, can also be employed.

As indicated by Decher *et al.*, alternate immersion of a substrate into solutions of polycation and polyanion leads to the formation of multilayer films.³⁸

Glass slides and silicon wafers with numerous hydroxyl groups on their surface are the main substrates employed in the production of LbL films. Conversion of these hydroxyl groups into the form of $-O^-$ typically occurs at the pH solution under which the LbL assembly operates. Hence, activation of LbL build-up requires immersion of substrates with negative charge into a polycation solution.

Once the first layer is formed, the electrical charge of the surface is the opposite of that of the substrate. This enables adsorption of anionic macromolecules above the polycationic layer. The charge surface changes anew once the second layer is formed. The formation of

multilayer film is promoted by iteration of this process.⁵⁸

Every polycation and polyanion adsorption must be followed by rinsing in solvent to eliminate macromolecules that are not effectively adsorbed on the surface and thus to ensure a film uniformity.

The growth of polyelectrolyte films is dependent on several parameters. A particularly important parameter underpinning adsorption and multilayer formation is the charge density on the polyelectrolytes. In addition, multilayer film formation is also dependent on polyelectrolyte solution parameters (e.g. pH, ionic strength and solution concentration) as well as molecular parameters (e.g. polymer molecular weight, types of functional groups that can be subjected to ionisation and polymer pK_a). The conformation of the chains in the LbL is especially dependent on solution pH and polymer pK_a (Figure 2-2).³⁹

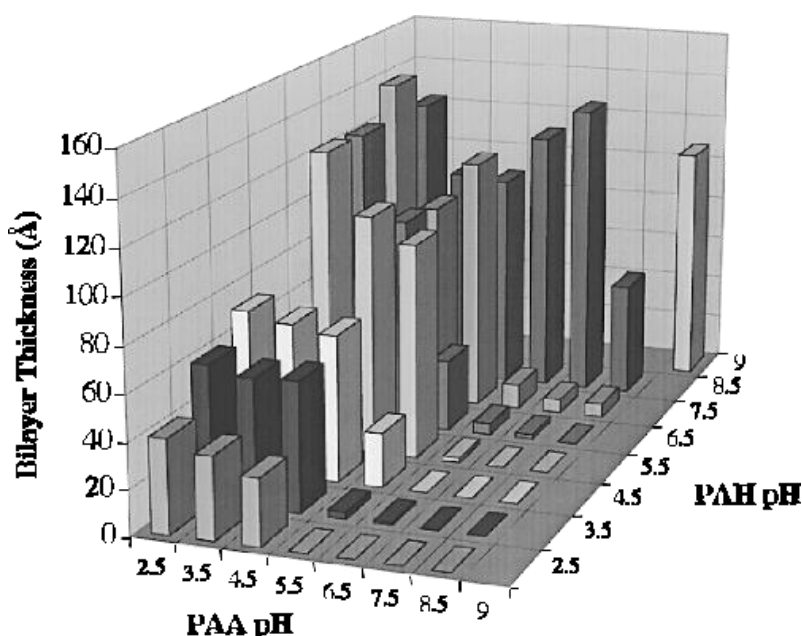


Figure 2-2. Complete pH matrix illustrating how the PAH/PAA bilayer contributes to the average increasing thickness in relation to the dipping solution pH. Reproduced with permission from Ref [39]. Copyright 2000 American Chemical Society.³⁹

2.1.2 Hydrogen-bonding Layer-by-Layer self-assembly method

Aside from the popular electrostatic interactions, weaker interactions (e.g. hydrogen bondings) can facilitate formation of multilayer films as well. Although they are not as easy to develop as LbL films created through electrostatic interactions, hydrogen-bonding LbL films are highly advantageous to certain applications.⁴⁵ Hydrogen-bonding assembly provides three key properties, namely, creation of pH-sensitive thin films without difficulty, multiple options for transformation of hydrogen-bonding films into hydrogel materials of minimal thickness and with one or more components, and incorporation into the thin films of polymers with low temperatures of glass transition. Applications of LbL films made possible by such properties include drug delivery systems sensitive to pH or temperature, material with mechanical properties that can be adjusted, release films that dissolve in physiological conditions, and proton exchange membranes for fuel cells.^{46,59}

2.1.2.1 The basic principles of hydrogen-bonding assembly

Polymer deposition with alternate hydrogen bond acceptor and hydrogen bond donor is the underlying principle of hydrogen-bonding LbL films. Poly(ethylene glycol) (PEG) with oxygen atoms on the backbone of the polymer and poly(N-vinylpyrrolidone) (PVPON) with the carbonyl group are the two most commonly used hydrogen bond acceptors, while polyacids like poly(methacrylic acid) (PMA) and poly(acrylic acid) (PAA) containing carboxylic acid are the main hydrogen bond donors (Figure 2-3).^{44,60}

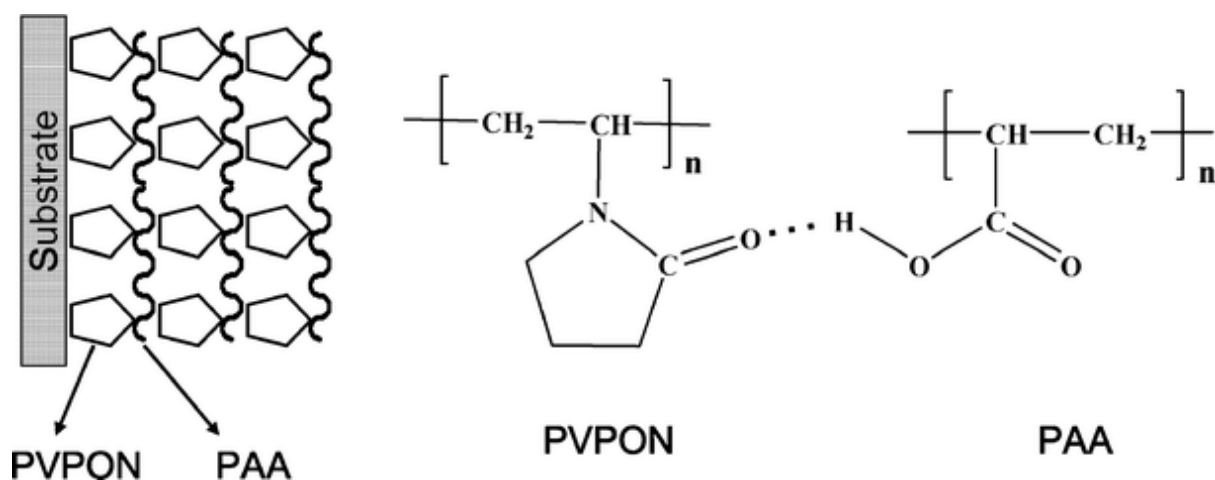


Figure 2-3. Diagram showing how PVPON and PAA are constructed based on hydrogen-bonded LbL films. Reproduced from Ref [60] with permission of Springer (Copyright 2012).⁶⁰

The first demonstration of hydrogen-bonding LbL assembly was achieved at the same time in 1997 by Rubner and Zhang.^{42,43} The role played by hydrogen-bonding interactions as catalysts of deposition of LbL films in aqueous solutions was exemplified by Stockton and Rubner by employing alternate layers of polyaniline (PANi) and polymers without charge, like PVPON, poly(vinyl alcohol) (PVA), poly(acrylamide) (PAAm) or poly(ethylene oxide) (PEO).⁴² Meanwhile, to provide evidence for the use of hydrogen bondings in the formation of multilayer films, Zhang and colleagues conducted research on hydrogen-bonding-directed multilayer systems between PAA and PVPON.⁴³ In a different study, PVPON as the hydrogen bond acceptor and m-methyl-formaldehyde as the hydrogen bond donor were employed to achieve hydrogen-bonding assembly on particle templates.⁴⁴ Complete protonation of polyacids is guaranteed by low pH in the case of hydrogen-bonded films based on polycarboxylic acids and two neutrally charged polymers underpin hydrogen-bonded LbL deposition. An overview of data related to film thickness associated with various polycarboxylic acid/neutral polymer systems assembled on the basis of LbL deposition on planar substrates from weak ionic solutions at a pH value of 2 is provided in Table 2-1, while

Figure 2-4 illustrates the chemical configurations of the polymers employed in self-assembly.

Table 2-1. Average bilayer thickness measured in an ellipsometric manner at a pH value of 2 and temperature of 23°C for poly(methacrylic acid) (PMAA; M_w 150 K) constructed with poly(ethylene oxide) (PEO; M_w 200 K), poly(N-vinylpyrrolidone) (PVPON; M_w 360 K), poly(acrylamide) (PAAM; M_w 5,000 K), poly(N-isopropyl acrylamide) (PNIPAM; M_w 300 K), poly(vinyl methyl ether) (PVME; M_w 200 K), poly(N-vinylcaprolactam) (PVCL; M_w 1.8 K), and poly(2-hydroxyethyl acrylate) (PHEA; M_w 600 K). Reproduced from Ref [45] with permission of Taylor & Francis (Copyright 2006).⁴⁵

Polymer system	PMAA/ PEO	PMAA/ PVPON	PMAA/ PAAM	PMAA/ PNIPAM	PMAA/ PVME	PMAA/ PVCL	PMAA/ PHEA
Bilayer thickness (nm)	20	4	7	6	15.6	4.8	13

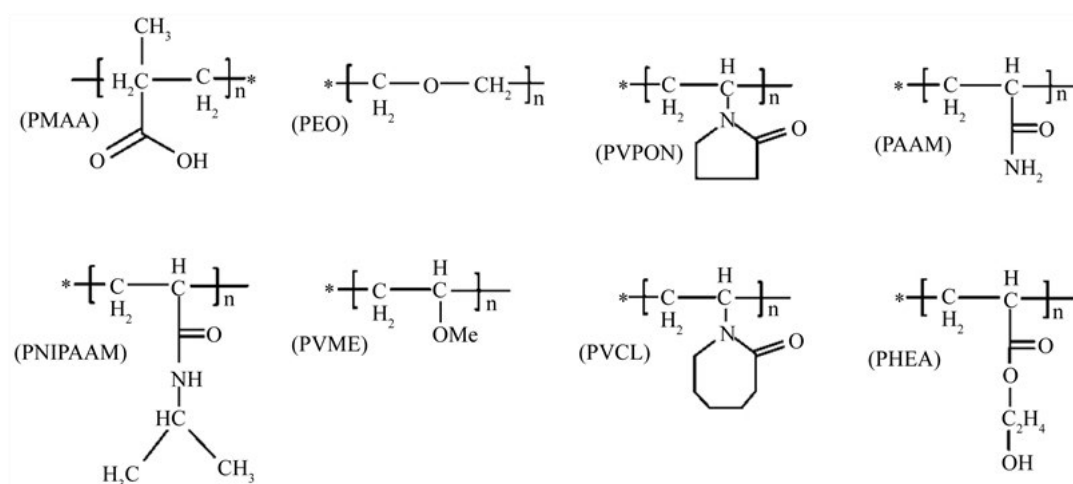


Figure 2-4. Chemical configurations of the polymers used in self-assembly outlined in Table 2-1. Reproduced from Ref [45] with permission of Taylor & Francis (Copyright 2006).⁴⁵

Loading and discharge of functional molecules from hydrogen-bonding LbL films are facilitated by the fact that these films usually possess high susceptibility to pH and ionic strength. Comparative analysis of films underpinned by hydrogen-bonding and electrostatic interactions, respectively, reveals that there is a restricted pH spectrum for the interaction of hydrogen-bonding polymers and for their ability to create stable films. The reason for this is the dependence on the pKa of the component polymers and the strength of the interplay between the polymer pairs with hydrogen-bonding functional groups. The susceptibility of the hydrogen-bonding LbL between PVPON/PAA to pH has been highlighted by Xu and colleagues,⁴¹ who demonstrated that the pH is a major determinant of how thick hydrogen-bonding LbL multilayers can get and how they are morphologically structured. In a different study, a high ionic strength was demonstrated to facilitate PVPON/PAA film disassembly, while the loading of Ag⁺ ions into the PVPON/PAA multilayers and subsequent discharge were shown to be aided by film immersion in solutions with low pH.⁶¹ Compared to PMA/PEG films, which deconstruct at a pH of about 4,⁶² greater stability is exhibited by PMA/PVPON hydrogen-bonding films, which deconstruct at a pH of about 6.4.⁴⁶ Furthermore, Sukhishvili and Granick demonstrated that hydrogen-bonding LbL films with a composition of PEO and PMAA allowed incorporation of rhodamine 6 G dye and its discharge was possible under particular conditions.⁴⁷ The two authors further reported that hydrogen-bonded multilayer with a composition of PMAA and block copolymer micelles (BCMs) swell and discharged small molecules as a function of temperature (Figure 2-5).⁴⁹

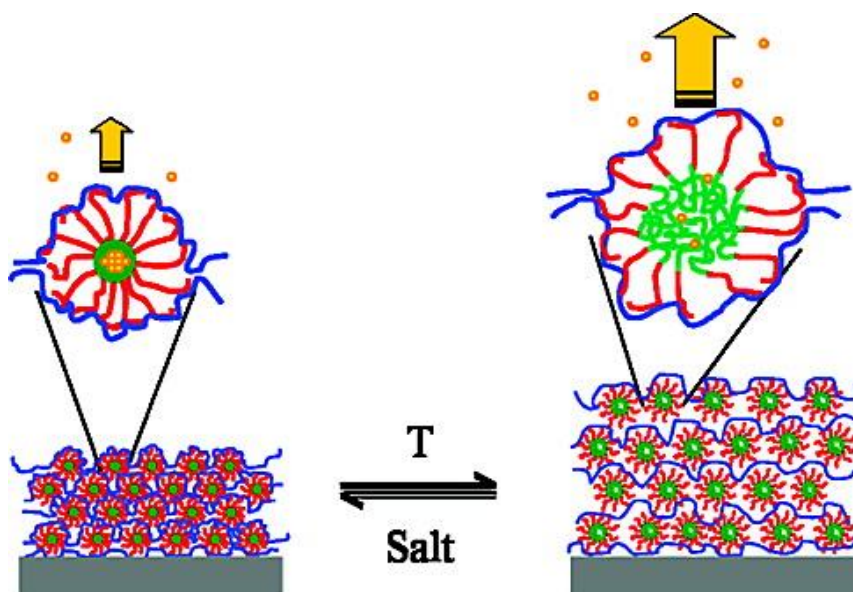


Figure 2-5. Diagram showing non-permanent BCM/PMAA film swelling under the influence of temperature. Reproduced with permission from Ref [49]. Copyright 2009 American Chemical Society.⁴⁹

Hydrogen-bonding multilayer films can also be constructed with macromolecules with susceptibility to temperature, like poly(*N*-isopropylacrylamide) (PNIPAM), poly(*N*-vinylcaprolactam) (PVCL) and poly(vinyl methyl ether) (PVME). The solubility of these polymers is altered significantly at a specific low critical solution temperature (LCST).⁵² For example, the LCST of the thermo-responsive polymer of widespread usage, PNIPAM, is 32°C. If this polymer is polymerised alongside a co-monomer displaying hydrophilicity or hydrophobicity, its LCST can be adjusted. Films and capsules of biomedical relevance with properties susceptible to temperature and undergoing transformations at a temperature similar to the body temperature (37°C) could be developed through the integration of these polymers in an LbL multilayer. In the process of polymer deposition or following film formation, it is possible to adjust the thickness of multilayers underpinned by polymers with temperature sensitivity according to temperature.^{49,53}

2.1.2.2 Stabilisation of hydrogen-bonding film

From an experimental perspective, ionic or hydrogen bond self-assembly is uncomplicated and widely employed, but its use in both *in vitro* and *in vivo* applications may be hampered by the fact that it is unstable under certain conditions.⁶³ In general, the stability of hydrogen-bonded multilayers is ensured solely under acidic conditions. However, hydrogen-bonding materials have become more versatile in recent times due to the use of diverse polymer building blocks and crosslinking methods to achieve film stability. The developments in hydrogen-bonding films made possible by such innovations in material design have benefitted applications related to drug delivery and micro-reactors.⁶⁴

The application of chemical,⁶⁵ thermal⁶⁶ or photochemical methods for purposes of crosslinking to stabilise hydrogen-bonding multilayers has been resorted to in numerous studies. Since a polyacid is frequently used as a hydrogen bond acceptor in hydrogen-bonding LbL, the hydrogen bonding can be disrupted when the pH is increased beyond the pKa of the polyacid through deprotonating the carboxylic acid group. For example, covalent crosslinking of PMAA in PMAA/PVPON or PMAA/PEO hydrogen-bonding films or capsules was achieved by Sukhishvili and colleagues through carbodiimide chemistry.⁶⁴ Meanwhile, carbodiimide-supported crosslinking between hydrogen-bonding multilayer and ethylenediamine was shown by Kozlovskaya and Sukhishvili to facilitate the production of two-component PVCL or PVPON-NH₂-20/PMAA capsules with properties sensitive to pH.⁶⁷ A non-permanent response to environmental pH alterations is generated by the capsules by varying their diameter and permeable character. One study revealed that the capsule walls shifted from high association to full dissociation according to pH.⁶⁸ Furthermore, a different study reported that PMAA hydrogel films or capsules were obtained as a result of neutral polymer chains being wholly released from the cross-linked films in alkaline conditions when unfunctionalised PVPON or PEO was employed in self-assembly.⁶⁹

Thiol and disulphide bonds were used in polymers by Caruso and colleagues as a new

strategy of layers crosslinking.^{54,55} To this end, they applied hydrogen-bonding self-assembly to achieve the synthesis of thiol-modified PMA (PMA_{SH}) and fabricated PMA_{SH}/PVPON films. Oxidation based on chloramine T (CaT) subsequently permitted the conversion of the thiol groups into disulphide linkages. As shown in Figure 2-6, once PVPON was removed by breaking down the hydrogen bonds between the deprotonated PMA and PVPON at physiological pH, single-component PMA(SH-disulfide) capsule preparation was permitted by the hydrogen-bonding multilayers. The general assumption is that oxidising conditions (e.g. bloodstream) ensure the stability of disulphide linkages, while reduction conditions (e.g. cell cytoplasm) contribute to their destabilisation.

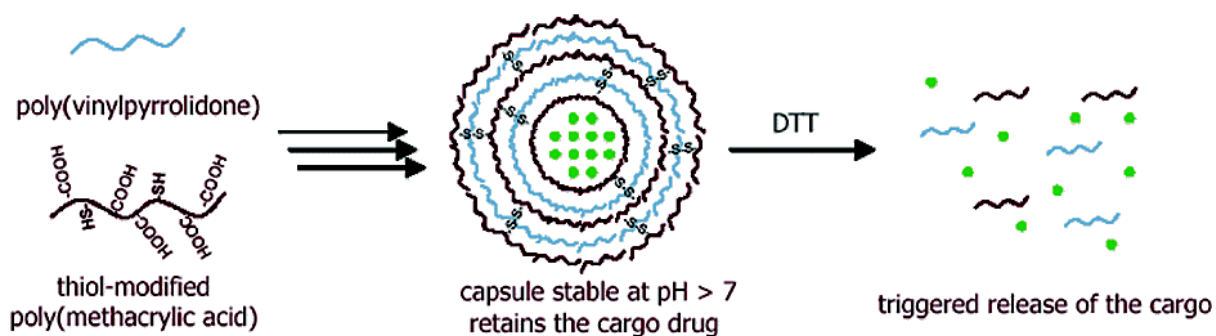


Figure 2-6. Cysteamine-functionalised PVPON and PMA used in the construction and crosslinking of hydrogen-bonded multilayer thin films. Reproduced with permission from Ref [54]. Copyright 2006 American Chemical Society.⁵⁴

2.1.3 Porous structure *via* Layer-by-Layer self-assembly

Earlier studies have employed silica nanoparticles or cellulose nanowires to produce porous films *via* LbL with the purpose of expanding airspaces. For instance, synthesised hollow silica nanoparticles displaying variation in particle size and shell thickness afforded Cohen and colleagues single and graded index designs for accomplishment of AR coatings.⁷⁰ Meanwhile,

Kotov and colleagues argued that an innovative architecture of high porosity developed by orienting and superimposing cellulose nanowires at random was what gave AR properties their strength.⁷¹ Moreover, in a different study, the use of acid or base treatment following LbL self-assembly allowed development of porous films (Figures 2-7 and 2-8).^{72,73} The Shiratori group recently reported that the use of metal ions afforded wide-range control of the pore size of a polyelectrolyte structure displaying porosity (Figure 2-9).⁷⁴ Nevertheless, the creation of porous films with multiple functions is still faced with considerable obstacles, in spite of the advances that have been made so far. These obstacles include anti-reflection (AR) property, biocompatibility and durability, as well as the use of cost-effective and sustainable materials and techniques that are not dependent on size or shape.^{75,76}

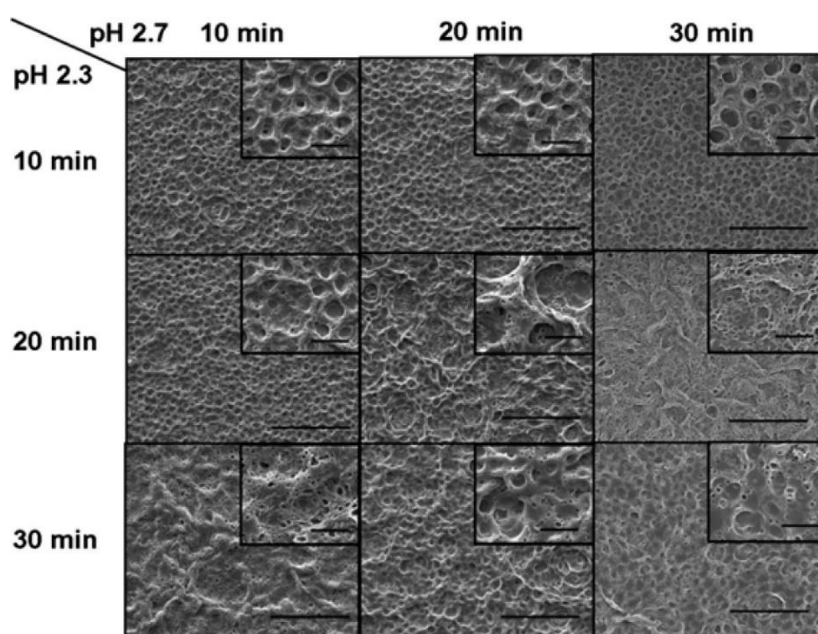


Figure 2-7. SEM images showing the development of porous structures of (BPEI_{6.5}/PAA_{4.5})₃₀ films *via* staged acid treatment. The porous structures are shown magnified in the inset of each image. Low magnification images have a scale bar of 100 μ m while high magnification images have a scale bar of 20 μ m. Reproduced with permission from Ref [72].

Copyright 2013 American Chemical Society.⁷²

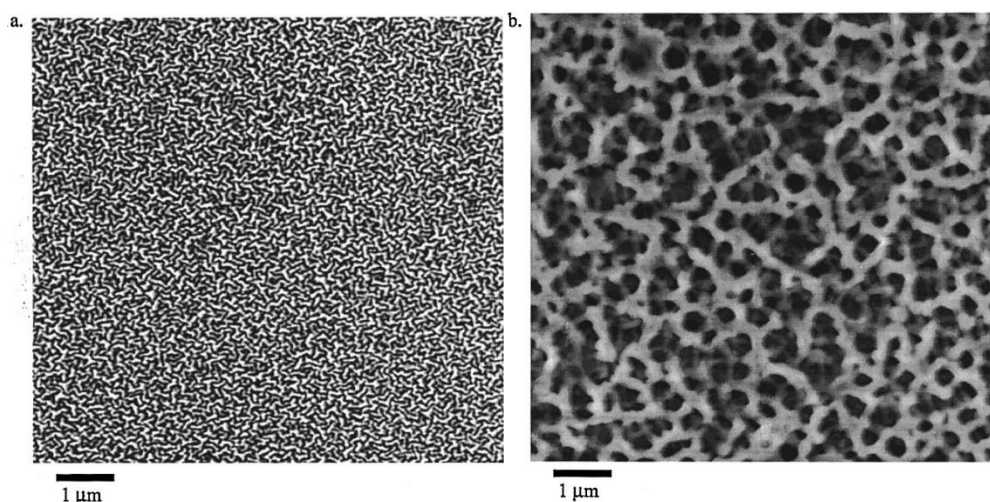


Figure 2-8. The surface of a 21-layer 3.5/7.5 polyelectrolyte multilayer film is shown in an AFM image prior to (a) and after (b) it was immersed in an acidic transition bath ($\text{pH} = 2.5$). The films are respectively 950 and 2790 Å thick and have a refractive index of 1.54 and 1.18. Reproduced with permission from Ref [73]. Copyright 2000 American Chemical Society.⁷³

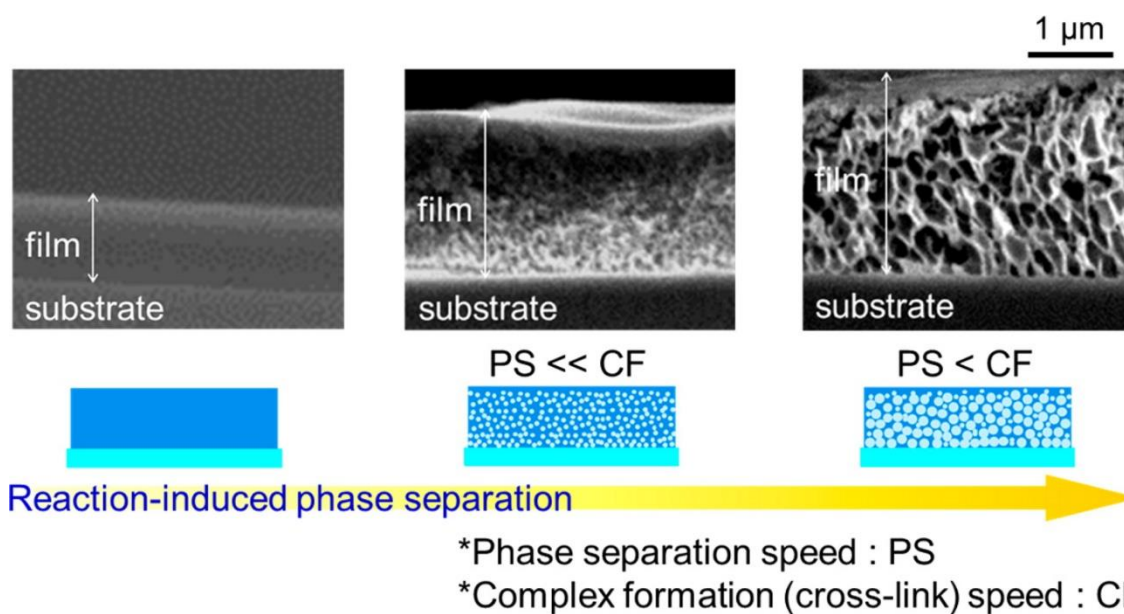


Figure 2-9. Cross-sectional SEM images and diagram illustrating the deduced formation process of polyelectrolyte films displaying porosity *via* phase separation triggered by reaction. Every image has a scale bar of 1 μm. Reproduced with permission from Ref [74]. Copyright 2016 American Chemical Society.⁷⁴

2.2 Surface Wettability

The contact angle representing the angle between a solid surface and liquid drop defines the phenomenon of wetting. This angle depends on the structure of the surface, its energy, how rough it is and how clean it is.

A contact angle with a value of water in the range of $0-90^\circ$ confirms the wetting and hydrophilicity of the surface. On the other hand, a contact angle with a value of water exceeding 90° confirms the non-wetting and hydrophobicity of the surface. Furthermore, a surface is superhydrophobic if the contact angle exceeds 150° , as the drop appears nearly round on the surface (Figure 2-10). Meanwhile, surface energy is susceptible to alteration *via* fluorination, for instance, in the case of most materials, contributing to augment hydrophobicity. Similarly, changes in surface roughness allow changes in hydrophobic or hydrophilic character. Figure 2-10 presents the wetting modes highlighted above alongside contact angles.

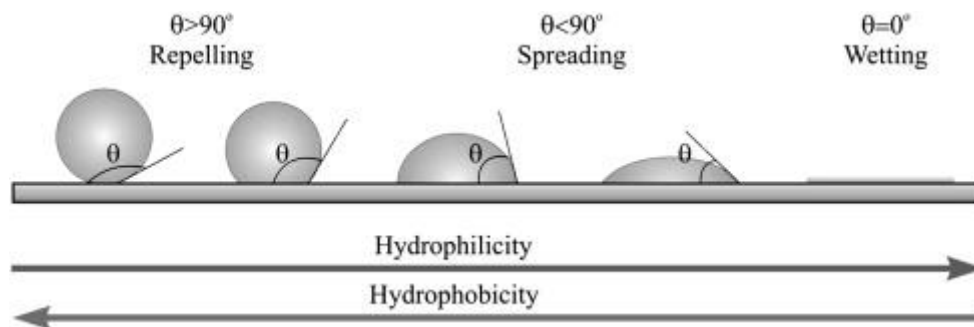


Figure 2-10. The phenomenon of wetting and the associated modes of hydrophobicity and hydrophilicity. Reproduced from Ref [77] with permission of Elsevier (Copyright 2009).⁷⁷

2.2.1 Wetting Models

The value of the contact angle facilitates the measurement of the hydrophobic mode. The contact angle permits assessment of hydrophobicity or hydrophilicity, which occurs between liquid, solid and gas phases. There is significant variation in the parameters that regulate contact angle development, which is why identification of reproducible contact angles in systems can be difficult. For purposes of demonstration of the different states, various contact angle equations and situations have been devised. Young's equation, Wenzel's equation and the Cassie-Baxter equation are the most important models that have been developed. Wetting on a smooth surface is characterised by Young's equation, while wetting on a rough surface is characterised by the other two equations. The three equations are all illustrated in Figure 2-11, with surface roughness being considered in the case of Wenzel's equation and the Cassie-Baxter equation.

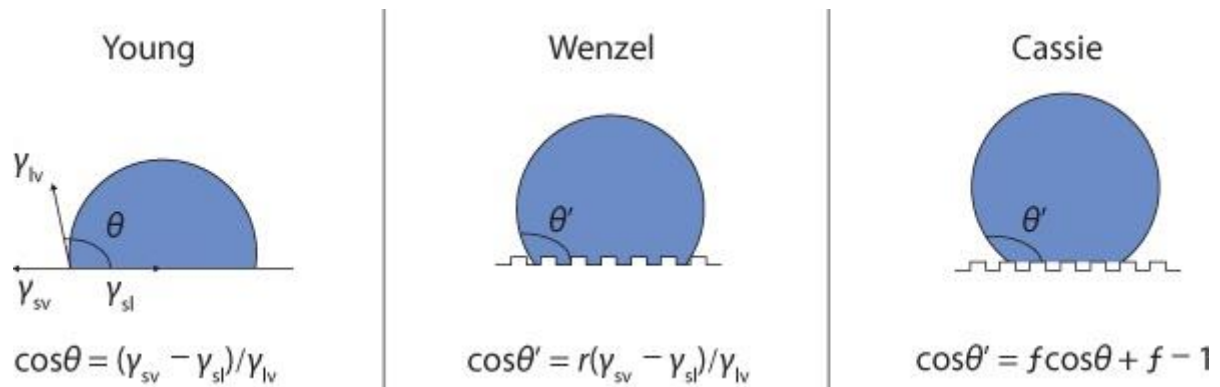


Figure 2-11. Young's, Wenzel's and Cassie-Baxter's equations (Nakajima, 2011); a liquid droplet is shown on a solid surface, with three interphases (γ) developing the contact angle (θ), namely, solid-liquid (SL), liquid-vapour (LV) and solid-vapour (SV). Fractional area f_1 with contact angle θ_1 and fractional area f_2 with θ_2 ($f_1 + f_2 = 1$) are the fractions constituting the rough surface in the Cassie-Baxter equation. Reproduced from Ref [78] with permission of Nature (Copyright 2011).⁷⁸

2.2.2 Superhydrophobicity

A surface that is water repellent to an extreme degree is said to display superhydrophobicity. This property or other self-cleaning capability is exhibited by numerous biological surfaces. In a superhydrophobic or solid-air composite surface, the air is shut in beneath a droplet of water among the surface texture bumps.^{79,80} Many studies have shown that hydrophobic surfaces from nature have at their core the micro or nanostructure and ample endeavours have been dedicated to shedding light on the structural complexities of such surfaces.

A particular level of energy is required to disrupt the chemical bonds that occur between molecules on a surface. Compared to molecules that form bonds at the surface, the potential energy of molecules without bonds is greater and is known as surface free energy. As explained by Nosonovsky and Bhushan,⁸⁰ the round shape adopted by droplets and bubbles on a surface is the result of a system's attempt to achieve a state of least amount of energy. The development of a hierarchical surface is the outcome of the specific arrangement of elements of varying defining lengths and is associated with a particular functionality. Superhydrophobicity has been attributed to the hierarchical configuration of nature's own surface and is considered to be augmented by hierarchical structures. Water droplets easily sit on the nanostructure as the empty spaces under them in the porous structure are filled by air bubbles.^{81–83} Superhydrophobicity is enabled by the fact that the droplets of water are prevented from coming into full contact with the surface by the air trapped in the structure.

The areas in which synthetic superhydrophobic coatings can be applied are limited due to the fact that they do not withstand physical forces very well. Superhydrophobic surfaces can be irreversibly damaged by deterioration owing to sunlight, wind erosion, and dirt. Usually, repair of such damage requires redeposition, which can be costly or untenable for a given application.⁸⁴

2.2.3 Liquid-Impregnated Surfaces (LIS)

A solid-liquid composite surface with infusion of liquid rather than air into the pores could be a viable solution for the creation of superhydrophobic surfaces. David Quéré pioneered this solution when he proposed the notion of liquid-infused texture in 2005.⁸⁵ The underlying assumption was that a drop of immiscible liquid deposited on an infused surface would not adhere to the surface but float on it. In addition to anticipating that this kind of composite surface would be capable of self-cleaning, Quéré also conjectured the attributes of the optimal surface texture and its most appropriate dimensions and shape.⁸⁵

2.2.4 Slippery Liquid-Infused Porous Surfaces (SLIPS)

The Aizenberg group drew inspiration from the *Nepenthes* pitcher plants for the development of the slippery liquid-infused porous surface (Figure 2-12).²² Preparation of this kind of surface involved impregnation of a nanoporous or microporous surface with a hydrophobic and water immiscible liquid. The creation of a slippery surface that can repel various liquids, including water, ice and oil, can be achieved by ensuring that the surface energies of the porous substrate and the liquid are equivalent. Furthermore, evidence has been provided in support of the self-healing capability of the surface and the fact that it remained stable under high pressure. The porous substrate consisted of arrays of nanoposts with functionalization based on perfluoroalkyl silane and Teflon nanofibres available in commerce. Meanwhile, perfluorinated liquid with low surface tension (e.g. 3M Fluorinert FC-70 and DuPont's Krytox oils) was used for the lubricant liquid. Fluorinated nanostructured silicon or porous Teflon substrates displaying roughness represented the foundation for the liquid-infused surface proposed by the Aizenberg group.²²

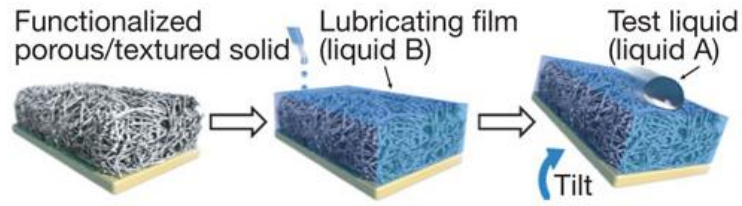


Figure 2-12. Schematic image of SLIPS composed of a hydrophobic underlayer and a lubricant layer. Reproduced from Ref [22] with permission of Nature (Copyright 2011).²²

A porous or textured solid combined with a liquid lubricant whose stability is ensured by capillary forces constitutes the composition of a lubricant-infused surface. A range of new properties is derived from the interface between such a surface and an immiscible liquid that it touches, which is known as the working fluid. Lubricant displacement by the working fluid will not occur provided that the system design is effective.

The complexity of the boundary between a working fluid drop and a lubricant-infused surface is greater than the single three-phase contact line between water, air and solid that is created by a water drop on a solid surface. As shown in Figure 2-13, three different morphologies of a lubricant-infused surface under a working fluid drop can be distinguished, according to the energetics of the component materials (i.e. working fluid, lubricant and solid).²⁶ The impaled state is associated with lubricant displacement by the working fluid, which touches the solid in every area beneath the drop. In the infused, emerged state, the solid continues to trap the lubricant and just the exposed features are touched by the working fluid. The encapsulated state is characterised by total lack of contact between the working fluid and the solid. This state is also the most slippery, according to measurement based on the roll-off angle. By contrast, the least slippery state is the impaled state, which is thus comparable to the Wenzel state on a surface displaying superhydrophobicity.²⁶

Quantification of the above three states can be achieved on the basis of their total interfacial energy (Figure 2-13). The steady state will be associated with the least amount of total interfacial energy. For the impaled state, impregnated, emerged state and encapsulated state, the total surface energy per area is respectively $E_{w1} = r\gamma_{sw}$, $E_{w2} = (r - \varphi)\gamma_{os} + \varphi\gamma_{ws} + (1 - \varphi)\gamma_{ow}$ and $E_{w3} = \gamma_{ow} + r\gamma_{os}$. In these relationships, r and φ respectively represent the overall surface area of the solid normalised by the projected area and the solid fraction touching the working fluid in the impregnated, emerged state, while the interfacial tension between components “ i ” and “ j ” (“ w ” for working fluid, “ o ” for lubricant, and “ s ” for solid) is indicated by γ_{ij} . When $S_{os}(w) = \gamma_{sw} - \gamma_{ow} - \gamma_{os} > 0$, the encapsulated state takes precedence over the emerged state $E_{w3} < E_{w2}$, with $S_{os}(w)$ denoting the spreading coefficient of “ o ” on “ s ” in the presence of “ w ”. Experimental determination of spreading coefficients relies on observation of the spread of a lubricant drop on an even solid within the working fluid. To prevent gravity from influencing the spread, the capillary length $\ell_c = (\gamma/\rho g)^{1/2}$ should be greater than the drop size R . In this relationship, the surface tension of the spreading liquid, its density and the gravitational acceleration are respectively denoted by γ , ρ and g .⁸⁶ $S_{os}(w) > 0$ if the lubricant is observed to spread, with the encapsulated state being available for a textured solid of identical chemical configuration. Figure 2-13 provides an overview of these observations.

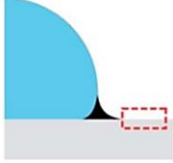
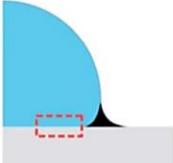
Interface	Configuration	Total interface energy per unit area	Equivalent criteria		
Oil-Solid-Air 	A1 Dry	$E_{A1} = r\gamma_{sa}$	$E_{A1} < E_{A2}, E_{A3}$	$S_{os(a)} < -\gamma_{oa}\left(\frac{r-1}{r-\phi}\right)$	$\theta_{os(a)} > \theta_c$
	A2 Impregnated, emerged	$E_{A2} = (r-\phi)\gamma_{os} + \phi\gamma_{sa} + (1-\phi)\gamma_{oa}$	$E_{A2} < E_{A1}, E_{A3}$	$-\gamma_{oa}\left(\frac{r-1}{r-\phi}\right) < S_{os(a)} < 0$	$0 < \theta_{os(a)} < \theta_c$
	A3 Encapsulated	$E_{A3} = \gamma_{oa} + r\gamma_{os}$	$E_{A3} < E_{A2}, E_{A1}$	$S_{os(a)} \geq 0$	$\theta_{os(a)} = 0$
Oil-Solid-Water 	W1 Impaled	$E_{W1} = r\gamma_{sw}$	$E_{W1} < E_{W2}, E_{W3}$	$S_{os(w)} < -\gamma_{ow}\left(\frac{r-1}{r-\phi}\right)$	$\theta_{os(w)} > \theta_c$
	W2 Impregnated, emerged	$E_{W2} = (r-\phi)\gamma_{os} + \phi\gamma_{sw} + (1-\phi)\gamma_{ow}$	$E_{W2} < E_{W1}, E_{W3}$	$-\gamma_{ow}\left(\frac{r-1}{r-\phi}\right) < S_{os(w)} < 0$	$0 < \theta_{os(w)} < \theta_c$
	W3 Encapsulated	$E_{W3} = \gamma_{ow} + r\gamma_{os}$	$E_{W3} < E_{W1}, E_{W2}$	$S_{os(w)} \geq 0$	$\theta_{os(w)} = 0$

Figure 2-13. Diagram of wetting architectures external to and beneath a drop (column 2). The sum of the individual interfacial energies gives the total interface energy per unit area (column 3). Column 4 indicates corresponding specifications for the stability of every configuration. “Oil” and “water” respectively represent the lubricant and the working fluid. Reproduced from Ref [26] with permission from The Royal Society of Chemistry (Copyright 2013).²⁶

As highlighted by the previous equations, the lubricant-infused surfaces of the greatest stability are lubricants and solids with low surface energy, such as fluorocarbons, fatty alcohols, hydrocarbons and silicone oils. Ionic liquids have been suggested to be a better option than lubricants because the latter determine the loss of properties of the lubricant-infused surface when they evaporate.⁸⁷ By contrast, ionic liquids have minimal vapour pressures, although they do not occur in the encapsulated state, but only in the impregnated, emerged state.²⁶ Materials with low energy, such as PTFE membranes or other materials considered to possess hydrophobicity, such as silicon, SU-8 and aluminium, are employed as porous or textured

solids. The creation of a texture for the formation of a lubricant-infused surface is the same as the creation of a texture for achievement of a surface with superhydrophobicity.

It is possible for the lubricant oil to spread over and cover the repelled liquid droplet. The spreading coefficient of oil on water in the presence of air determines the criterion for cloaking occurrence:

$$S_{ow(a)} = \gamma_{wa} - \gamma_{wo} - \gamma_{oa} \quad (2-11)$$

In the above, γ and w are the interfacial tension between phases and the repelled liquid, respectively. Cloaking will happen only if $S_{ow(a)} > 0$ but not if $S_{ow(a)} < 0$. For instance, $S_{ow(a)} \sim 6 \text{ mNm}^{-1}$ was demonstrated to be a cloaking lubricant for silicone oil. Meanwhile, negative spreading coefficients have been observed in the case of some lubricants, like ionic liquid. Figure 2-13 illustrates these two cases. Aside from shedding light on the actual physical state of the system, cloaking also helps to understand how the cloaked lubricant is gradually lost *via* entrainment in the droplets of water during surface cast off.

Chapter 3

Optically Functionalized SLIPS

3.1 Background

Insufficient research has been conducted on surfaces with superhydrophobicity capable of super-repellency, preventing fogging and frosting as well as of removing frost,^{88,89} which calls for the development of transparent films with superhydrophobicity that are capable of withstanding fluctuations in temperature lower than zero.

Plausible solutions drawing on the properties of *Nepenthes* pitcher plants have been proposed by Aizenberg and colleagues to address these limitations.^{22–25} Transmission is intensified when a porous film is filled with lubricant as a result of a reduction in reflectance at the solid-gas interface and scattering by the nano/microstructure. The referenced studies have argued that, if a film with superhydrophobicity, high transmittance and low reflectance were used as the base for the lubricant, then SLIPS would be capable of high transmittance. Solar panels and intelligent windows could benefit from a thermo-responsive slippery fluid-infused film demonstrating transparency and anti-fouling effect.

Moth eyes, with their graded refractive index and relief architectures for reducing reflection, constituted the inspiration of this kind of film.⁹⁰ These architectures are replicated by multilayer thin films formed *via* the technique of LbL assembly,⁹¹ in which materials with opposite charges are adsorbed alternately *via* electrostatic attraction.^{39,92–94} Characterised by convenience, flexibility and straightforwardness, this technique is applied at ambient temperature and pressure,^{95–97} and permits regulation at micro/nanoscale of a film's thickness

and surface texture and wettability. LbL films made of nanofibres or nanoparticles typically display a low refractive index and are highly porous.^{98–100} The technique has enabled the creation of films with the properties of anti-reflection,¹⁰¹ replicating moth eyes, superhydrophobicity,⁵⁶ replicating lotus leaves, and omniphobicity,⁷² replicating pitcher plants. However, no success has yet been recorded regarding the development of SLIPS with transmittance exceeding 95% based on a wet process.^{23–25} The LbL assembly technique could not ensure high transmittance in spite of the challenge of regulating surface texture, film thickness and optical abilities. Nevertheless, the uncomplicated technique of nanoscale phase separation did enable the development of gel-SLIPS.¹⁰² Hence, there is the great potential in developing highly transparent SLIPS and additional traits (e.g. sensitivity to stimuli) through the LbL technique.^{103–105} Temperature discrepancies between the two facets of glass windows and lenses create frosting, which highlights the necessity to develop anti-frosting films that are anti-reflective to make up for the fact that their reflectance is influenced by changes in liquid surface density. Car window frosting has been a long-standing issue in certain regions, necessitating temperature increase within the vehicle before it can be removed.

Several types of films are presented in the following part, namely, LbL assembly-based film with superhydrophilicity and anti-reflection containing chitin nanofibers (CHINFs) and silica nanoparticles (SiO₂) and known as *moth-eye film*, fluoroalkylsilane-hydrophobized ten-bilayer *moth-eye film*, which is a film with transparency and superhydrophobicity known as *lotus film*, and *lotus film* coated in lubricant oil known as slippery fluid-impregnated anti-reflective film or *pitcher film* (Figure 3-1 and Figure 3-2). Compared to earlier studies, a higher transmittance can be attained through this three-stage replication owing to the accomplishment of an omniphobic coating. Furthermore, comparative analysis of temperature-based film alterations with three types of surface wettability (i.e. superhydrophilicity, superhydrophobicity and liquid-infused) clarifies how the anti-frosting property of the *pitcher*

film works. These three types of surface wettability have never been compared with one another and therefore could shed new light on how films are affected by lubricant oil.

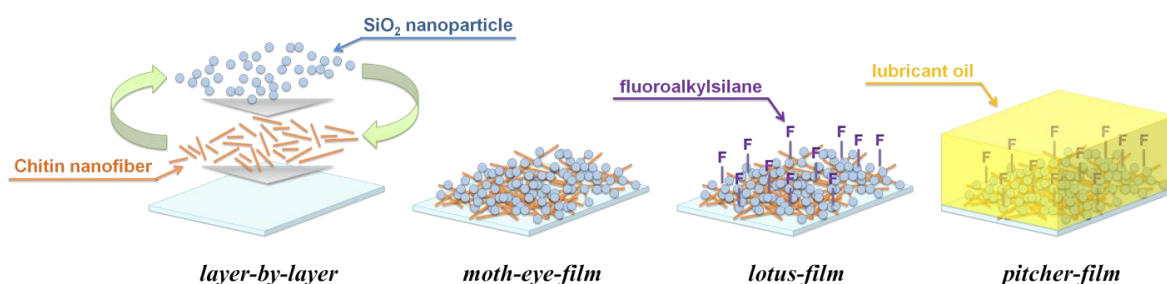


Figure 3-1. Schematic representation of each of the three film types, namely, LbL assembly-based *moth-eye film* with antireflection and comprising CHINFs and SiO₂, and *lotus* and *pitcher films* with superhydrophobicity and lubricant infusion, respectively, developed based on functionalization of ten-bilayer *moth-eye film*. Reproduced with permission from Ref [106]. Copyright 2014 American Chemical Society.¹⁰⁶

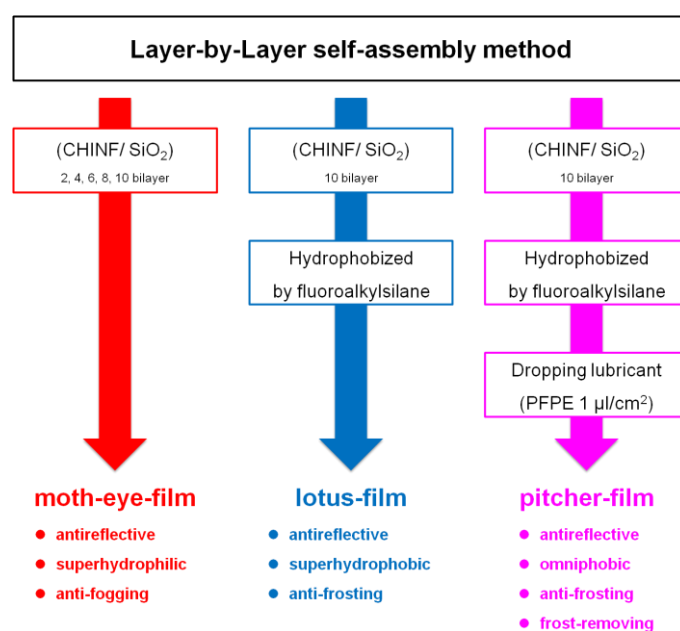


Figure 3-2. Summary of empirical protocols and the characteristics of the three film types. Reproduced with permission from Ref [106]. Copyright 2014 American Chemical Society.¹⁰⁶

3.2 Experiment

3.2.1 Materials

Film production involved the following materials: crab shells (Kawai Hiryo, Iwata, Japan), colloidal silica nanoparticles (SiO_2 , $\phi \sim 30$ nm, Nissan Chemical Industries, Ltd., Japan), perfluoropolyether (PFPE) (Krytox GPL 103, $\gamma = 17.4$ mN m^{-1} , Dupont, USA), tridecafluoro-2-(tridecafluorohexyl) decyltrichlorosilane (Gelest, Inc., USA), and glass substrates (76×26 mm, thickness = 1.0 mm, refractive index = 1.52, Matsunami Glass Ind., Ltd., Kishiwada, Japan). Ultra-pure water (Aquarius GS-500.CPW, Advantec, Japan) was used to prepare each LbL dipping suspension, while CH_3COOH (Kanto Chemical Co, Inc., Tokyo, Japan) was used to modulate the pH of the suspensions. KOH solution (1:120:60 wt% KOH/ H_2O /IPA) was used to clean the glass substrates for 120 seconds, after which ultra-pure water was used to rinse them, getting them ready for usage.

3.2.2 Chitin nanofibre preparation

The preparation of CHINFs began with purification of the crab shells in keeping with the guidelines from previous studies.^{107,108} This involved removal of mineral salts through treatment of the crab shell powder in 2 M of hydrochloric acid (Kanto Chemical Co, Inc.) for a period of 48 hours at room temperature. Subsequently, the treated chitin powder was rinsed with distilled water and subjected to heating under reflux in 2 M sodium hydroxide (Kanto Chemical Co, Inc.) for a period of 48 hours for the purpose of protein removal. A quantity of 1.7 wt% sodium chlorite (Kanto Chemical Co, Inc.) in buffer solution was used over a period of six hours at a temperature of 80°C to eliminate sample pigment. After rinsing with distilled water, sample suspension in 33 wt% sodium hydroxide with 0.03 g sodium borohydride (Kanto Chemical Co, Inc.) was performed as described in a previous study.¹⁰⁹ The suspension was

centrifuged more than once at 5000 rpm for five minutes to wash it with pure water. This was followed by dilution of the CHINF suspension to 0.025 wt% and dispersal *via* ultrasonication.

3.2.3 Film with superhydrophilicity and antireflectivity

The LbL technique was applied to develop layers with superhydrophilicity, antireflectivity and low refractive index based on prepared CHINFs and SiO₂ suspensions. This involved alternate immersion of a glass substrate into 0.025 wt% CHINF cationic suspension (pH 3) and 0.03 wt% SiO₂ anionic suspension (pH 3) for an interval of 60 seconds. Pure water was then used to rinse the substrate for 180 seconds, followed by air-drying at 10 mm distance and 0.05 MPa once each layer was deposited. The glass substrate was coated on film over around two-thirds of its surface, while the remaining surface remained uncoated.

3.2.4 Film with superhydrophobicity and transparency

The gas phase technique was applied in the creation of layers demonstrating transparency and superhydrophobicity. This involved introducing a ten-bilayer CHINF/SiO₂ antireflective film into a plastic bottle with a volume of 100 mL and a glass bottle with a volume of 2 mL that held 200 μ L of tridecafluoro-2-(tridecafluorohexyl) decyltrichlorosilane. The whole system was then treated thermally for 150 minutes at a temperature of 70°C.

3.2.5 Slippery film with fluid infusion and antireflectivity

Addition of 1 μ L cm⁻² PFPE to a *lotus film* was performed in a drop-wise manner. The thickness of the PFPE layer was around 1 μ m. A nitrogen gas blow was used to eliminate any extra PFPE from the film.

3.2.6 Characterization

For the purpose of characterizing film surface structures, imaging was performed using a field emission scanning electron microscope (FE-SEM) and an energy-dispersive X-ray spectrometry (EDX) (S-4700, Hitachi, Japan) with 3 kV accelerating voltage. Furthermore, a spectrophotometer (UVmini-1240, Shimadzu, Kyoto, Japan) permitted transmittance to be measured in the spectral range 300-1000 nm, while atomic force microscopy (AFM, Nanoscope IIIa, Digital Instruments, USA) was applied to evaluate how rough the films were. Ellipsometry (MARY-102, Five Lab, Japan) facilitated evaluation of how thick the films were as well as what the refractive index of ultrathin films covering the glass substrate was. Furthermore, a contact-angle meter (CA-DT, Kyowa, Japan) enabled measurement of contact and sliding angles, while a haze meter (NDH-5000, Nippon Denshoku Industries, Tokyo, Japan) employing a diode with white light emission (5 V, 3 W) as a source of light enabled measurements of film total transmittance (T.T.), parallel transmittance (P.T.), diffusion (DIF) and haze values (HAZE).

3.2.7 Anti-frosting property test

A glass substrate, ten-bilayer film with superhydrophilicity, film with superhydrophobicity and slippery fluid-infused antireflective film were all placed on a Peltier cooling unit in a thermo-hygrostat under conditions of 10°C and relative humidity of 80%, with progressive cooling of the Peltier unit in the range of 10 to -10°C. A digital camera was used to document the process photographically, and thermography (PI400, Optris, USA) permitted monitoring of temperature fluctuations. The capacity to remove frost was evaluated by heating the unit to 30°C once every film was frosted.

3.3 Results and Discussion

The Fresnel equations⁵³ specify that a zero reflection for an optimal uniform single-layer anti-reflective coating requires the film on the glass substrate to have a refractive index of

$$n_l = \sqrt{n_{air}n_{substrate}} = \sqrt{1.52} \approx 1.23 \quad (3-1)$$

where n_l , n_{air} , and $n_{substrate}$ are the refractive indices of the low-refractive-index film, the air, the substrate, respectively. For the vertical incidence, there would be 0% surface reflectance and transmittance of light at a specific wavelength, provided that the medium thickness corresponds to one-quarter of the wavelength. The following straightforward mixing rule enables to measure of the refractive index of a LbL film:¹¹⁰

$$n_l = f_{air}n_{air} + f_{nanoparticle}n_{nanoparticle} + f_{polyelectrolyte}n_{polyelectrolyte} \quad (3-2)$$

The volume fraction of component x is denoted by f_x and the refractive index is n_x . Based on this equation, the refractive index of LbL film has to be reduced in order to enhance porosity.

Relief structure and low surface energy are additional requirements for the films with superhydrophobicity.¹¹¹ The nano/micro complex surface that usually makes up the relief structure is significantly rough, which intensifies light scattering to deteriorate the transmittance, according to predictions by the optical theory associated with multilayer coating.^{112–116}

$$\ln(T/T_0) = -\{2\pi(n_{air} - n_l)\cos\theta\}^2(\sigma/\lambda)^2 \quad (3-3)$$

Multilayer transmittance with surface roughness is denoted by T , while multilayer transmittance without surface roughness is denoted by T_0 . The optical incident angle to the most exterior surface layer is denoted by $\cos\theta$, while σ and λ respectively represent the RMS surface roughness and the wavelength. Provided that the variables have the following values $T/T_0 = 0.98$, $\sigma/(\lambda \times 10^{-3})$, $\lambda = 550$ nm and $\theta = 0$, then the value of the RMS surface roughness will be 54.45 nm. Consequently, to ensure a transmittance higher than 98% and

prevent it from declining as a result of scattering loss, RMS surface roughness must not exceed 54.45 nm.

Given the considerations outlined above, it is important for the films used in the present study to attain a 1.23 refractive index in the film with superhydrophobicity and a 150° contact angle, which will require sufficiently low surface roughness.

3.3.1 Films with superhydrophilicity and antireflectivity

The LbL assembly technique was applied to develop the films with superhydrophilicity and antireflection, otherwise known as *moth-eye films*. As shown in Figure 3-3, the rise in the bilayer count determined a linear increase in the film thickness and a reduction in refractive index, the minimal value of which was 1.20. The CHINFs provided little electrostatic assistance (Figure 3-4), affording porosity and a particle-predominant composition to the film structures (Figure 3-5A). On the long wavelength side, light scattering by Rayleigh scattering was circumvented because there was close similarity between CHINF diameter and the nanoparticle dimensions (< 50 nm). RMS surface roughness (R_q) and R_a increased as the film structure became thicker (Figure 3-5C).

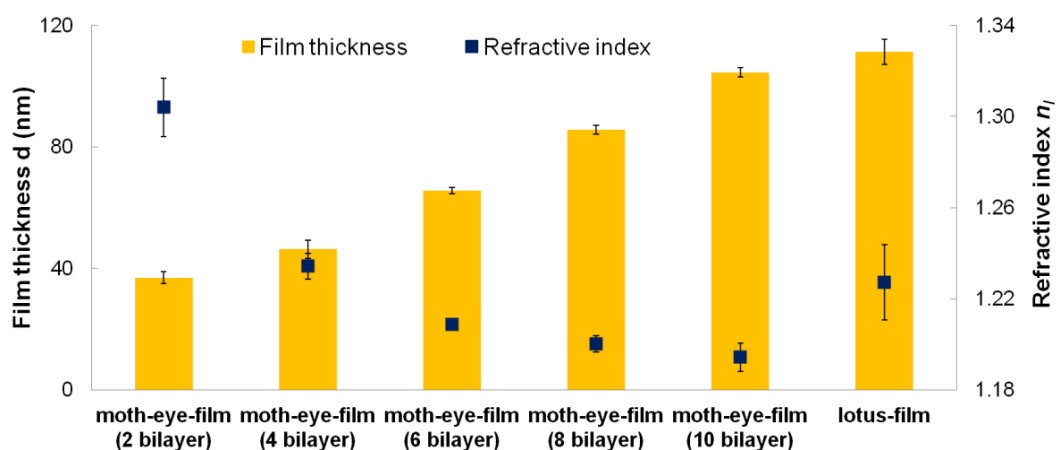


Figure 3-3. Ellipsometry-based measurement of superhydrophilic and anti-reflective films with varying numbers of bilayers and superhydrophobic film, with the thickness and refractive index of the films being indicated by the yellow bars and blue squares, respectively. Reproduced with permission from Ref [106]. Copyright 2014 American Chemical Society.¹⁰⁶

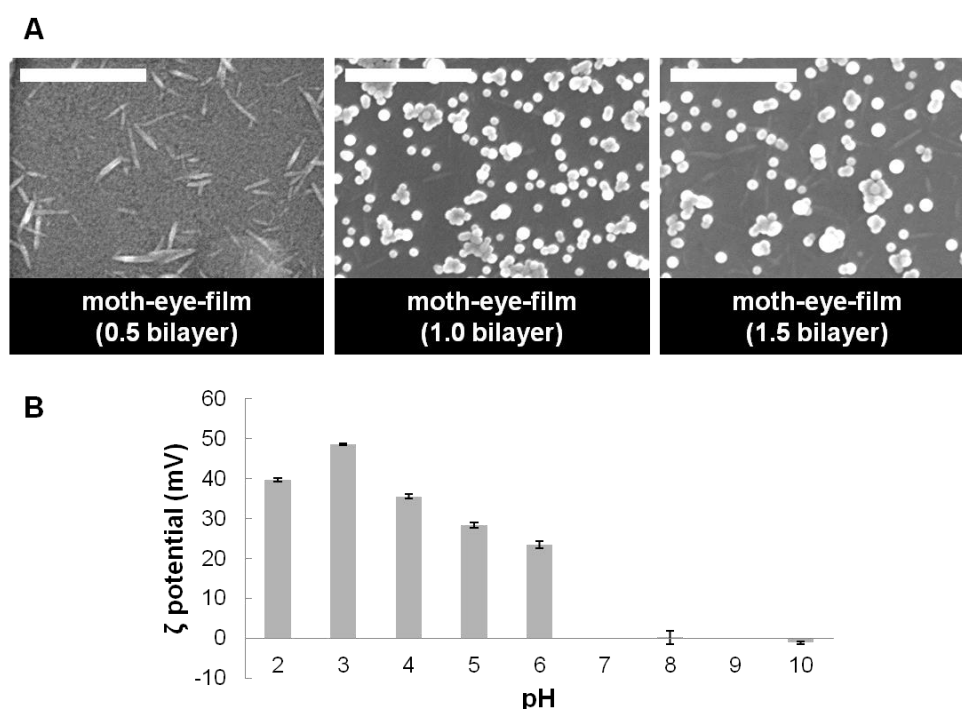


Figure 3-4. (A) Superhydrophilic and anti-reflective films imaged with FE-SEM on separate bilayers at 1 μm scale bar. (B) Zeta potential of CHINF solutions of varying pH. As cationic material, CHINF was intended to help SiO₂ nanoparticles to attach to the glass substrate but without coating them. Surface electrostatic bias occurred because of CHINF adherence to the glass substrate in some areas. As shown in the FE-SEM image of 1.0 bilayer of superhydrophilic and anti-reflective film, attachment of SiO₂ nanoparticles occurred in the areas with CHINF, while the FE-SEM image of 1.5 bilayer of superhydrophilic and anti-reflective film shows that next generation CHINF attached to the glass substrate without touching the SiO₂ nanoparticles. Reproduced with permission from Ref [106]. Copyright 2014 American Chemical Society.¹⁰⁶

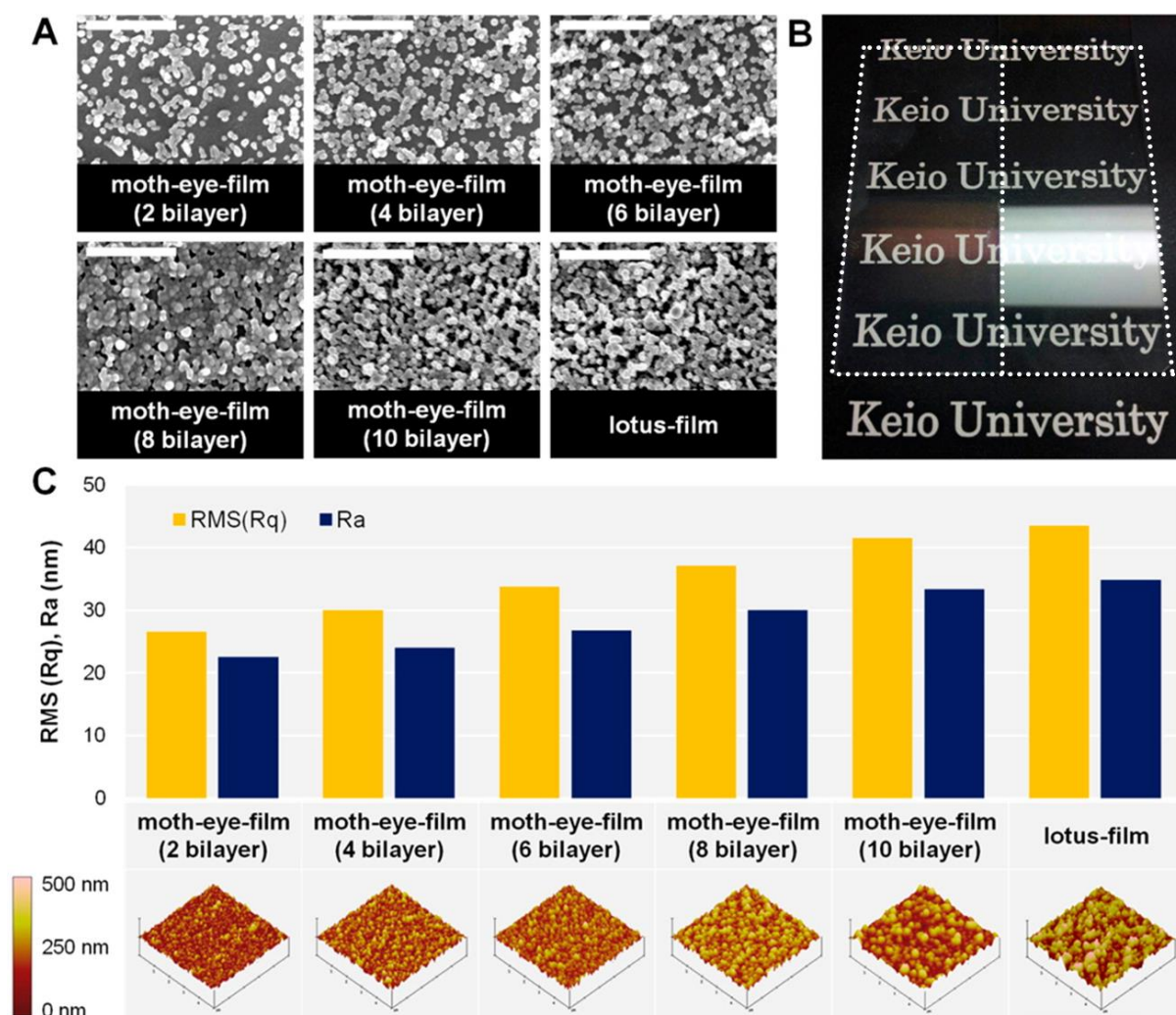


Figure 3-5. (A) Superhydrophilic and anti-reflective films with various numbers of bilayers and superhydrophobic film imaged with FE-SEM at 1 μm scale bar. (B) Ten-bilayer superhydrophilic and anti-reflective films (left) and glass substrate (right) imaged under fluorescent light. (C) Superhydrophilic and anti-reflective films with varying numbers of bilayers and superhydrophobic film with their surface roughness measured by RMS (Rq) and Ra, denoted by the yellow bars and blue squares, respectively; the equivalent AFM images are provided underneath. The scan size (x and y) and data scale (z) are 5 μm and 500 nm, respectively. Reproduced with permission from Ref [106]. Copyright 2014 American Chemical Society.¹⁰⁶

As illustrated in Figure 3-6, ten-bilayer superhydrophilic and anti-reflective film was associated with the maximum transmittance of 96.7% at 726 nm. The reason for this result is that the progressively increasing refractive index towards the glass substrate caused a reduction in reflectance. Stable electrostatic interaction facilitated the development of the films. Hence, deposition of alternate layers gave rise to a layer with refractive index that was not as high as that of the preceding layer. Reflectance was around 4% when the interface refractive index increased from 1.0 to 1.5. As seen in Figure 3-7, the progressive alteration of the refractive index by 0.1 towards the glass substrate resulted in each interface reflectance of around 0.1-0.2% and total reflectance of around 0.8%. Calculation of reflectance was straightforward as the powerful electrostatic interaction ensured the stability of every layer (Figure 3-7). In fact, by comparison to the glass substrate, the ten-bilayer superhydrophilic and anti-reflective film exhibited low reflectance under fluorescent light (Figure 3-5).

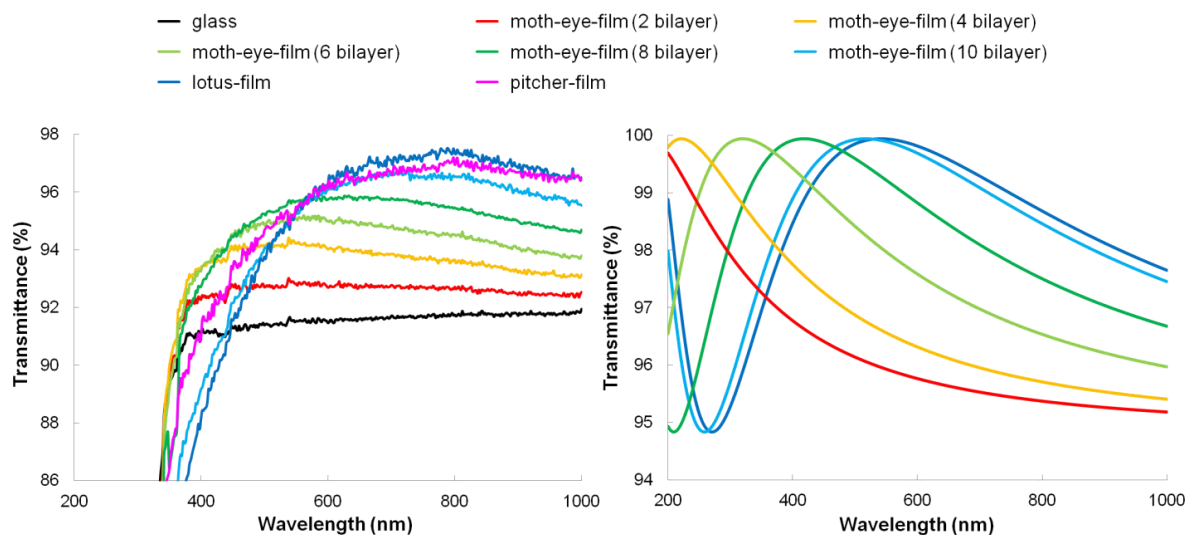


Figure 3-6. Transmittance changes of the fabricated films (left). Apart from slippery fluid-infused film, optical simulation software (Design, Tecwave) was applied to determine transmittance modifications of every film with constant 1.23 refractive index (right). Transmittance in air was determined for the glass substrate (black line), superhydrophobic and

anti-reflective films with two (red line), four (yellow line), six (lime green line), eight (green line) and ten (aqua line) bilayers, as well as for the superhydrophobic film (blue line) and slipper fluid-infused film (pink line). Reproduced with permission from Ref [106]. Copyright 2014 American Chemical Society.¹⁰⁶

The gap of refractive index on surfaces is what causes light to reflect on material surfaces. Fresnel's equations specify how surface reflectance can be calculated:

$$R = \left\{ \frac{(n_2 - n_1)}{(n_2 + n_1)} \right\}^2 \quad (3-4)$$

The refractive index of medium 1 is denoted by n_1 while the refractive index of medium 2 is denoted by n_2 . The gap of refractive index causes reflectance of around 4% of light as it penetrates the bare glass ($n_1 = 1.5$) from the air ($n_2 = 1.0$) (Figure 3-7). In contrast, the use of a moth-eye structure with projection that is small enough against the visible light wavelength as the reflecting surface determines a progressive modification in refractive index, and the average refractive index can be obtained through the equation below:

$$n_2 \times (\text{projection area ratio}) + n_1 \times (\text{air area ratio}) \quad (3-5)$$

Hence, the progressive increase in projection area ratio in the light travelling trajectory causes ongoing fluctuation in the average refractive index between n_1 and n_2 . However, disappearance of the refractive index gap does not lead to reflecting surface generation in the case of optimal moth-eye structures. Therefore, if the projection shape is regulated, it is possible to maintain reflectance at 0%. Moth-eye structures can be replicated by LbL films through the formation of a structure of progressive refractive index. Progressive modification in refractive index by 0.1 towards the glass substrate gives approximately 0.8% total reflectance on LbL films. In the present study, the refractive index was used to determine the reflectance for two bilayers (Figure 3-3), as shown below:

$$R = \left\{ \frac{(1.19-1.00)}{(1.19+1.00)} \right\}^2 + \left\{ \frac{(1.20-1.19)}{(1.20+1.19)} \right\}^2 + \left\{ \frac{(1.21-1.20)}{(1.21+1.20)} \right\}^2 + \left\{ \frac{(1.23-1.21)}{(1.23+1.21)} \right\}^2 + \left\{ \frac{(1.30-1.23)}{(1.30+1.23)} \right\}^2 + \left\{ \frac{(1.52-1.30)}{(1.52+1.30)} \right\}^2 \cong 1.4 \% \quad (3-6)$$

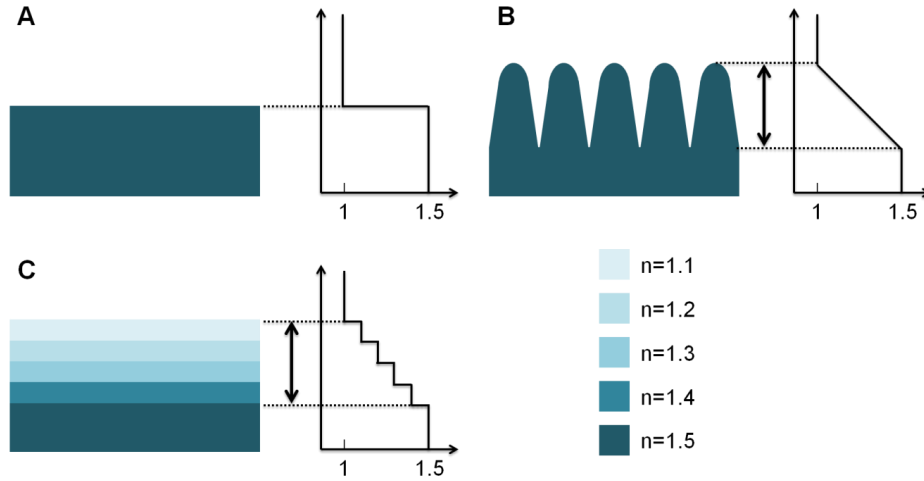


Figure 3-7. Diagram showing modifications in refractive index on bare glass (A), moth-eye structure (B) and LbL film (C). Reproduced with permission from Ref [106]. Copyright 2014 American Chemical Society.¹⁰⁶

The equation below is applied for the optical simulation software (Design, Tecwave) (Figure 3-6):

$$n = A + C/(\lambda - B) \quad (k = 0) \quad (3-7)$$

The refractive index and wavelength are respectively denoted by n and λ , while coefficients are denoted by A, B and C. A zero value is attributed to the material absorption coefficient (k) while wavelength dispersion is disregarded.

It is possible to make an antireflection coating with one layer non-reflective solely at a single wavelength. The normal incidence reflection coefficients can be employed to determine the reflection if the coating thickness is assumed to be 25% of the wavelength in the medium.

$$D = \lambda/4n_l \quad (3-8)$$

Hence, the maximum transmittance of a film D thick occurs at about $4Dn_l$ wavelength. Based on an optical simulation conducted in the present research, the maximum transmittance is exhibited by every bilayer film at a specific wavelength (Figure 3-6). Usually, a mid-range wavelength (e.g. 550 nm) is used in the production of antireflection coatings with one layer. For $n_l = 1.23$, $D \cong 112$ nm. In the case of incoming light with a wavelength below about 350 nm, the silica and glass substrate display a higher level of absorbance. Hence, since the wavelength associated with the highest transmittance is the same as or less than the absorption wavelength of SiO₂ and the substrate, the maximum transmittance of the six-bilayer superhydrophilic and anti-reflective film will not exceed that of films with eight or ten bilayers, even in the case of optimal refractive index. Absorbance of incoming light occurs in the case of eight-bilayer superhydrophilic and anti-reflective film, because its longer wavelength is close to the silica and substrate absorption wavelength. Furthermore, Rayleigh scattering intensifies dispersal in the proximity of the maximum transmittance wavelength as the RMS of this film exceeds one-tenth of the wavelength. This causes a reduction in the eight-bilayer superhydrophilic and anti-reflective film. Meanwhile, because its surface roughness is greater compared to other films, the ten-bilayer superhydrophilic and anti-reflective film is associated with intensification of short-wavelength light diffusion. This film is almost optimally thick (112 nm), which is why absorbance of incoming light does not occur close to the maximum transmittance wavelength of SiO₂ and substrate. Moreover, the refractive index alters more progressively in the case of LbL-based anti-reflective films of great thickness, despite the fact that scattering is intensified the rougher the surface is. Additionally, with the increase in the number of bilayers, the films resemble moth-eye structures more closely.

The refractive index distribution within the films is what hindered the achievement of 100% transmittance of each film. In the context of a non-heterogeneous medium, destructive interference eliminates all scattering intensity without alignment to the incident beam.

Therefore, the medium must have heterogeneous density and refractive index to permit observation of scattering intensity, and such a heterogeneity takes the form of variations. In particular, large variations are associated with high scattering intensity. Based on the theory outlined above, reduction of a film's refractive index can be achieved by expanding the air space in that film. On the downside, this gives rise to refractive index distribution and bias within the film. This leads to diffusion of incoming light, especially light of short wavelength, and less-than-optimal film transmittance.

3.3.2 Film with transparency and superhydrophobicity

Functionalisation of a ten-bilayer superhydrophilic and anti-reflective film with the maximum transmittance, surface roughness and minimal refractive index enabled formation of a film displaying high transparency and superhydrophobicity (*lotus film*). As shown in Figure 3-3, following gas-phase treatment, the temperature-based expansion in the elements of this film, particularly CHINFs, gave it greater thickness and refractive index than the superhydrophilic and anti-reflective film. For null reflectance, this refractive index was optimal on a glass substrate, while the film thickness was nearly optimal (112 nm). Furthermore, a minor increase in surface roughness accompanied the increase in film thickness (Figure 3-5). At 788 nm, the superhydrophobic film achieved the maximum transmittance of 97.5% (Figure 3-6).

F-containing fluoroalkylsilane altered the superhydrophobic film, as revealed by EDX imaging (Figure 3-8A). The film was also noted to include C and N of CHINFs and silica, suggesting that CHINFs and SiO₂ entered its composition as well.

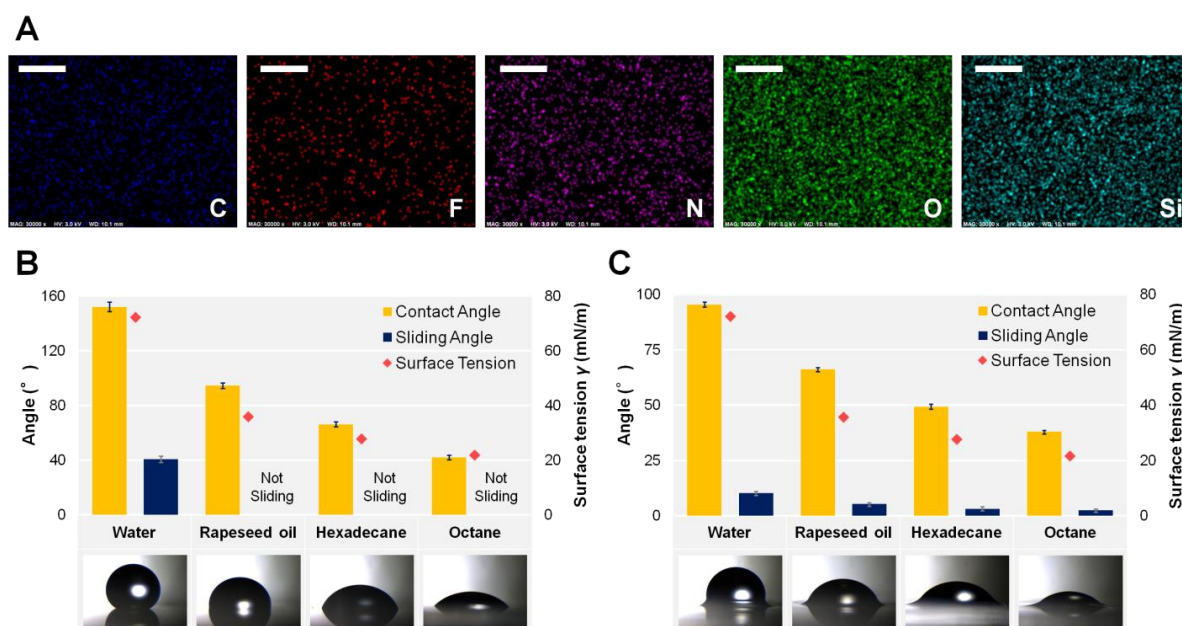


Figure 3-8. (A) Superhydrophobic film imaged with EDX at 1 μm scale bar. The graphs beneath indicate the contact angle, sliding angle and surface tension, respectively denoted by yellow and blue bars and red diamonds, of water, rapeseed oil, hexadecane and octane on a (B) hydrophobic film and (C) slippery fluid-infused film alongside images of all drops of liquid on the films. Reproduced with permission from Ref [106]. Copyright 2014 American Chemical Society.¹⁰⁶

The superhydrophobicity of the *lotus film* was confirmed by the fact that there was a decline in its contact angle as a function of surface tension and that the water contact angle was on average 152° (Figure 3-8B). No sliding of rapeseed oil, hexadecane or octane occurred on this film. A liquid drop and rough surface are separated by a layer of air, which creates a superhydrophobic surface.^{88,89} However, if the surface tension of a liquid is low, the liquid will not be trapped in the relief and porous structure, thus posing an obstacle to the formation of an air layer. This explains why rapeseed oil, hexadecane and octane did not slide on the superhydrophobic film but rather became attached to it.

With a 1.23 refractive index (Figure 3-3), the superhydrophobic film possessed higher maximum transmittance compared to the superhydrophilic and anti-reflective film (Figure 3-6). However, greater surface roughness increased the light scattering, which is the reason why the superhydrophobic and ten-bilayer superhydrophilic and anti-reflective films had closely similar overall optical values of visible light (Figure 3-9).¹¹⁷ Further support for this was derived from the fact that the superhydrophobic film had lower parallel transmission (94.8%) but higher scattering (2.05%) than the superhydrophilic and anti-reflective film.

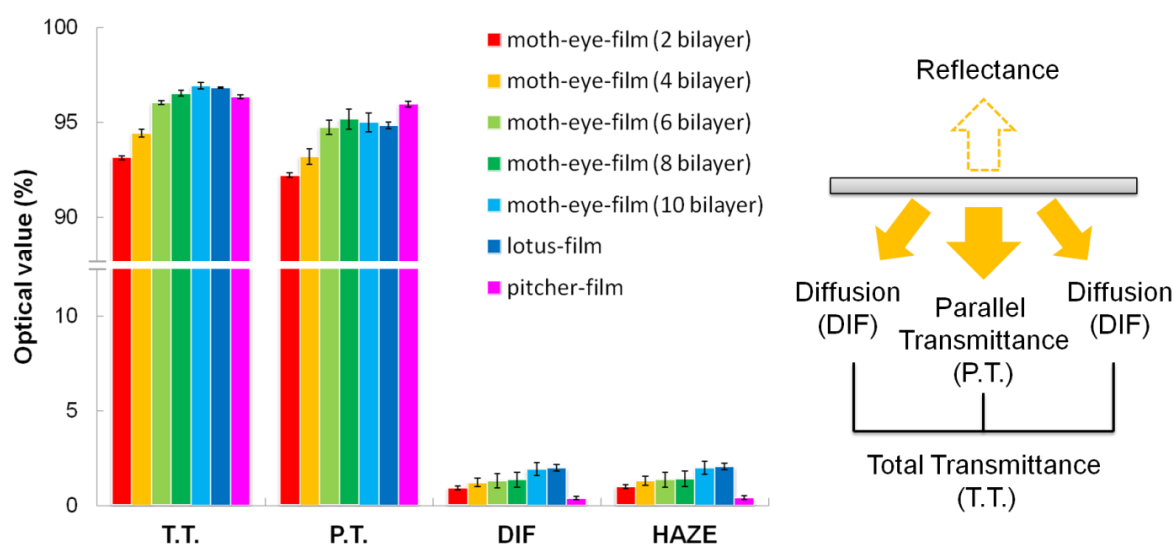


Figure 3-9. Superhydrophilic and anti-reflective films with two (red bar), four (yellow bar), six (lime green bar), eight (green bar) and ten bilayers (aqua bar), superhydrophobic film (blue bar) and slippery fluid-infused film (pink bar) are shown with their total transmittance (T.T.), parallel transmittance (P.T.), diffusion (DIF) and haze (HAZE). Explanations for the optical values are provided on the right-hand side. DIF divided by T.T. gives the haze, which indicates how much light diffusion is caused by light passing through the films. Reproduced with permission from Ref [106]. Copyright 2014 American Chemical Society.¹⁰⁶

3.3.3 Slippery fluid-infused film with antireflectivity

PFPE lubricant oil dropped on superhydrophobic film enabled creation of slippery fluid-infused anti-reflective film or *pitcher film*, which exhibited a decline in its contact and sliding angles as a function of surface tension. As shown in Figure 3-8C, the water and oil sliding angles were 10° and 2-5°, respectively.

The slipper fluid-infused anti-reflective film achieved the maximum transmittance of 97.2% at 798 nm (Figure 3-6), while its haze was not as high as that of other films at 0.41% (Figure 3-9). The formula below enables calculation of haze:

$$HAZE = (DIF/T.T.) \times 100 \quad (3-9)$$

The optical value of haze is denoted by *HAZE*, the optical value of diffusion is denoted by *DIF* and the optical value of total transmittance is denoted by *T.T.* The slippery fluid-infused anti-reflective film exhibited higher parallel transmittance and lower diffusion, even though its T.T. was comparable to that of the other films. This signifies that lubricant oil coating determined a reduction in surface topography-induced light diffusion and in the refractive index gap at the interface between solid and gas. Nevertheless, compared to the other films, this film had higher reflectance because the lubricant oil density was inconstant. Furthermore, the results refute that the film constituents were the catalyst of the scattering, indicating that, compared to the visible wavelength, CHINFs and nanoparticles were small enough to generate maximum 0.41% dispersal.

3.3.4 Anti-frosting properties

A glass substrate, ten-bilayer superhydrophilic film, superhydrophobic film and slippery fluid-infused film were assessed in terms of their anti-frosting capabilities (Figure 3-10). All three films exhibited antireflection prior to activation of the Peltier cooling unit. Five minutes following activation, there was slight misting on the superhydrophobic film due to

small nuclear fog adhering to it. Fog spread to the film-less glass substrate areas after ten minutes, leading to temperature being distributed heterogeneously in the same plane. Unlike the glass substrate, the fog was resisted to some extent by the superhydrophobic film,¹¹⁸ but after a quarter of an hour, frosting completely covered both of them. On the other hand, aside for the film-less substrate areas, neither the superhydrophobic nor the slippery fluid-infused film frosted, engendering a temperature difference among the superior and inferior parts. Although these two latter films also underwent progressive frosting in the 15-50 minute interval, they performed better than the glass substrate and the superhydrophilic film. The superhydrophobic film contained fog in its rough surface and therefore exhibited faster temperature reduction compared to the slippery fluid-infused film, which did not retain fog. With the rise in Peltier unit temperature, the relief structure of the superhydrophobic film kept water droplets, whereas the slippery fluid-infused film did not. Moreover, as indicated by thermography, the lubricant oil on the latter film retarded temperature alteration more than in the other films. However, none of the film lost their antireflection during this evaluation process.

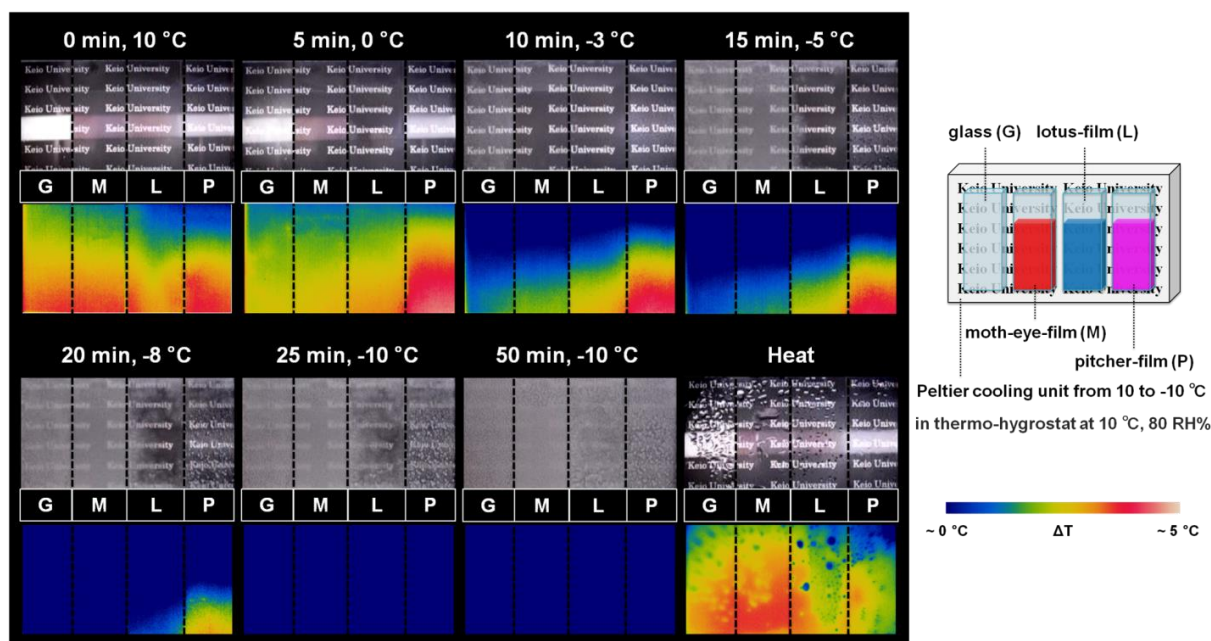


Figure 3-10. Glass substrate (G), ten-bilayer superhydrophilic film (M), superhydrophobic film (L), and slippery fluid-infused film (P) imaged photographically and *via* thermography. The time and temperature since activation of the Peltier cooling unit are indicated above the images. The Peltier unit dictated the temperature. As indicated on the right-hand side, the experiment involved introducing the films in a thermo-hygrostat at 10°C and 80% relative humidity, with a gradual decline in temperature until -10°C. Upon reaching that level, the temperature was increased to 30°C. Reproduced with permission from Ref [106]. Copyright 2014 American Chemical Society.¹⁰⁶

As the dew slid off it, the surface of the slippery fluid-infused film maintained a relatively small rise in temperature. Frost began to develop when the lubricant oil temperature dropped to a point that interfered with fluid surface maintenance. Subsequently frosting covered every surface. On the other hand, rise in Peltier unit temperature caused the water droplets with high specific temperature to slide off, determining a rapid increase in surface temperature.

The findings obtained suggest that slippery fluid-infused film is capable of preventing surface fogging as well as temperature alterations triggered by inadequate lubricant heat transfer, thereby demonstrating anti-frosting property.

3.4 Conclusions

The composition of nanofibres and nanoparticles made LbL assembly-based superhydrophobic films with antireflection highly porous, which is why they achieved 96.7% maximum transmittance and minimal refractive index of 1.20. To afford these films greater hydrophobicity, adjustments were made, resulting in achievement of the maximum transmittance of 97.5%, the minimal refractive index of 1.23 capable of supplying null reflectance, and 152° water contact angle. Meanwhile, the slippery fluid-infused film with antireflection obtained when lubricant was dropped on the superhydrophobic film had higher maximum transmittance (97.5%),^{22–25,102} owing to the fact that progressive modification of the refractive index had a diminishing effect on relief structure dispersal and anti-reflective behaviour. Moreover, by comparison to visible light wavelengths, the film CHINFs and nanoparticles were small enough and no haze value exceeded 2.05%. The liquid-infused surface transmittance was enhanced due to the use as lubricant underlayer of a film with poor reflectance. Another observation is that films impregnated with lubricant can hinder fog attachment and can withstand temperature alterations, thus preventing fog from forming. From a technological perspective, the integration of three biomimetic strategies made the present study possible and has the potential to promote material innovation, thus prompting the development of materials of high functionality.

Chapter 4

SLIPS Enhanced Through Wettability

4.1 Background

Owing to its minimal invasiveness, endoscopy has become a widely employed surgical procedure in the last ten years.¹¹⁹ However, a major issue with this procedure is that the endoscope lens allowing the surgeon to see what he/she is doing is easily stained with blood, thus reducing visibility.¹²⁰ Consequently, the endoscope lens has to be cleaned of blood and other fluids repeatedly during surgery, increasing the risk of blood clot formation as well as trapping foreign material in the blood coagulating on the surface.¹²¹ This can prolong surgery duration, increase costs to the patient and to the hospital, and lead to further complications.

Anti-fouling surfaces are needed by other medical devices (e.g. stents) as well. Stents are mainly applied to treat coronary artery disease, being introduced and expanded within the affected blood vessels, where they press the atheromatosis on the vessel wall, thus enabling blood to flow again.¹²² Blood clots could be eliminated with drug-eluting stents,¹²³ but their effect only lasts for the duration of drug elution and are accompanied by increased likelihood of in-stent restenosis and atherosclerosis. Hence, an anti-fouling coating capable of preventing blood clotting, atherosclerosis, clot aggregation and restenosis needs to be developed urgently.

To resolve these limitations, this study try to apply SLIPS for medical devices. Functionalised SLIPS are compatible with a range of underlayers,^{72,124} as revealed by a number of studies,¹²⁵ but the majority contain fluorinated lubricant oils (e.g. perfluoropolyether). However, one study reported lack of biocompatibility between the fluorinated underlayer and

oil used in the composition of the fluorinated SLIPS that was developed.^{126,127} Hence, based on the experimental approach outlined in Figure 4-1, this study sought to create a non-fluorinated SLIPS with materials demonstrating biodegradability and biocompatibility. The techniques of LbL self-assembly based on electrostatic interactions and hydrogen-bonding were applied to create the underlayer from chitosan, sodium alginate and polyvinylpyrrolidone (PVPON).^{46,128} Taking advantage of the fact that the hydrogen bonds were susceptible to pH, the film based on chitosan and alginate cross-linking was introduced into an alkaline buffer solution to eliminate the PVPON and thus to make the structure porous. The film surface was subjected to methyl silanization with decyltrimethoxysilane (DTMS) before being coated in biocompatible almond oil employed as the primary raw material in various substances (e.g. surgical bone wax, cosmetic oil).¹²⁹ Clinical experience confirmed the safety of sweet almond oil.¹³⁰ DTMS does not pose any risks and its use alongside methyl groups in triggering hydrophobicity should affect the human body less than fluorine elements, which lack biodegradability, are expensive, undergo reaction with different materials, and retard nerve development in children exposed to them.¹³¹ Furthermore, the surface energy associated with the shift from fluorinated to non-fluorinated oil confirmed that non-fluorinated almond oil was viable for use to adhere to the SLIPS porous underlayer. Additionally, an analysis was conducted to evaluate whether the biodegradable and biocompatible SLIPS demonstrating stability under physiological conditions was applicable to medical devices (e.g. endoscopes, stents). This assessment was undertaken on the basis of the optical properties, thickness and liquid repellent ability of thin films as well as the amount of time needed by blood to coagulate.

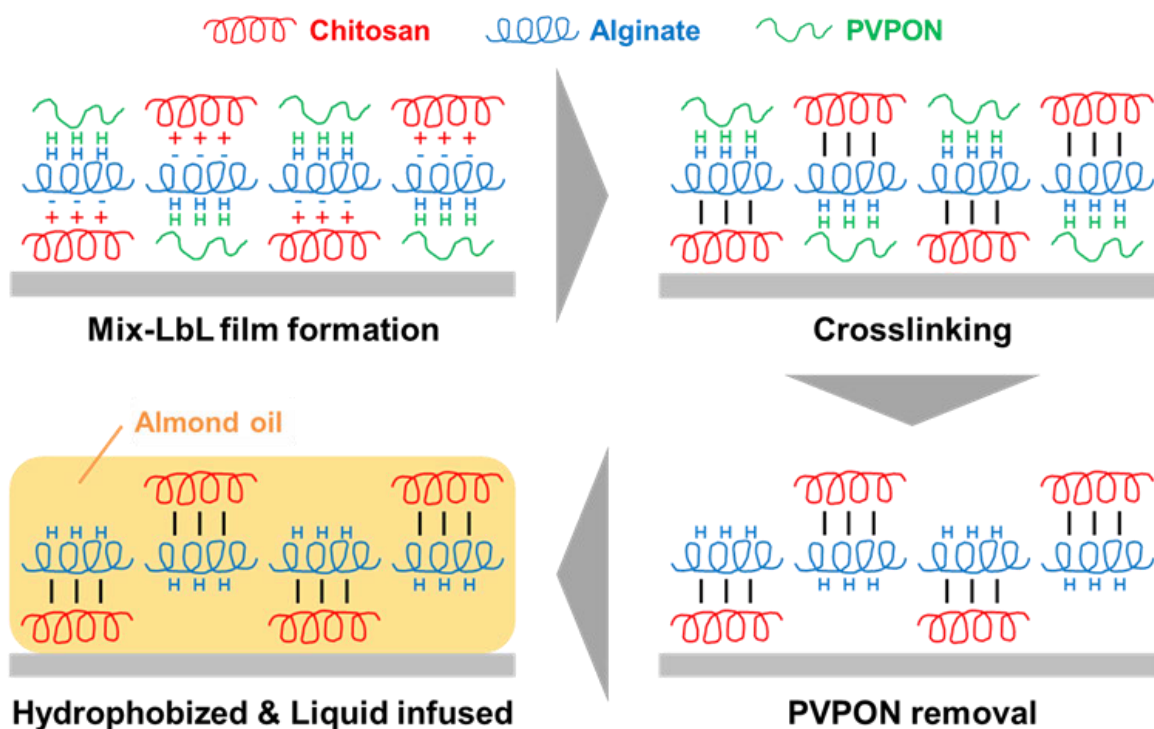


Figure 4-1. Simplified representation of how non-fluorinated SLIPS with biodegradability and biocompatibility is created. Reproduced with permission from Ref [132]. Copyright 2015 American Chemical Society.¹³²

4.2 Experiment

4.2.1 Materials

The creation of the films was achieved with chitosan (chitosan-10, Wako Pure Chemical Industries, Ltd., Osaka, Japan), sodium alginate (Nacalai Tesque, Inc., Kyoto, Japan), PVPON (MW ~55 kDa, Sigma-Aldrich, St. Louis, MO, USA), 1-ethyl-3-(3-dimethylaminopropyl) carbodiimide (EDC) (Wako Pure Chemical Industries, Ltd., Osaka, Japan), ethanol (EtOH) (Kanto Chemical Co., Inc., Tokyo, Japan), HCl (Kanto Chemical Co., Inc., Tokyo, Japan), decyltrimethoxysilane (DTMS) (Shin-Etsu Chemical Co., Ltd., Tokyo,

Japan), sweet almond oil (Original Co., Ltd., Tokyo, Japan), and glass substrates (76×26 mm, thickness: 1.0 mm, refractive index: 1.52, Matsunami Glass Ind., Ltd., Kishiwada, Japan). Sodium carbonate, sodium bicarbonate (Wako Pure Chemical Industries, Ltd., Osaka, Japan), and ultra-pure water were used in the preparation of an alkaline 10 mM buffer solution. Acetic acid (Kanto Chemical Co., Inc., Tokyo, Japan), sodium acetate, and ultra-pure water (Aquarius GS-500.CPW, Advantec Co., Saijo, Japan) were used in the preparation of a 10 mM buffer solution with a pH of 4. The acetate buffer solution of pH 4 was employed in the preparation of every polyelectrolyte dipping solution. A solution of potassium hydroxide (1:120:60 wt.% of KOH:H₂O:ethanol) (Junsei Chemical Co., Ltd., Tokyo, Japan) was used to clean the glass substrates for 120 seconds, after which ultra-pure water was used to rinse them rigorously and get them ready for use.

4.2.2 Preparation of precursor film

A mix-LbL approach was adopted to prepare precursor films suitable for porous underlayer development by producing sodium alginate and alternating with a combination of polyelectrolyte (chitosan) and hydrogen-bonding polymer (PVPON). After immersion in the mix of chitosan and PVPON (1 mg/mL; vol.% of 25:75, 50:50, or 75:25) for ten minutes, the glass substrate was rinsed thrice in buffer solution for 180 seconds. This was followed by immersion of the substrate in a solution of sodium alginate (1 mg/mL) for ten minutes and rinsing in buffer solution. This dipping protocol was equivalent to a single bilayer deposition and was carried out until achievement of the target number of bilayers. Every solution employed in film development had a fixed pH of 4. An automatic LbL fabrication machine (Nano Film Maker, SNT Co., Kawasaki, Japan) facilitated film development. A light nitrogen gas stream was applied to dry the films following multilayer assembly.

4.2.3 Crosslinking

Amide bonds between chitosan and alginate were formed by crosslinking the twenty-bilayer precursor films consisting of chitosan, PVPON and alginate in an EDC solution (pH 5, 200 mM EDC in 50:50 vol.% EtOH:H₂O) for one day at a temperature of 4°C. Rinsing of the films was subsequently conducted twice for five minutes in a solution with a pH of 5 achieved through addition of hydrochloric acid.

4.2.4 Elimination of PVPON

Immersion of the crosslinked LbL films in buffer solution (pH 10, 10 mM Na₂CO₃/Na₂HCO₃ in 50:50 vol.% EtOH:H₂O) was conducted for 120 minutes, followed by rinsing two times in pure water for five minutes, to eliminate the hydrogen-bonding element (i.e. PVPON) from the films.

4.2.5 Hydrophobization and liquid infusion

The gas phase technique was employed to make the porous multilayer films (chitosan:PVPON, vol.% of 50:50) hydrophobic. This involved introducing them in a glass bottle with a volume of 100 mL and a glass bottle of 2 mL and with a content of 200 μ L DTMS. The whole system was then introduced in a thermal incubator for 150 minutes at 140°C. Addition of the almond oil (1 μ L cm⁻²) to the hydrophobized film was done in a drop-wise manner. Nitrogen gas was blown over the surface to eliminate any extra almond oil from the films.

4.2.6 Blood coagulation test

Digital microscopy (VHX-1000, Keyence, Osaka, Japan) enabled visualisation of how 3 μ L pig blood with 0.3 wt.% citric acid (Tokyo Shibaura Zouki Co., Tokyo, Japan) coagulated on glass, the porous chitosan/alginate film after PVPON was eliminated, the hydrophobized porous film, and biocompatible SLIPS. The blood coagulation time was established to be the point when the blood stopped flowing and changed colour due to clotting.

4.2.7 Characterization

According to a previous research, Fourier transform infrared spectroscopy (FT-IR) (ALPHA-T, Bruker, Billerica, MA, USA) was applied to analyse the chemical bonds in the films prior to and following crosslinking and elimination of PVPON on silicon substrates treated with plasma.¹³³ The film surface nanotopography was imaged with the FE-SEM (S-4700, Hitachi, Tokyo, Japan) with 3 kV accelerating voltage. Ellipsometry (MARY-102, Five Lab Co., Saitama, Japan) enabled measurement of the thickness and refractive index of thin films covered on the glass substrates. A spectrophotometer (UVmini-1240, Shimadzu, Kyoto, Japan) was used to determine the transmittance in the 300-1000 nm spectral range, while a contact-angle meter (CA-DT, Kyowa, Tokyo, Japan) was employed to obtain the contact angles and sliding angles for a 5 μ L droplet. A fully automatic surface tensiometer (CBVP-Z, Scientific Gear, Fairfax, VA, USA) allowed the surface tension to be measured. A haze meter (NDH-5000, Nippon Denshoku Industries, Co., Ltd., Tokyo, Japan) allowed measurement of the total transmittance and the optical source employed was a diode (5 V, 3 W) with white light emission. T.T. and P.T. divided by DIF gave the HAZE, indicating how much light was dispersed when the light passed through the films.

4.3 Results and Discussion

4.3.1 Biodegradable porous underlayer for SLIPS

Both the amide I and amide II bands increased to 1590 cm^{-1} and 1530 cm^{-1} following EDC treatment, as revealed by the FT-IR analyses undertaken on the film consisting of chitosan/PVPON and alginate pre- and post-EDC treatment (Figure 4-2). Hence, the chitosan amine groups and the alginate carboxylic groups were successfully crosslinked. Based on the FT-IR spectra of chitosan, PVPON and sodium alginate (Figure 4-3), the C-H stretching vibration of PVPON was identified as the source of peaks at approximately 1290 cm^{-1} , asymmetrical C-O-C gave the peaks at about 1060 cm^{-1} , symmetrical O-C-O gave the peaks at 1400 cm^{-1} , and asymmetrical O-C-O stretching vibration of chitosan and sodium alginate gave the peaks at 1590 cm^{-1} . The rise in pH caused hydrogen bonds between PVPON and alginate to be lost, resulting in a minor decline in the 1290 cm^{-1} peak of PVPON following crosslinking in EDC solution at a pH of 5.

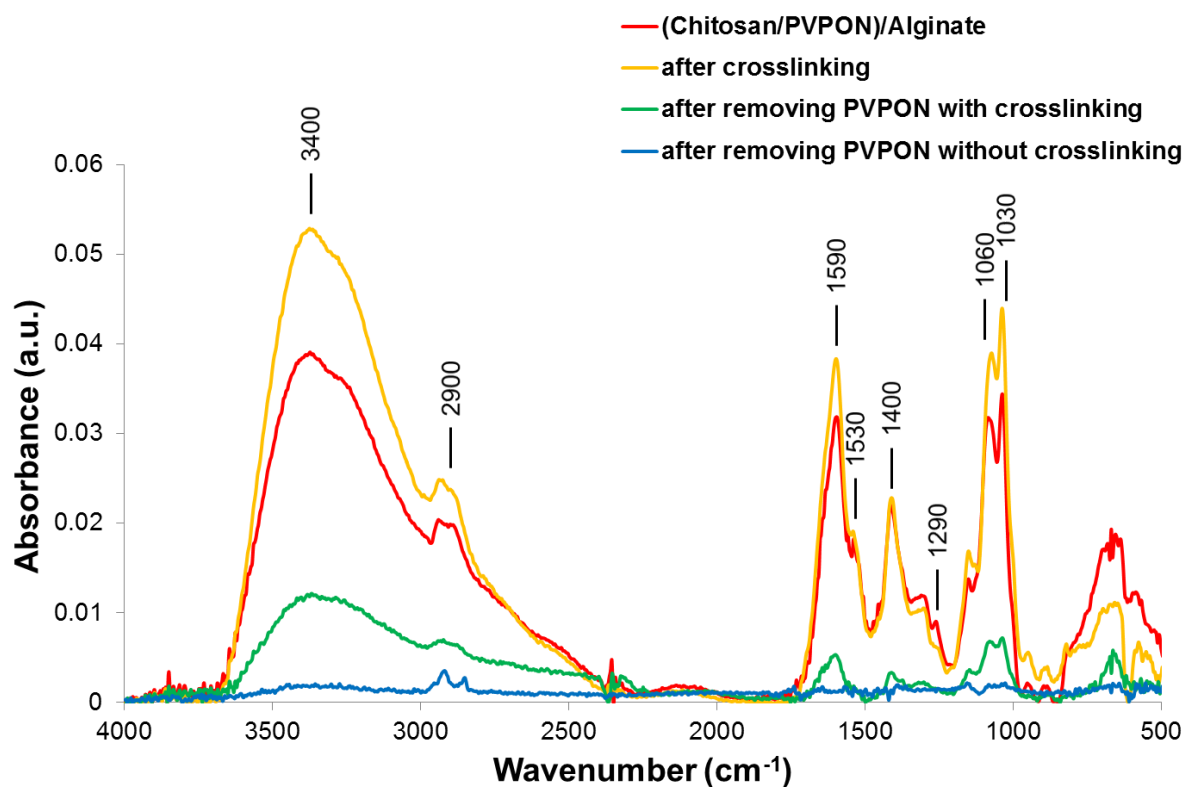


Figure 4-2. The red, orange, green and blue lines respectively represent the FT-IR spectra of the precursor film of chitosan/PVPON and alginate, a film after crosslinking, a film with porosity following removal of PVPON from the crosslinked film, and a film following PVPON removal from a film without crosslinking. Reproduced with permission from Ref [132].

Copyright 2015 American Chemical Society.¹³²

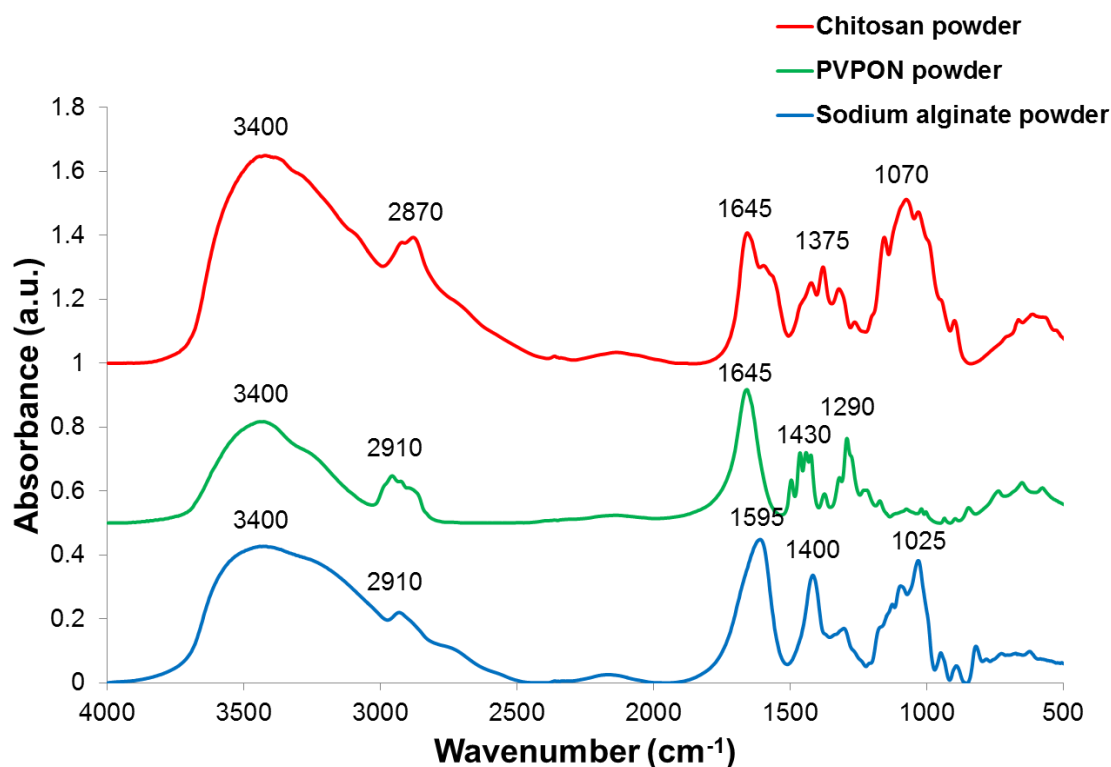


Figure 4-3. FT-IR spectra of the chitosan/PVPON/alginate film constituents, namely, chitosan, PVPON and sodium alginate powders. Reproduced with permission from Ref [132]. Copyright 2015 American Chemical Society.¹³²

After dipping in buffer solution with pH 10, the IR peaks of films with and without crosslinking were measured to ensure film stability and that PVPON was eliminated from the crosslinked film. The 1290 cm⁻¹ peak of PVPON vanished when the pH of the crosslinked film was elevated, but some important peaks related to the stretching vibration of amide bands, chitosan and alginate were preserved. On the other hand, all peaks vanished when PVPON was eliminated from the film without crosslinking, suggesting the necessity of film crosslinking and its importance for ensuring film stability against modifications in pH. Furthermore, to corroborate the FT-IR results and demonstrate that the films existed after PVPON was eliminated, XPS analysis was carried out by dipping the films into a buffer solution with pH 10 (Figure 4-4).

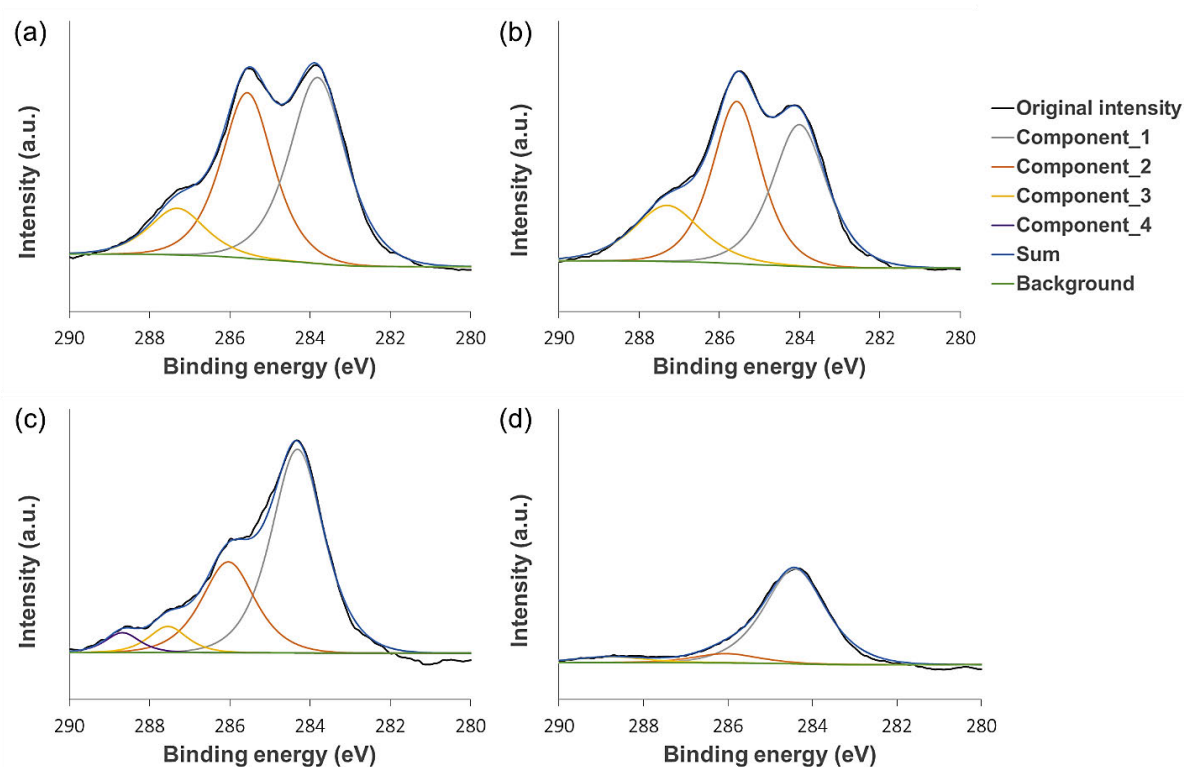


Figure 4-4. C_{1s} core level spectra associated with the precursor film containing chitosan/PVPON and alginate (a); film with crosslinking (b); film with porosity following elimination of PVPON from the crosslinked film (c); and film following PVPON elimination from a film without cross-linking (d). The C-C peak is denoted by component_1, the C-O peak is denoted by component_2, the N-C=O peak is denoted by component_3 and the O=C-O peak is denoted by component_4. Reproduced with permission from Ref [132]. Copyright 2015 American Chemical Society.¹³²

Multilayers comprising biomacromolecules of similar structure are usually flat, without any topography or aggregation, which is why the precursor film of chitosan/PVPON/alginate and the crosslinked film had an almost flat structure (Figure 4-5). An orderly nanotopography and porosity were generated when PVPON was eliminated (Figures 4-6 and 4-7). Furthermore, regular film nanopores can also develop due to elimination of PVPON,⁴⁸ owing to film creation

based on the self-assembly of a polymer mixed solution of PVPON and chitosan and an alginate solution, which produce structures of stable energy when combined.⁹³

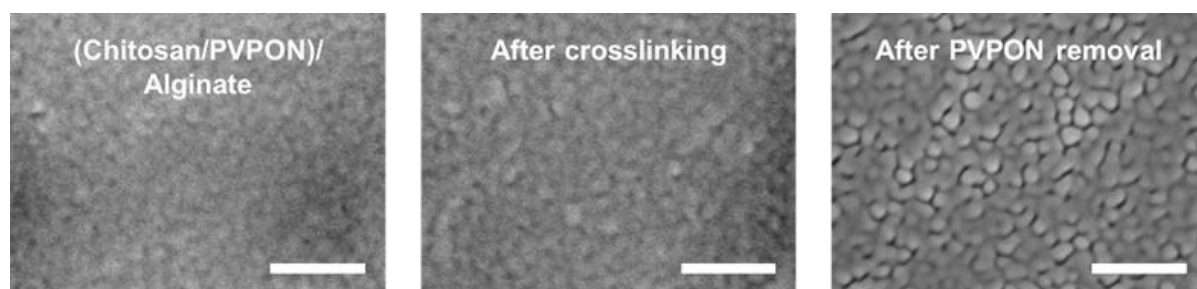


Figure 4-5. FE-SEM imaging at a scale bar of 300 nm of precursor film containing chitosan/PVPON and alginate (left), film with crosslinking (centre), and film with porosity following elimination of PVPON from the crosslinked film (right). Reproduced with permission from Ref [132]. Copyright 2015 American Chemical Society.¹³²

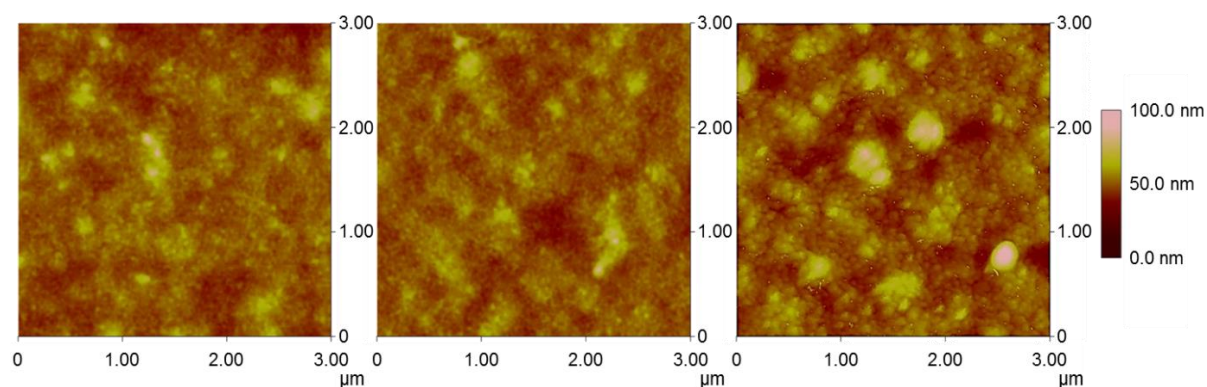


Figure 4-6. AFM images showing the precursor film containing chitosan/PVPON and alginate (left), film with crosslinking (centre), and film with porosity following elimination of PVPON from the crosslinked film (right). The scan size (x and y) and data scale (z) are respectively 3 μm and 100 nm. Reproduced with permission from Ref [132]. Copyright 2015 American Chemical Society.¹³²

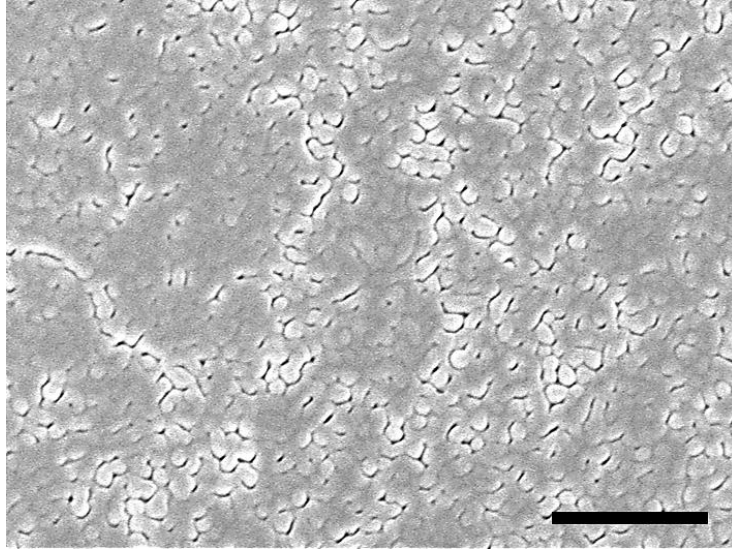


Figure 4-7. Low magnification FEM-SEM imaging at 500 nm scale bar of a film demonstrating porosity following elimination of PVPON from the crosslinked film. Reproduced with permission from Ref [132]. Copyright 2015 American Chemical Society.¹³²

The enhancing effect on porosity that elimination of PVPON had was confirmed by ellipsometry analysis (Figure 4-8). The following straightforward mixing rule was applied to determine the LbL film refractive index, based on the Fresnel equations:¹¹⁰

$$n_l = f_{air}n_{air} + f_{polyelectrolyte1}n_{polyelectrolyte1} + f_{polyelectrolyte2}n_{polyelectrolyte2} \quad (4-1)$$

The volume fraction and component x refractive index are respectively indicated by f_x and n_x . The equation implies that an LbL film becomes more porous as its refractive index declines. In fact, the level of PVPON in the chitosan/PVPON mixed solution was observed to dictate by how much the refractive index declined following PVPON elimination. Moreover, voids took the place of the physical space where PVPON had been when the film was immersed in buffer solution with pH 10, which increased the PVPON content ratio and consequently led to additional reduction in the refractive index.

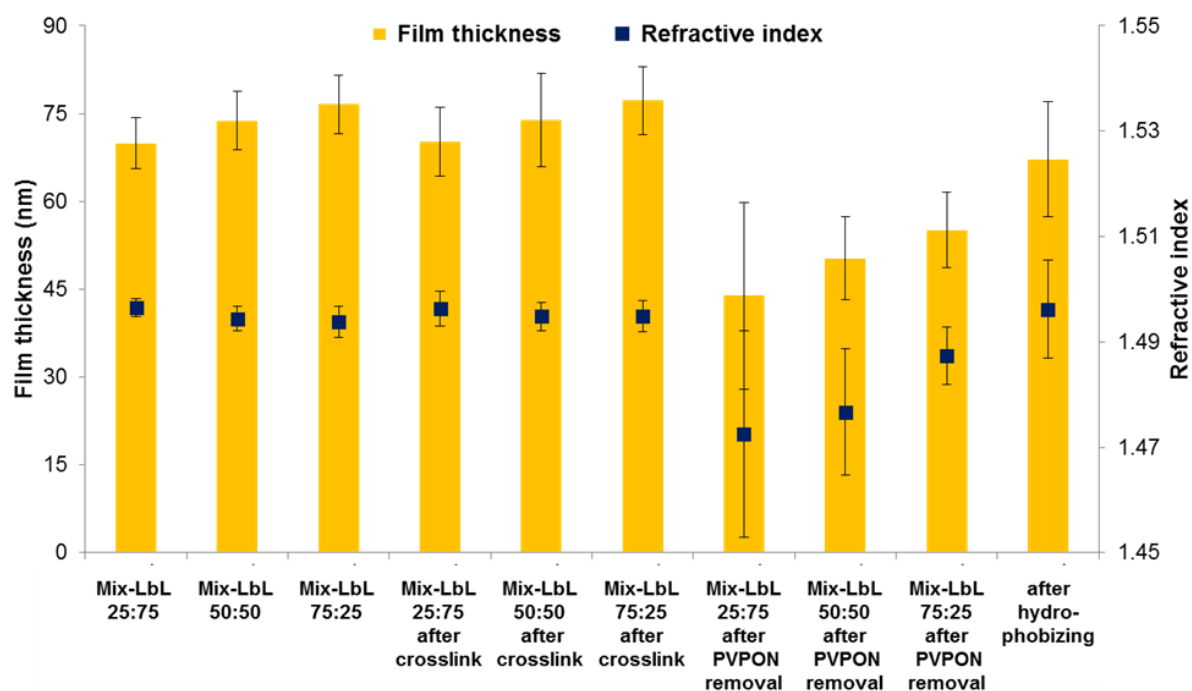


Figure 4-8. Ellipsometry analysis showing the thickness and refractive index, represented by yellow bars and blue squares, respectively, of the precursor films of chitosan/PVPON and alginate comprising varying mixture fractions (chitosan: PVPON vol.% of 25:75, 50:50, and 75:25), which are denoted by mix-LbL X: Y, crosslinked films, films with porosity following elimination of PVPON from the crosslinked films, and hydrophobized films with porosity (chitosan: PVPON, vol.% of 50:50). Reproduced with permission from Ref [132]. Copyright 2015 American Chemical Society.¹³²

The PVPON content ratio determined how thick the films were as well. Since the strength of the electrostatic interactions between chitosan and alginate exceeded that of PVPON-alginate hydrogen-bonding, making the former conducive to film growth, the films became thicker with the reduction in the mixture solution PVPON ratio equivalent to a rise in chitosan ratio (Figure 4-9). However, the films became thinner when PVPON was eliminated from the crosslinked films in buffer solution of pH 10, as this caused shrinking of the multilayers. Meanwhile, partial detachment of the film from the glass substrate occurred when

the film with the mixture fraction chitosan: PVPON vol.% of 50:50 was immersed. Hence, the subsequent experiments were conducted with the precursor film containing chitosan/PVPON/alginate with a mixture fraction of chitosan: PVPON vol.% of 50:50.

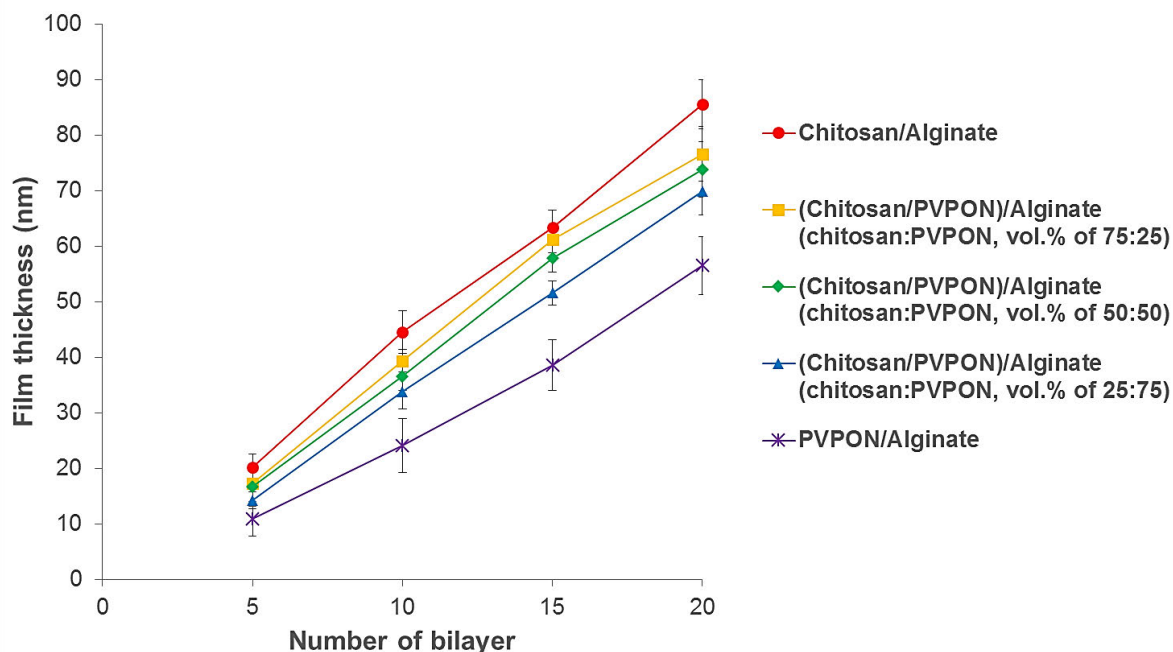


Figure 4-9. Growth of films consisting of chitosan/alginate, PVPON/alginate, and chitosan/PVPON/alginate in varying mixture fractions (chitosan: PVPON vol.% of 25:75, 50:50, and 75:25). Reproduced with permission from Ref [132]. Copyright 2015 American Chemical Society.¹³²

After they were hydrophobized for 150 minutes at a temperature of 140°C, the films became thicker and had a higher refractive index. The procedure caused small quantities of moisture from the multilayer to evaporate, in turn causing the films to swell up.¹⁰⁶ However, exposure to heat reduced the swelling of multilayer LbL films with polymers soluble in water due to the fact that the polymer substrate lacked permeability.

Figure 4-10 illustrates how the films' light transmittance changed. The refractive index between the glass substrate and air differed less because the films were present¹⁰⁶ and the films composed of chitosan/PVPON and alginate exhibited higher transmittance compared to the glass substrate. After the films were crosslinked, transmittance was preserved, but PVPON elimination diminished the transmittance of the film with porosity, due to the fact that, as revealed by FE-SEM imaging, film porosity and nanotopography intensified light dispersal. The hydrophobized films with porosity exhibited a higher refractive index and scattering structure compared to pre-hydrophobization porous film, which is why their transmittance was lowest. An increase in transmittance due to heightened parallel transmittance and reduced diffusion was achieved after almond oil was dropped on the hydrophobized films with porosity, creating SLIPS that demonstrated biodegradability and biocompatibility (Figure 4-11). What this implies is that the addition of almond oil caused a reduction in surface topography-induced light dispersal as well as in the refractive index at the interface between solid and air.

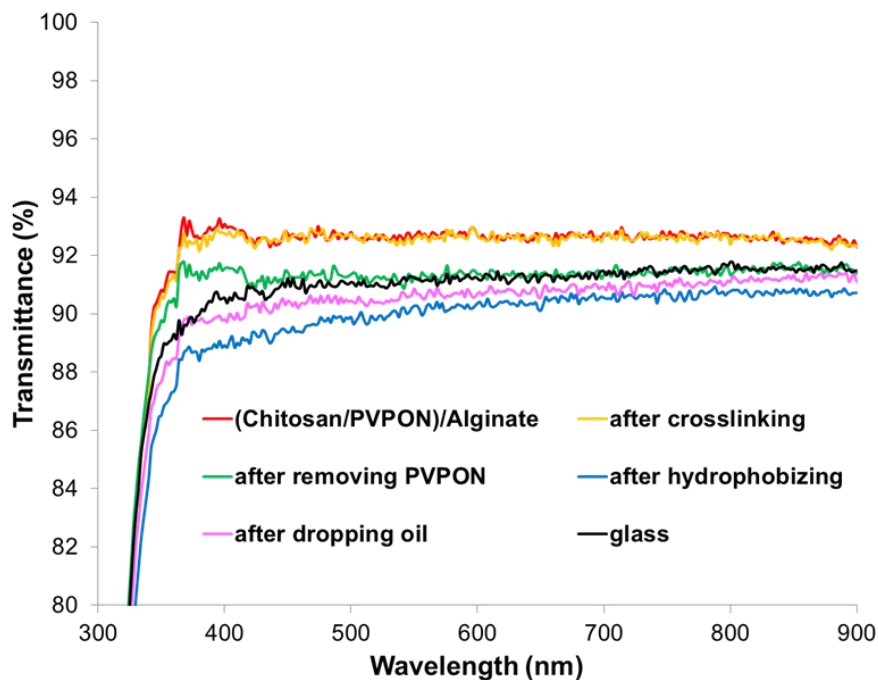


Figure 4-10. Film transmittance variations: The black, red, yellow, green, blue, and pink lines are respectively indicative of the transmittance of a glass substrate, a precursor film comprising chitosan/PVPON and alginate (chitosan:PVPON vol.% of 50:50), a film with crosslinking, a film with porosity following PVPON elimination from the crosslinked film, a hydrophobized film with porosity, and a SLIPS with biocompatibility after oil was dropped on the hydrophobized film with porosity on glass substrates in an air medium. Reproduced with permission from Ref [132]. Copyright 2015 American Chemical Society.¹³²

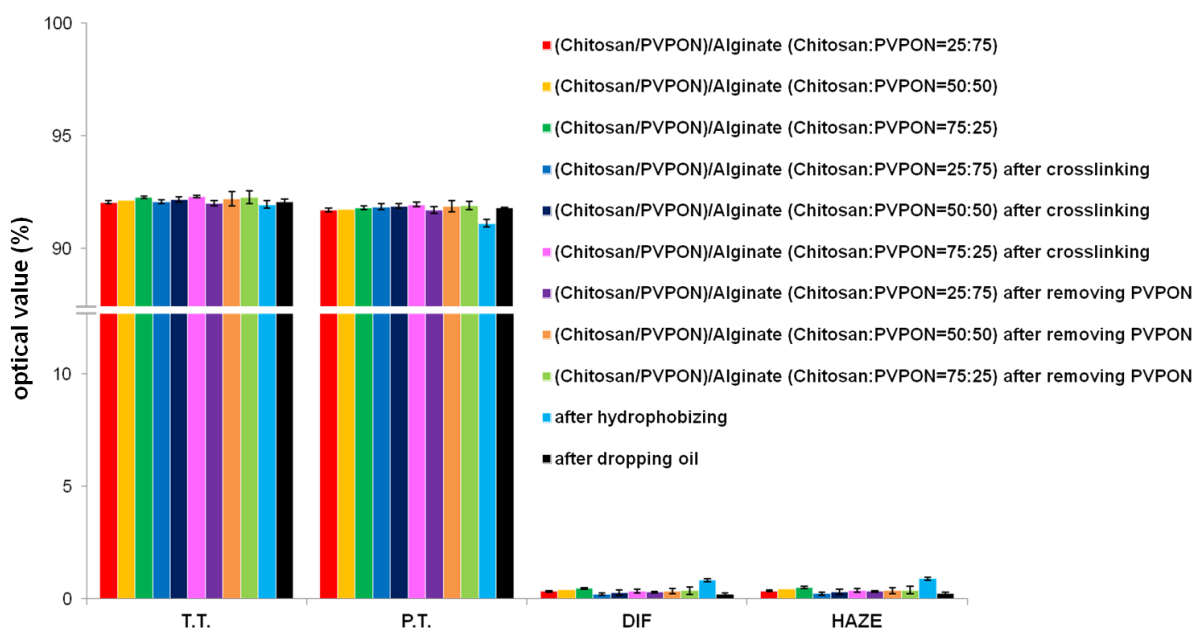


Figure 4-11. Total transmittance (T.T.), parallel transmittance (P.T.), diffusion (DIF) and haze (HAZE) associated with precursor film comprising chitosan/PVPON and alginate (chitosan: PVPON vol.% of 25:75, red bars; 50:50, yellow bars; 75:25, green bars), films with crosslinking (chitosan: PVPON vol.% of 25:75, blue bars; 50:50, dark blue bars; 75:25, pink bars), films with porosity following PVPON elimination from the crosslinked films (chitosan: PVPON vol.% of 25:75, purple bars; 50:50, orange bars; 75:25, lime green bars), a hydrophobized film with porosity (chitosan: PVPON vol.% of 50:50, light blue bars), and a

SLIPS with biocompatibility after oil was dropped on the hydrophobized film with porosity (black bars). Reproduced with permission from Ref [132]. Copyright 2015 American Chemical Society.¹³²

4.3.2 SLIPS applied criteria

The hydrophilicity of the surface was converted into hydrophobicity as a result of hydrophobization (Figure 4-12). Prior to this process, the hydrophilic nature of the films and water-soluble polymer absorption had reduced the contact angles to almost zero (Figure 4-13). To ascertain whether the hydrophobized films with porosity satisfied the SLIPS criteria below, measurements of the contact angles of water and almond oil on the films with hydrophobicity were performed:²²

$$\Delta E_1 = \gamma_{oa} \cos \theta_o - \gamma_{wa} \cos \theta_w - \gamma_{wo} > 0 \quad (4-2)$$

$$\Delta E_2 = \gamma_{oa} \cos \theta_o - \gamma_{wa} \cos \theta_w + \gamma_{wa} - \gamma_{oa} > 0 \quad (4-3)$$

The interfacial tension between the two phases defined by the subscripts w (water), o (almond oil), and a (air) is denoted by γ_{xy} , while the contact angles of almond oil and water on the multilayer with hydrophobicity on an air background are respectively denoted by θ_o and θ_w . Fowkes equation was applied to determine γ_{wo} :²²

$$\gamma_{wo} = \gamma_{oa} + \gamma_{wa} - 2(\gamma_{oa}^\alpha \gamma_{wa}^\alpha)^{\frac{1}{2}} \quad (4-4)$$

The contributions made by the liquid surface tensions to the dispersion force are denoted by γ_{oa}^α and γ_{wa}^α . The surface tension contributed 21.8 mN/m to the dispersion force. In the case of materials without polarity, $\gamma_{oa}^\alpha \approx \gamma_{oa}$.¹³⁴

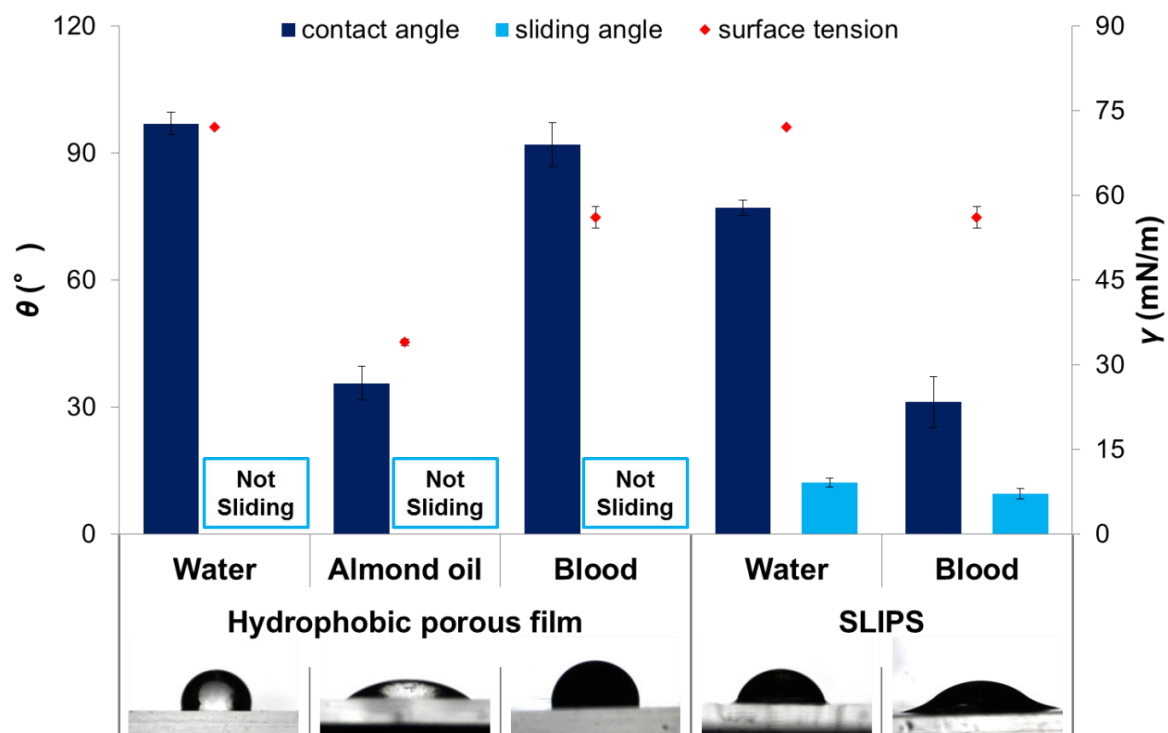


Figure 4-12. The dark blue bars, light blue bars and red diamonds respectively represent the contact angle, sliding angle and surface tension of water, almond oil, and blood on hydrophobized film with porosity and SLIPS with biocompatibility created when almond oil was dropped on the hydrophobized film with porosity. Equivalent pictures of every liquid drop on each film are provided below. Reproduced with permission from Ref [132]. Copyright 2015 American Chemical Society.¹³²

The blood coagulation time and the contact area could not be precisely correlated, despite the fact that each contact angle gave a different contact area between blood and each surface, and in particular, the contact area between blood and the SLIPS with biocompatibility was more expansive compared to the hydrophobized surface demonstrating porosity.

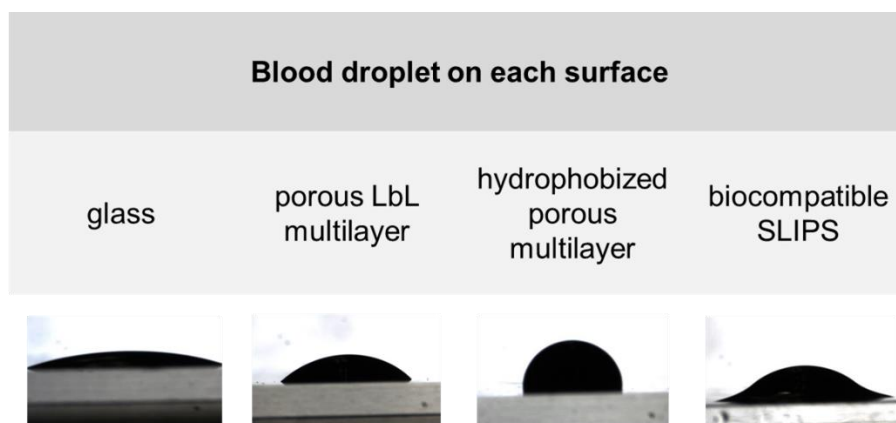


Figure 4-13. Blood droplet on every surface, as imaged with the CCD camera. Reproduced with permission from Ref [132]. Copyright 2015 American Chemical Society.¹³²

Due to the fact that they did not exhibit microtopography but only nanotopography, the films were not made superhydrophobic by the process of hydrophobization. The SLIPS criteria were satisfied by the hydrophobic surface with porosity, which presented a stable liquid surface (Table 4-1), confirming that the film was a SLIPS with an underlayer demonstrating biodegradability and porosity and produced from a non-fluorinated fluid possessing biocompatibility.

Table 4-1. The measurements obtained for the contact angles and surface tensions of water and almond oil as well as the interfacial tension and spreading coefficient among water and almond oil. Reproduced with permission from Ref [132]. Copyright 2015 American Chemical Society.¹³²

water			almond oil			γ_{wo} (mN/m)	ΔE_1	ΔE_2	$S_{ow(a)}$
γ_{wa} (mN/m)	θ_w (°)	γ_{wa}^α (mN/m)	γ_{oa} (mN/m)	θ_o (°)	γ_{oa}^α (mN/m)				
72.1	97	21.8	34	35.7	34	51.7	1.71	91.5	-13.6

The SLIPS with biodegradability and biocompatibility displayed a low sliding angle of water of around 10°, despite the fact that no sliding of the droplet of water on the hydrophobic multilayer occurred.

The spreading coefficient dictates the coating criterion:²⁶

$$S_{ow(a)} = \gamma_{wa} - \gamma_{wo} - \gamma_{oa} \quad (4-5)$$

The lubricant fluid would coat the water droplet and lubricant loss due to evaporation would occur if $S_{ow(a)} > 0$, but the lubricant fluid would not coat the water droplet and no loss of lubricant due to evaporation would occur if $S_{ow(a)} < 0$. The stability of the lubricant fluid coating the porous multilayer in the case of the SLIPS with biodegradability and biocompatibility was confirmed by $S_{ow(a)} = -13.6$ (Table 4-1). In fact, as shown in Figure 4-14, the SLIPS with biodegradability and biocompatibility still functioned as a SLIPS with a sliding angle of water lower than 25° and total transmittance exceeding 85% following exposure for up to one month at room temperature. A single day of exposure determined a minor increase in the sliding angle and a minor reduction in transmittance, but additional exposure did not significantly alter the two properties. This implied that a day of exposure caused almond oil to evaporate only to a small extent and the stability of the lubricant layer was maintained.

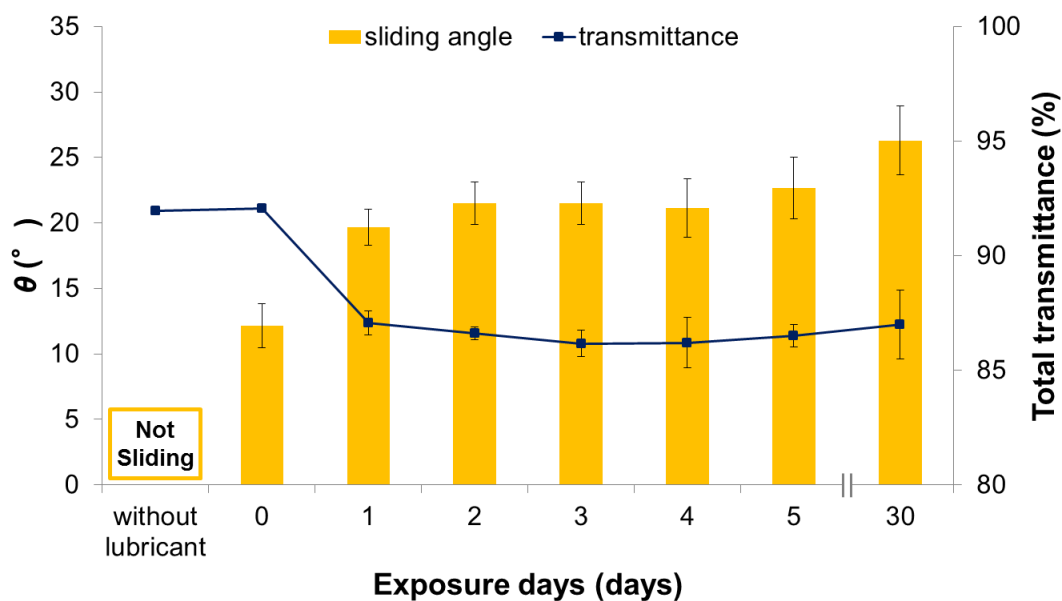


Figure 4-14. The yellow bars and blue squares respectively show how the sliding angle of water and the total transmittance of a SLIPS with biocompatibility changed following growing exposure at room temperature. A haze meter was employed to determine the total transmittance, representing the parallel transmittance coupled with forward diffusion. Reproduced with permission from Ref [132]. Copyright 2015 American Chemical Society.¹³²

4.3.3 Durability

High shear was applied to SLIPS with biocompatibility to test how robust it was and a spin coater of varying spinning speeds enabled comparison between the sliding angle of water and blood (Figure 4-15).²⁴ The SLIPS continued to be repellent following the shear test in the range of 250-6000 rpm. Furthermore, measurements of the sliding angle of water and blood were performed following exposure under running water for various water flowing durations in order to evaluate how stable the biocompatible SLIPS was in fluid (Figure 4-16). The film remained repellent for a period of four hours of exposure. Nevertheless, the sliding angle of water and blood still rose, and the two liquids only slid off after nine and eleven hours, respectively.

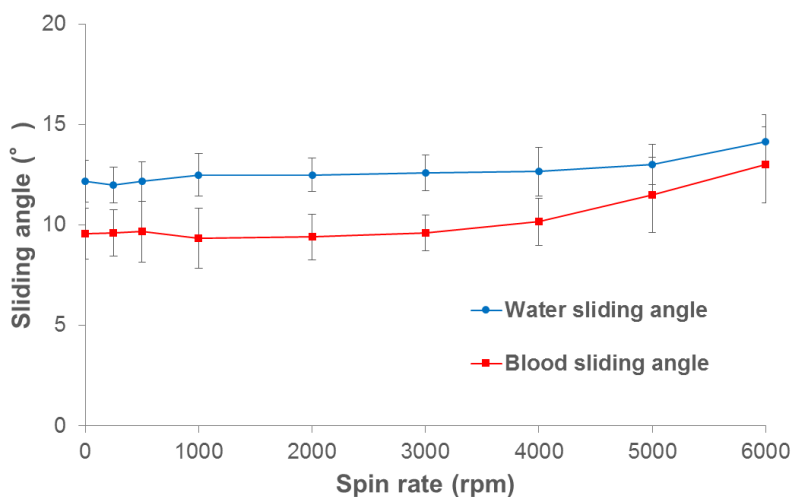


Figure 4-15. The sliding angle of water and blood, shown in blue and red, respectively, on the SLIPS with biocompatibility following 60 seconds of spinning at spin rates in the range 250-6000 rpm. Reproduced with permission from Ref [132]. Copyright 2015 American Chemical Society.¹³²

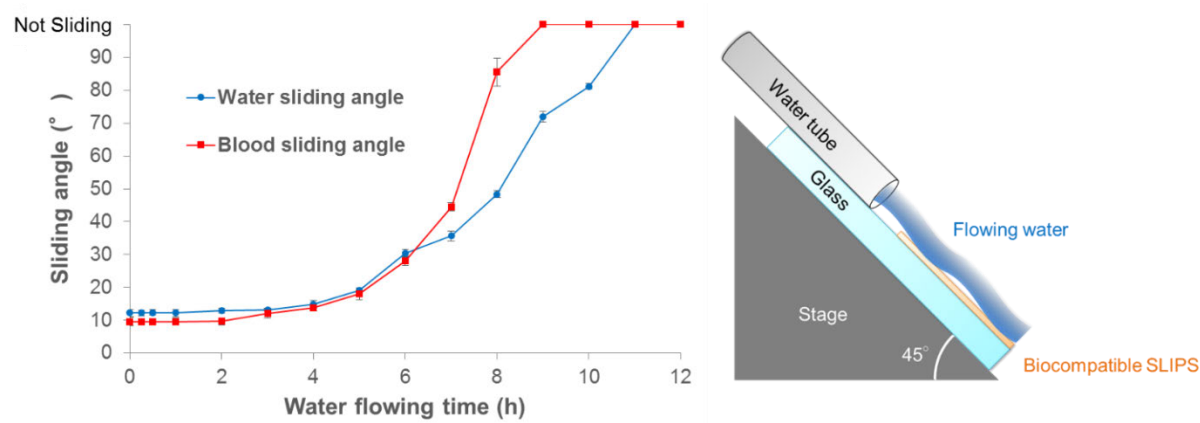


Figure 4-16. The sliding angle of water and blood, shown in blue and red, respectively, on the SLIPS with biocompatibility following exposure under running water for a water flowing duration in the range 0.25-12 hours. The flow rate from a peristaltic pump (MP-1000, Tokyo Rikakikai Co., Ltd., Tokyo, Japan) was 0.32 ml/s through a water tube (inside diameter: 3.15 mm, outside diameter: 5.20 mm). Reproduced with permission from Ref [132]. Copyright 2015 American Chemical Society.¹³²

4.3.4 Antithrombogenic properties

A digital microscope was used to determine how long it took for blood to coagulate on each film (Figure 4-17). For this purpose, the reference employed was the glass substrate, on which the duration of blood coagulation was 12 minutes. On the pre-hydrophobization porous multilayer, blood coagulated in 8 minutes, due to the fact that chitosan and alginate possess properties of blood coagulation. On the other hand, on the post-hydrophobization porous multilayer and the SLIPS with biocompatibility, blood took longer to coagulate. A low surface energy was engendered by the DTMS applied to the hydrophobized film, and consequently blood could not bind to the chitosan and alginate. The anti-clotting capacity exhibited by the hydrophobized multilayer arose from the fact that proteins were not adsorbed, since adsorbed blood proteins serve as mediator of interactions between synthetic material surfaces and blood.^{93,135}

Owing to the low surface wettability and the anti-clotting capacity of almond oil, which consists primarily of oleic acid, a notable anti-thrombogenic effect was displayed by the biocompatible SLIPS. The film anticoagulation effect is promoted by oleic acid by attaching to lysine residues in the proximity of the antithrombin III N-terminus, which represents a physiological serine protease inhibitor in charge of regulating the coagulation reaction as a suppressor of blood coagulation as well as stimulating reactions with serine proteolytic enzymes.¹³⁶ Almond oil also contains linoleic acid, which is present in lipoprotein lipids and has anti-atherogenic properties. Linoleic acid-enhanced lipoproteins are more sensitive to oxidation, which adversely affects the activity of platelets, leading to reduced susceptibility to oxidative stress in lipoprotein particles enhanced with more oleic acid than with linoleic acid.¹³⁷

The use of lubricant fluid to coat the margin of the target fluid hindered the blood from evaporating at the interface between the blood and lubricant oil (Figure 4-12). Coagulation of blood on the biocompatible SLIPS occurred after half an hour, yet it was possible to repel and

eliminate the coagulated blood from the surface without difficulty and with no staining (Figure 4-18). Furthermore, measurements of the sliding angle of blood on the surface displaying hydrophobicity and the SLIPS with biocompatibility were performed (Figure 4-12). The surface tension of blood was to be not as high as that of water, with a difference of 15 mN/m. As indicated in an earlier research, lower surface tensions were accompanied by lower sliding angles on the SLIPS.^{102,106} This study observed that the heightened mobility of the lubricant layer facilitated repellence of blood from the biocompatible SLIPS by contrast to water.^{102,106} No blood staining or traces were left after the blood slid off the film (Figure 4-19). On the basis of these findings, it can be concluded that, by comparison to the bare glass, the LbL multilayer with porosity, and the hydrophobized multilayer with porosity, the SLIPS demonstrating biodegradability and biocompatibility showed stability under physiological conditions and was the most suitable cloaking film for application in a medical context.

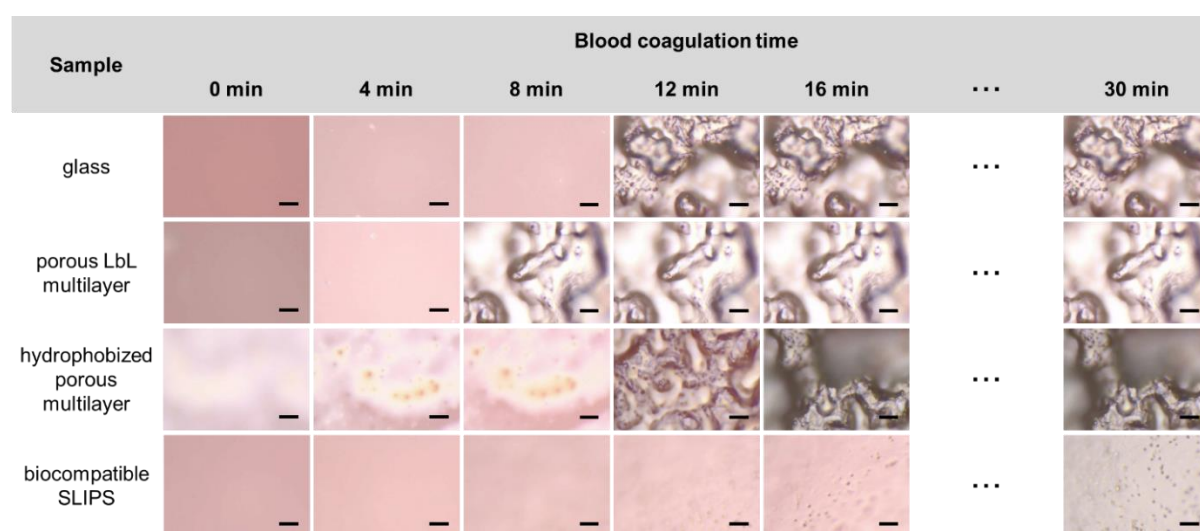


Figure 4-17. Digital microscopy imaging at a 10 μm scale bar showing how long it took for blood to coagulate on a glass substrate (first line), films with porosity following PVPON elimination from a crosslinked film (second line), a hydrophobized film with porosity (third line), and a biocompatible SLIPS after oil was dropped on the hydrophobized film with porosity

(fourth line). Reproduced with permission from Ref [132]. Copyright 2015 American Chemical Society.¹³²

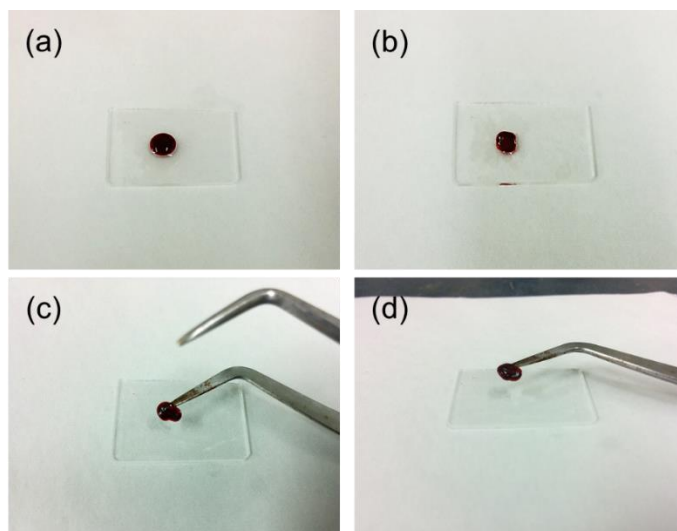


Figure 4-18. Pictures showing a droplet of blood on a SLIPS with biocompatibility (a), top-view following coagulation (b), top-view (c) and side-view (d) following clot elimination from the biocompatible SLIPS. Reproduced with permission from Ref [132]. Copyright 2015 American Chemical Society.¹³²



Figure 4-19. Pictures showing how blood was repelled from the biocompatible SLIPS after it was dropped (left), as it was sliding (centre) and after it slid off (right). Reproduced with permission from Ref [132]. Copyright 2015 American Chemical Society.¹³²

4.4 Conclusions

In the above part, a non-fluorinated slippery liquid-impregnated coating consisting of a textured polyelectrolyte multilayer with biodegradability and plant oil with biocompatibility was presented. The underlayer possessed crosslinking and displayed stability under physiological conditions. The surface energy pointed to the immiscibility of almond oil and blood, thus providing a theoretical justification that the development of a non-fluorinated SLIPS coated with almond oil as a porous multilayer was feasible and practical. The constituent materials exhibited an anti-thrombogenic effect as they repelled blood and, by contrast to other coatings of varying surface wettability, hindered blood from coagulating too fast. Furthermore, the materials displayed environmental durability for one month and their transmittance was maintained at around 90%. The inexpensive, environmentally safe and uncomplicated LbL technique that was employed to develop this film is applicable to curved surface coating irrespective of the curvature radius. There is a strong possibility that this SLIPS comprising an underlayer and lubricant fluid, both of which displayed biocompatibility, could preserve its properties for more than a couple of hours during use in surgical interventions. Furthermore, the fluid-infused surface may be better understood by developing a non-fluorinated oil surface demonstrating stability on a membrane with porosity. Further research is needed to elucidate its mechanical properties and stability, including resistance to abrasion, but such a material would be useful for the development of anti-fouling surfaces for use in a medical context, especially for endoscopes and stents.

Chapter 5

Responsive SLIPS with Regulation of Optical Transparency and Wettability

5.1 Background

Property change from one state to another has been the main concern of traditional studies of smart surfaces. Besides this, a few strategies, such as chirality-induced switching and biofunctionalisation, have been developed to create materials whose features can be adjusted in a dynamic manner.^{138,139} For instance, changes in ambient temperature trigger immediate adjustments in the wettability and transmittance of poly(N-isopropylacrylamide) (PNIPAAm) coatings, owing to the fact that the adjustable hydrogen-bonding interactions in the surroundings of PNIPAAm chains causes them to contract and stretch in a reversible manner.¹⁴⁰ This makes PNIPAAm coatings multifunctional smart surfaces of high efficiency and they have indeed been used for a long time. However, adjusting the surface structure and chemical make-up in keeping with the necessities of a smart surface is challenging and poses considerable obstacles to the accomplishment of effective transmittance control and repellence of liquids with low surface tension in solid surfaces.

In such materials, an underlayer demonstrating porosity and low surface free energy traps the perfluorinated lubricant oil and gives rise to omniphobic and self-cleaning capabilities. Furthermore, a range of functions can be fulfilled by SLIPSs created from hydrophobic

underlayers and lubricant oils in different combinations.^{141,142} Bioinspired SLIPSs with thermal-healing attributes were designed in one study as a novel type of cross-species.¹⁴³ Meanwhile, a different study developed organogel SLIPSs with water adhesion switching dependent on temperature.¹⁴⁴ Additional studies have presented other surface functions, such as a self-standing gel SLIPS developed through nanoscale-phase separation,¹⁰² a SLIPS with antireflection and 97% transmittance,¹⁰⁶ and an anti-thrombogenic SLIPS with biocompatibility created *via* the technique of LbL self-assembly.¹³² Hence, close attention must be paid to the choice of underlayer and lubricant oil in the creation of functional SLIPSs according to their planned usage.

With adjustment of their transparency and wettability properties achieved by applying a graded mechanical stimulus, the smart, super-slippery surfaces underpinned by fluid-impregnated porous films were first created by Aizenberg and colleagues.²⁷ Lower light transmission in visible wavelengths is achieved due to the heightened dispersal of light at the interface between liquid and gas, which in turn is the outcome of increased film strain that gives rise to an expansive area with empty and open pores. At the same time, the surface adopts an undulating shape owing to the stretched film and thus droplets of water are captured on the rough surface. According to the findings of the cited studies, SLIPSs could facilitate the development of smart surfaces possessing optical transparency and wettability whose control can be concomitantly achieved through introduction of external stimuli, provided that variation of the lubricant oil structure or underlayer topography enables concomitant control of the outermost surface structure and of the scattering factor. Solar panels, medical devices and smart windows could all benefit from the use of thermal-responsive, anti-fouling SLIPSs with adjustable transparency.^{145,146}

Substitution of the fluoride oils trapped in the surface spaces with paraffin that transforms from solid to liquid when exposed to temperature higher than its melting point is

the principle on which these films have been developed. Under such circumstances, the ambient temperature determines whether the droplets of water on the composite surface are repulsed or captured. The scattering factor of the paraffin layer as well as the thin film surface topography can be adjusted if solid/liquid transmutable and liquid paraffin can be mixed. Hence, ambient temperature is conducive to the achievement of broadband optical transparency and wettability switching that can be adjusted.

In the following part, discussion focuses on the temperature-activated solidifiable/liquid paraffin-infused porous surfaces (TA-SLIPSs) with concomitant control of transparency and water droplets at room temperature (Figure 5-1). The LbL self-assembly technique was applied to develop surfaces demonstrating porosity and consisting of nanofibres (CHINFs) and poly(acrylic acid) (PAA). What makes LbL self-assembly an ideal technique for SLIPS development is the fact that it is affordable, environmentally sustainable, easy to use, and enables coating of expansive curved surface areas, irrespective of the curvature radius.^{39,72,124} The layer of lubricant oil added to the nanofibrous surfaces with hydrophobicity following nanofibrous LbL film hydrophobization was a solidifiable paraffin combined with liquid paraffin. The lubricant layer's surface morphology and the size as light-transmission inhibitor were altered when paraffin solidified. Consequently, the ratio of solidifiable paraffin to liquid paraffin could serve as regulator of the thermal-based droplet motion and light transmittance. Multifunctional systems with temperature sensitivity warrant more research to refine them for anti-fouling applications and aid the creation of surfaces with adjustable transparency that could be used in the medical field, such as transparent endoscopes that can repel blood and anti-scratch lenses, and for smart, anti-fouling windows with optical transparency and opacity during the day and during the night, respectively.

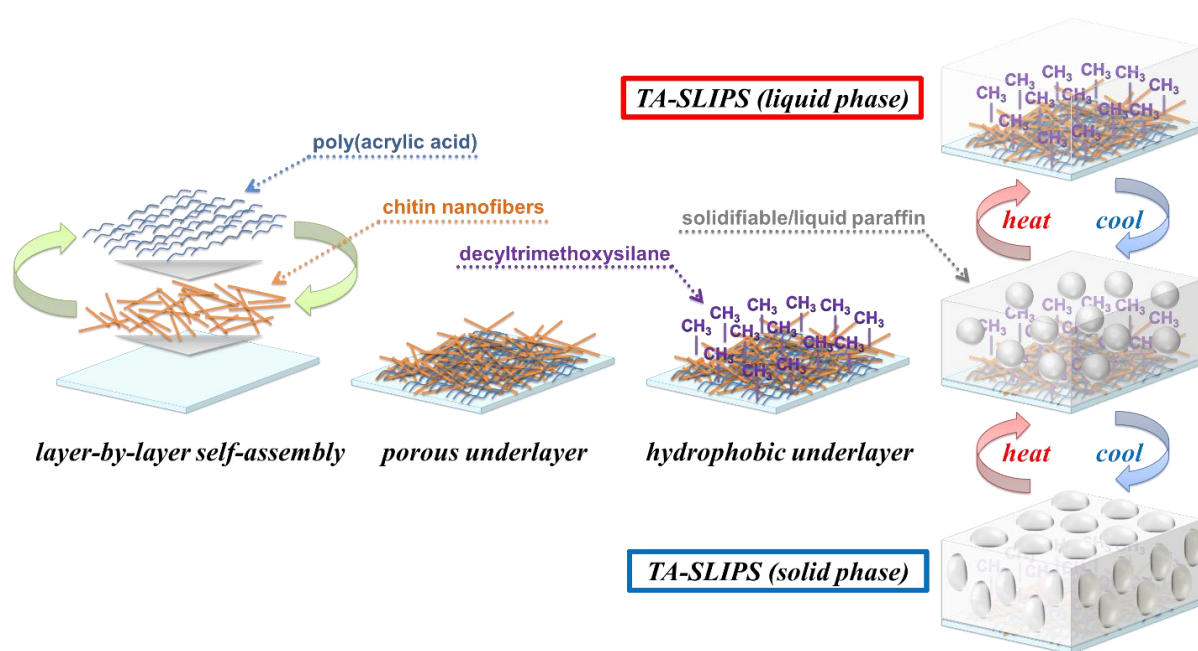


Figure 5-1. Simplified representation of TA-SLIPS: CHINFs and PAA make up the porous underlayer developed through the method of LbL self-assembly; functionalization of the hydrophilic nanofibrous underlayer produced the hydrophobic underlayer, while introduction of the solidifiable/liquid paraffin in the hydrophobic nanofibrous membrane resulted in the super-slippy surface with temperature sensitivity. Reproduced with permission from Ref [147]. Copyright 2016 American Chemical Society.¹⁴⁷

5.2 Experiment

5.2.1 Materials

The development of the films required the use of the following materials: crab shells (Kawai Hiryo, Iwata, Japan), PAA ($M_w \sim 100$ kg/mol, 35 wt% aqueous solution, Sigma-Aldrich,

St. Louis, MO, USA), DTMS (Shin-Etsu Chemical Co., Ltd., Tokyo, Japan), liquid paraffin (Kanto Chemical Co., Inc., Tokyo, Japan), paraffin oil (melting point: 58~60°C, Wako Pure Chemical Industries, Ltd., Osaka, Japan), and glass substrates (76 × 26 mm, thickness: 1.0 mm, refractive index: 1.52, Matsunami Glass Ind., Ltd., Kishiwada, Japan). Ultra-pure water (Aquarius GS-500.CPW, Advantec, Japan) was the principal element of every LbL dipping suspension, while acetic acid (Kanto Chemical Co., Inc., Tokyo, Japan) was used to tune the pH of the suspension. Potassium hydroxide (1:120:60 wt% KOH/H₂O/IPA) was used to clean the glass substrates for 120 seconds followed by rinsing with ultra-pure water prior to usage. Kanto Chemical Co., Inc. (Tokyo, Japan) supplied the hydrochloric acid, sodium hydroxide, sodium chlorite, and sodium borohydride.

5.2.2 Chitin nanofibre refinement

The production of CHINFs began with purification of the crab shells following the protocol presented earlier.^{107,108} The mineral salts were eliminated by treating the powder of crab shells in 2 M hydrochloric acid for 48 hours at ambient temperature. Distilled water was used to rinse the chitin powder, which was then subjected to heating under reflux in 2 M sodium hydroxide for 48 hours for removal of proteins. Subsequently, 1.7 wt% sodium chlorite in buffer solution was used for 360 minutes at a temperature of 80°C to eliminate the pigment. After rinsing with distilled water, the sample was suspended in 33 wt% sodium hydroxide with a content of sodium borohydride. The suspension consisting of CHINFs, sodium hydroxide and sodium borohydride was centrifuged at 5000 rpm for 5 minutes to clean it repeatedly with pure water. This was followed by dilution of the CHINF suspension to 0.025 wt% concentration and then dispersal through ultrasonication.

5.2.3 Production of the mix of paraffin oil and liquid paraffin

Liquefaction of the solidified paraffin oil was achieved by incubating it thermally for 180 minutes at a temperature of 90°C. Furthermore, in the same thermal incubator, mixture of the liquefied paraffin oil and the liquid paraffin was mixed in various ratios (solidifiable: liquid paraffin = vol. ratio of 1:10, 1:15, 1:20, 1:25, 1:30, 1:35, 1:40, 1:45 or 1:50) and stirred for 720 minutes at 90°C.

5.2.4 TA-SLIPS development

The underlayer employed consisted of porous films developed with the LbL technique based on suspension of refined CHINFs and PAA. Alternate immersion of a glass substrate in the cationic CHINF suspension (0.025 wt%, pH 3) and the anionic PAA suspension (1 mM, pH 3) was performed for 60 seconds, followed by rinsing with pure water for 180 seconds and air-drying from 10 mm away at 0.05 MPa after each layer was deposited. About two-thirds of the glass substrates were coated with the films, while the rest was bare glass. CVD was employed to perform film hydrophobization. A film demonstrating porosity and with the lowest refractive index, a glass bottle with a volume of 2 mL, and also comprising 200 μL DTMS was introduced into a glass bottle with a volume of 100 mL. The system was thermally incubated for 150 minutes at 140°C. After the film was hydrophobized, a mixture of solidifiable paraffin oil and liquid paraffin (1 $\mu\text{L cm}^{-2}$) was dropped on it at a temperature of 60°C. Nitrogen gas was blown on the surface to eliminate any extra paraffin oil from the film.

5.2.5 Characterization

Characterisation of the film surface morphology was undertaken through field emission scanning electron microscopy (FE-SEM) (S-4700, Hitachi, Japan) at 3 kV accelerating voltage, while the chemistry of the porous surfaces was analysed with X-ray photoelectron spectroscopy (XPS, JPS-9010TR, JEOL, Tokyo, Japan) with an $\text{MgK}\alpha$ laser. A spectrophotometer (UVmini-1240, Shimadzu, Kyoto, Japan) allowed the light transmittance to be measured over a spectral range of 300-900 nm spectral range. A colour three-dimensional scanning microscope (VK-9710, Keyence, Osaka, Japan) was employed to examine the film topography, while ellipsometry (MARY-102, Five Lab, Saitama, Japan) (measuring model: rotating retarder method; light source: 0.8 mW HeNe Laser at 632.8 nm; beam diameter: 0.8 mm; fixed incident angle: 45° ; sample time: 0.05 sec, refractive index of glass: 1.52, absorption index of glass: 0.0203) permitted measurement of how thick the films were and of the refractive index of the underlayer with porosity that covered the glass substrate. A contact angle meter (CA-DT, Kyowa, Saitama, Japan) was used at various surface temperatures to determine the contact and sliding angles of a 10 μL droplet at room temperature. Last but not least, a haze meter (NDH-5000, Nippon Denshoku Industries, Tokyo, Japan) alongside an optical source in the form of a diode with light emission (5 V, 3 W) was employed to determine the film values of T.T., P.T., DIF and HAZE.

5.3 Results and Discussion

5.3.1 Porous (CHINF/PAA) underlayer

The LbL self-assembly technique was applied to develop the CHINF- and PAA-based films demonstrating hydrophilicity and porosity. The CHINF network constituted the foundation of the CHINF/PAA underlayer's porous structure, which expanded in proportion with the number of bilayers (Figure 5-2, first line). Porosity was also found to increase with increasing number of bilayers according to the ellipsometry analysis, whereas the refractive index declined up to ten bilayers. Nevertheless, compared to the smallest value of the film with ten bilayers, the films with twelve and fourteen-bilayers had higher refractive index values owing to PAA accumulation (Figure 5-2, third line), which was more intense in these latter two films, as indicated by SEM analysis. Hence, the ensuing experiments were conducted with the 10-bilayer film. The following straightforward mixing rule can be applied to determine the refractive index of an LbL film, in line with the Fresnel equations:¹¹⁰

$$n_l = f_{air}n_{air} + f_{polyelectrolyte1}n_{polyelectrolyte1} + f_{polyelectrolyte2}n_{polyelectrolyte2} \quad (5-1)$$

In the above, f_x and n_x respectively denoted the volume fraction and refractive index of component x . This equation implies that porosity increases as the LbL film refractive index declines, while porosity diminishes as the LbL film refractive index increases. The process presented in the experiment part enabled effective refinement of the CHINFs, as can be seen in the SEM image of the film with four bilayers. Furthermore, CHINF accumulation led to stacked nanofibres without disruption of film pores and the pores were filled with PAA, as indicated in a TEM and DLS images of chitin nanofibers (Figures 5-3 and 5-4). In other words, increase in the number of bilayers caused accumulation of PAA on the surface, confirming that, as the film became thicker, the refractive index diminished.

Once the ten-bilayer CHINF/PAA underlayer demonstrating porosity was hydrophobized, exposure to 140°C temperature for the DTMS CVD process caused the film to shrink and consequently it lost some of its thickness, from 79.2 to 76.2 nm (Table 5-1). On the other hand, the film shrinking and the content of extra DTMS heightened the refractive index from 1.34 to 1.39, diminishing porosity to a small degree.

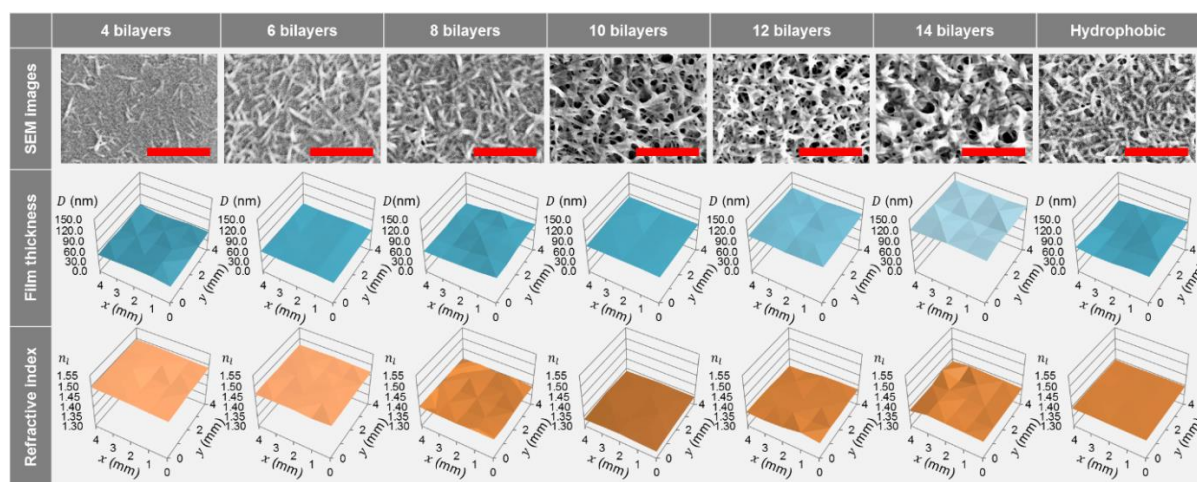


Figure 5-2. The porous underlayers with varying number of bilayers imaged with FE-SEM at 1 μm scale bar (first line), film thickness (second line) and refractive index (third line) as well as the porous underlayer showing hydrophobicity (first line). Ellipsometry was applied to determine the film thickness (D) and refractive index (n_l) across a 4×4 mm area. Reproduced with permission from Ref [147]. Copyright 2016 American Chemical Society.¹⁴⁷

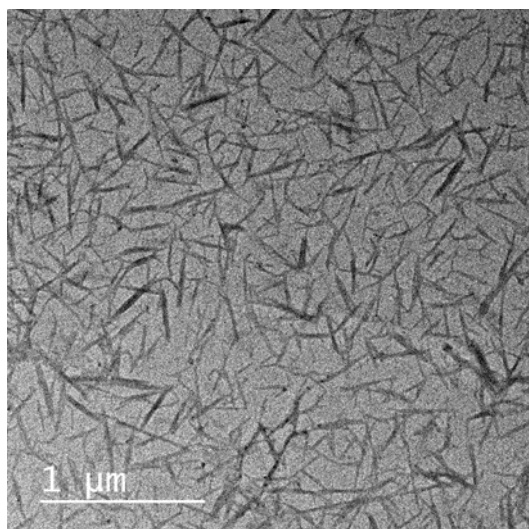


Figure 5-3. Chitin nanofibres imaged with TEM. Reproduced with permission from Ref [147].

Copyright 2016 American Chemical Society.¹⁴⁷

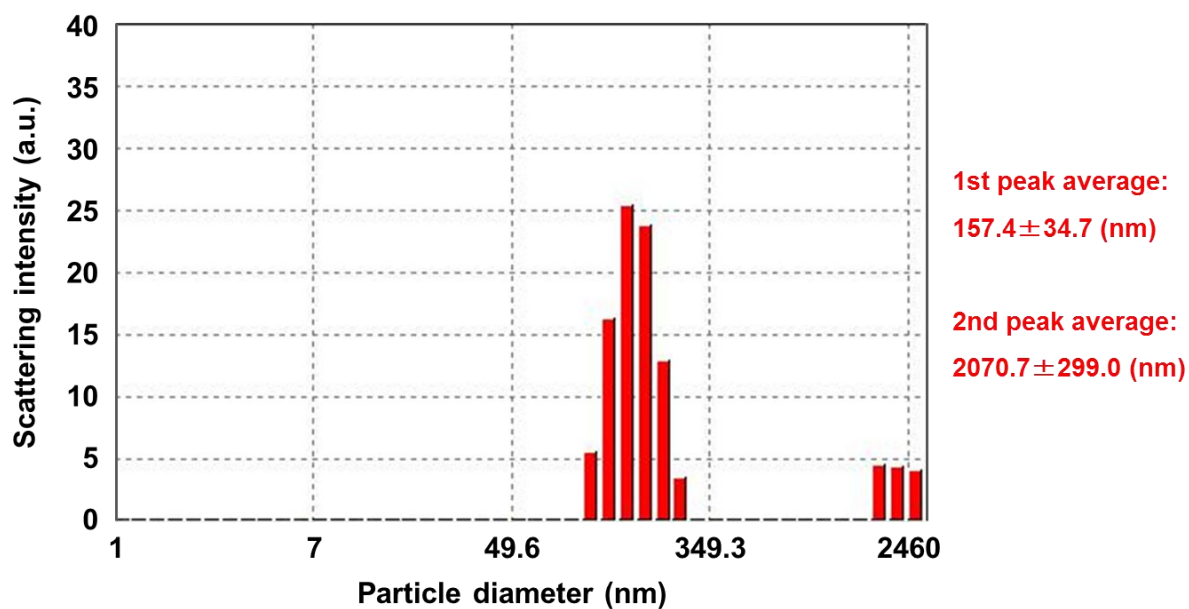


Figure 5-4. DLS image showing the average particle diameter associated with every peak.

Reproduced with permission from Ref [147]. Copyright 2016 American Chemical Society.¹⁴⁷

Table 5-1. The thickness and refractive index of porous underlayers with varying number of bilayers and the porous underlayer demonstrating hydrophobicity. Reproduced with permission from Ref [147]. Copyright 2016 American Chemical Society.¹⁴⁷

	4	6	8	10	12	14	Hydro phobic
	bilayers	bilayers	bilayers	bilayers	bilayers	bilayers	
Thickness (nm)	54.1	61.8	70.4	79.2	106.8	126.2	76.2
Refractive index	1.49	1.47	1.40	1.34	1.38	1.39	1.39

The presence of CHINFs and PAA in the films was confirmed by XPS analysis, which indicated the occurrence of the main peaks of CHINFs and PAA, namely, C-C, C-O, and O=C-O bonds (Figure 5-5a and b). The presence of a multitude of C-C bonds in the DTMS-modified films pre- and post-DTMS CVD was also validated and engendered a low surface energy.

A molecular layer with hydrophobicity and of minimal thickness was produced from the reaction between DTMS and hydroxyl groups from the porous CHINF/PAA underlayer. The hydrophilicity of the porous film was converted into hydrophobicity by the CVD process, with a $108.7 \pm 0.95^\circ$ contact angle of water (Figure 5-5c). Before it was hydrophobized, the hydrophilic porous film had almost zero contact angle due to its wettability state and water-soluble polymer assimilation. To evaluate whether the SLIPS criteria below were satisfied by the hydrophobized film, measurement of the contact angles of water and liquid paraffin oil of the hydrophobic film was performed (Figure 5-5d):^{22,148}

$$\Delta E_1 = R(\gamma_{oa} \cos \theta_o - \gamma_{wa} \cos \theta_w) - \gamma_{wo} > 0 \quad (5-2)$$

$$\Delta E_2 = R(\gamma_{oa} \cos \theta_o - \gamma_{wa} \cos \theta_w) + \gamma_{wa} - \gamma_{oa} > 0 \quad (5-3)$$

In the above, the total interfacial energy per unit area associated with the wetting morphology 1 is denoted by E_1 , while the total interfacial energy per unit area associated with the wetting morphology 2 is denoted by E_2 . The working conditions for the maintenance of the stability of a film impregnated with liquid are highlighted by each delta (Figure 5-5d), while the interfacial tension between two phases is denoted by γ_{xy} , as defined by the subscripts w (water), o (liquid paraffin oil), and a (air). Furthermore, the contact angle of liquid paraffin oil on the hydrophobic multilayer on an air background is represented by θ_o , while the contact angle of water on the hydrophobic multilayer on an air background is given by θ_w . The underlayer's roughness factor R is a function of ratio between the solid–liquid area A_{SL} and its projection on a flat plane A_F whose expression takes the form of a contact angle of water for a rough and smooth surface:^{148,149}

$$R = \frac{A_{SL}}{A_F} = \frac{\cos \theta_w}{\cos \theta} \quad (5-4)$$

The value of θ on the smooth glass substrate coated by DTMS post-CVD is $99.4 \pm 0.23^\circ$. The Fowkes equation was applied to determine γ_{wo} :

$$\gamma_{wo} = \gamma_{oa} + \gamma_{wa} - 2(\gamma_{oa}^\alpha \gamma_{wa}^\alpha)^{\frac{1}{2}} \quad (5-5)$$

The contributions made by the liquid surface tensions to the dispersion force are indicated by γ_{oa}^α and γ_{wa}^α . The water surface tension contributed 21.8 mN/m to the dispersion force. In the case of materials without polarity, $\gamma_{oa}^\alpha \approx \gamma_{oa}$.^{22,148}

The CHINF-based nanotopography exhibited by the films instead of microtopography meant that the CVD process could not turn them into superhydrophobic films. The SLIPS criteria were fulfilled by the hydrophobic film with porosity and a stable liquid surface (Table 5-2), suggesting that the film possessed a SLIPS with a nanofibrous underlayer demonstrating porosity and a lubricant layer in the form of the liquid paraffin oil.

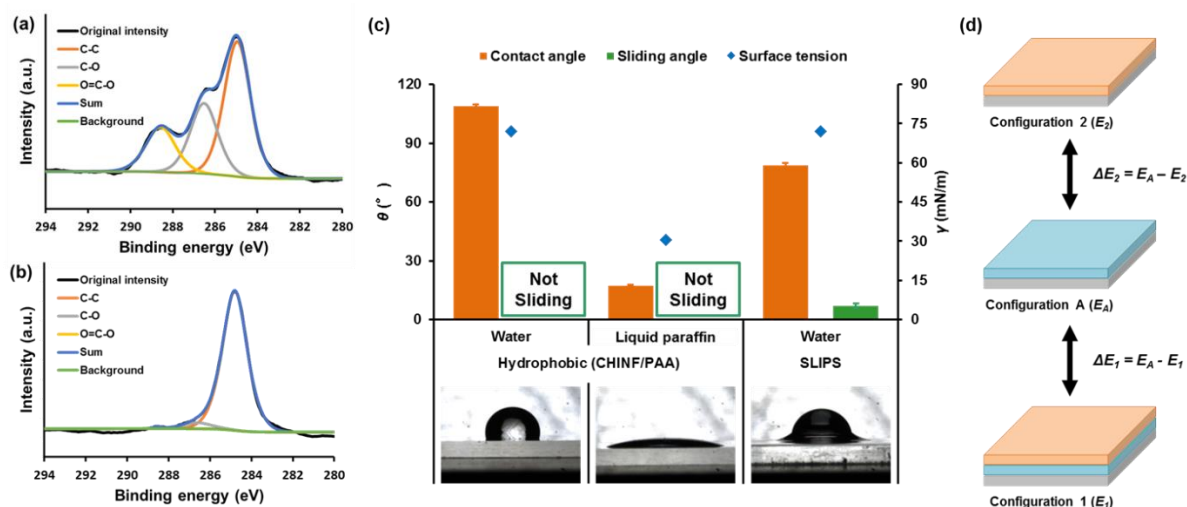


Figure 5-5. C_{1s} core-level spectra of the underlayer with porosity (a) pre- and (b) post-hydrophobization by DTMS. The initial intensity is denoted by the black line, C-C is denoted by the orange line, C-O is denoted by the grey line, O=C-O is denoted by the yellow line, sum is denoted by the blue line, and background peaks are denoted by the green line. (c) The orange and green bars and the blue diamonds respectively denote the contact angle, sliding angle and surface tension of water and liquid paraffin oil on a porous CHINF/PAA film that was subjected to hydrophobization and on a SLIPS created through the addition of liquid paraffin oil in a drop-wise fashion to the hydrophobized porous film. Below: equivalent pictures of liquid drops on various films. (d) The total interfacial energy per unit area for the wetting configuration 1 is denoted by E_1 , the total interfacial energy per unit area for the wetting configuration 1 is denoted by E_2 and the total interfacial energy per unit area for the wetting configuration 1 is denoted by E_A . Every delta is indicative of a key criterion for the maintenance of the stability of a lubricating film on a functional SLIPS in the working conditions outlined in equations (5-2) and (5-3). Reproduced with permission from Ref [147]. Copyright 2016 American Chemical Society.¹⁴⁷

Table 5-2. The contact angle and surface tension associated with water and liquid paraffin oil as well as the determined interfacial tension and spreading coefficient between the two liquids.

Reproduced with permission from Ref [147]. Copyright 2016 American Chemical Society.¹⁴⁷

water			liquid paraffin oil			γ_{wo} (mN/m)	R	ΔE_1	ΔE_2	$S_{ow(a)}$
γ_{wa} (mN/m)	θ_w (°)	γ_{wa}^α (mN/m)	γ_{oa} (mN/m)	θ_o (°)	γ_{oa}^α (mN/m)					
72.1	108.7	21.8	24.8	17.2	24.8	50.4	2	43.2	140.9	-3.1

The spreading coefficient dictates the coating criterion in the following way:²⁶

$$S_{ow(a)} = \gamma_{wa} - \gamma_{wo} - \gamma_{oa} \quad (5-6)$$

$S_{ow(a)} > 0$ and $S_{ow(a)} < 0$ respectively indicate that the droplet of water will be covered by lubricant fluid that can evaporate without difficult and that the droplet of water will not be covered by the lubricant fluid that will be retained in the porous underlayer without evaporation. As can be seen in Table 5-2, $S_{ow(a)}$ had a value of -3.1 in the case of SLIPs with liquid paraffin oil, meaning that the porous multilayer was covered by lubricant fluid that possessed stability.

The criterion highlighted above was established at room temperature. A mixture of solidifiable and liquid paraffin made up the TA-SLIPs and the volume ratio of this mixture determined the melting point. Hence, this approach was not easily applicable to the TA-SLIPs. Nevertheless, the criterion should be assumed to have been satisfied by the TA-SLIPs, which acquired stability upon surface conversion from solid to liquid phase, according to research on SLIPs created on the basis of the premise that liquid paraffin was the lubricating oil associated with the liquid phase.

5.3.2 TA-SLIP surface wettability

TA-SLIPS surface wettability was examined at various temperatures following enrichment of the hydrophobic porous underlayer with the mix of solidifiable and liquid paraffin. The volume ratio of this mix caused a significant decline in the contact and sliding angles at specific temperatures (Figure 5-6a and b), confirming that the solidifiable to liquid paraffin ratio determined the temperature of the paraffin mix conversion from liquid to solid at the surface. At 1:25 volume ratio, the following results were obtained at various temperatures. Close to the transition temperature of around 28°C, there was a fast decline in the contact angle of water, from $99 \pm 4.82^\circ$ to $53 \pm 3.98^\circ$ (Figure 5-6a). Furthermore, it was observed in the sample images that the rise in surface temperature prompted the paraffin mixture to convert from solid to liquid phase at the surface (Figure 5-6c). The rise in temperature from 22 to 30°C also caused a decline in the sliding angle of 10 μ L water droplets (Figure 5-6b), which enabled the droplets to slide freely instead of being trapped. The modification of TA-SLIP surface tension was identified as the source of this phenomenon, since it was conducive to droplet movement, particularly in the proximity of the transition temperature. By contrast, when the temperature was less than 22°C, the water droplets did not slide, not even after inclining the solidified paraffin surface at 90°. The microtopography of the paraffin mixture created when the temperature dropped confirmed this result (Figure 5-6d). Moreover, close to the transition temperature, the paraffin surface in the Wenzel state shifted to the SLIPS state. These observations suggest that increasing or decreasing the temperature in relation to the transition temperature helped to regulate the attachment behaviour of TA-SLIPSs to the droplets of water.

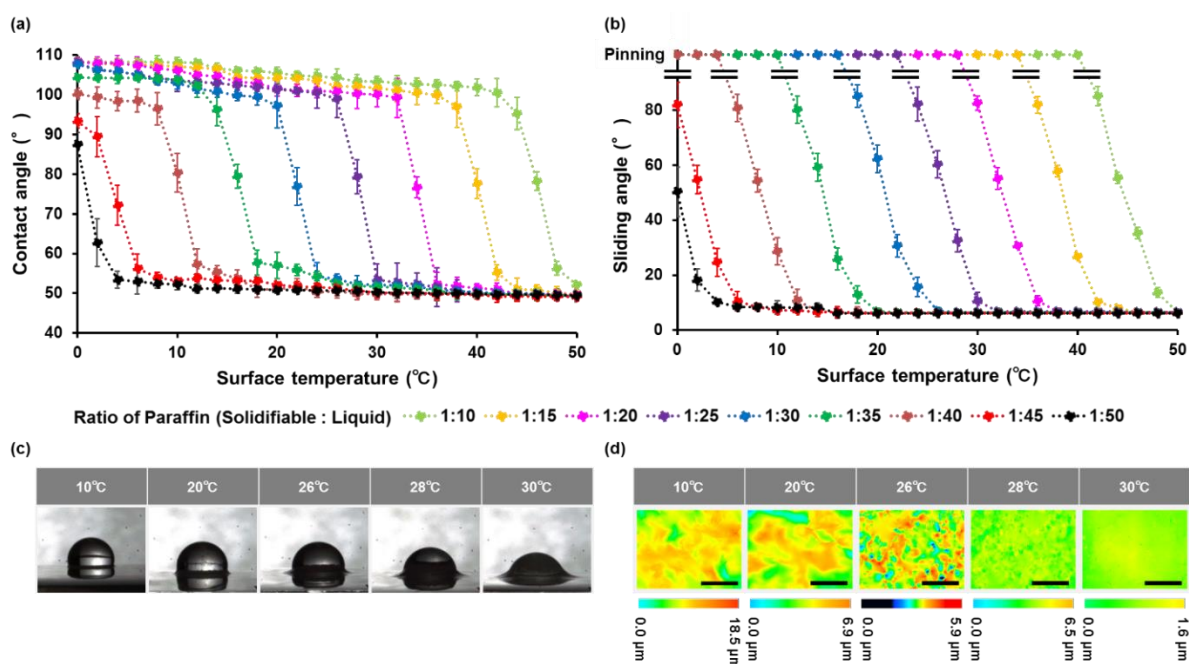


Figure 5-6. The paraffin mixture volume ratio dictating the contact angle (a) and sliding angle (b) of a 10 μL water droplet at various temperatures (solidifiable: liquid paraffin = 1:10, lime-green line; 1:15, yellow line; 1:20, pink line; 1:25, purple line; 1:30, blue line; 1:35, green line; 1:40, brown line; 1:45, red line; and 1:50, black line). (c) Charged-couple device camera images of 10 μL water droplet on a TA-SLIPS at a volume ratio of 1:25 at various temperatures. (d) TA-SLIPS with a volume ratio of 1:25 imaged at various temperatures with colour two-dimensional laser scanning microscopy. Below: equivalent scale bars of roughness, while the black scale bars are all 100 μm . The supporting information provides three-dimensional images of greater size. Reproduced with permission from Ref [147]. Copyright 2016 American Chemical Society.¹⁴⁷

Colour three-dimensional laser scanning microscopy facilitated examination of the impact of temperature on surface structure as well as enabling measurement of surface topography and surface roughness (Ra and RMS) (Figure 5-7). The micro-ordered rough topography of the TA-SLIPS structure transformed into a nano-ordered smooth surface as the temperature rose.

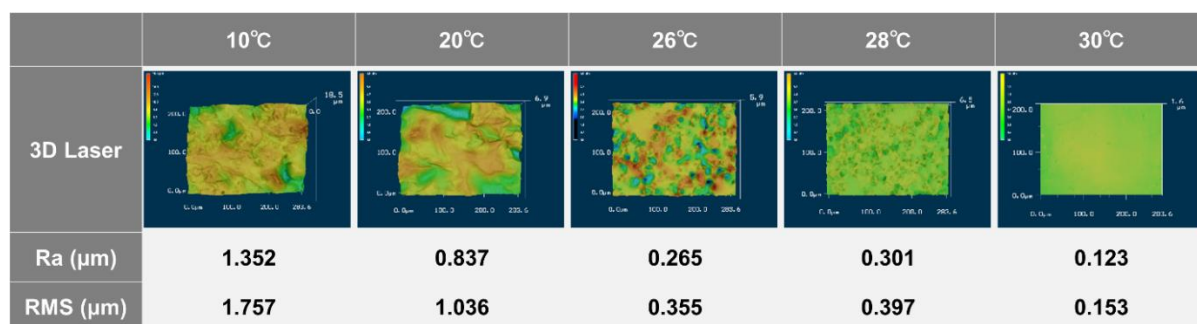


Figure 5-7. TA-SLIPSs imaged with colour three-dimensional laser scanning microscope at various temperatures. Below: surface roughness (Ra and RMS) associated with various temperatures. The X axis is 200 μm and the Y axis is 283.6 μm. Reproduced with permission from Ref [147]. Copyright 2016 American Chemical Society.¹⁴⁷

A high-speed camera (HAS-D3, Ditect, Tokyo, Japan) was employed to gather time-resolved images of a 10 μL water droplet on a TA-SLIPS to determine how the wetting process on the film was affected by temperature (Figure 5-8).

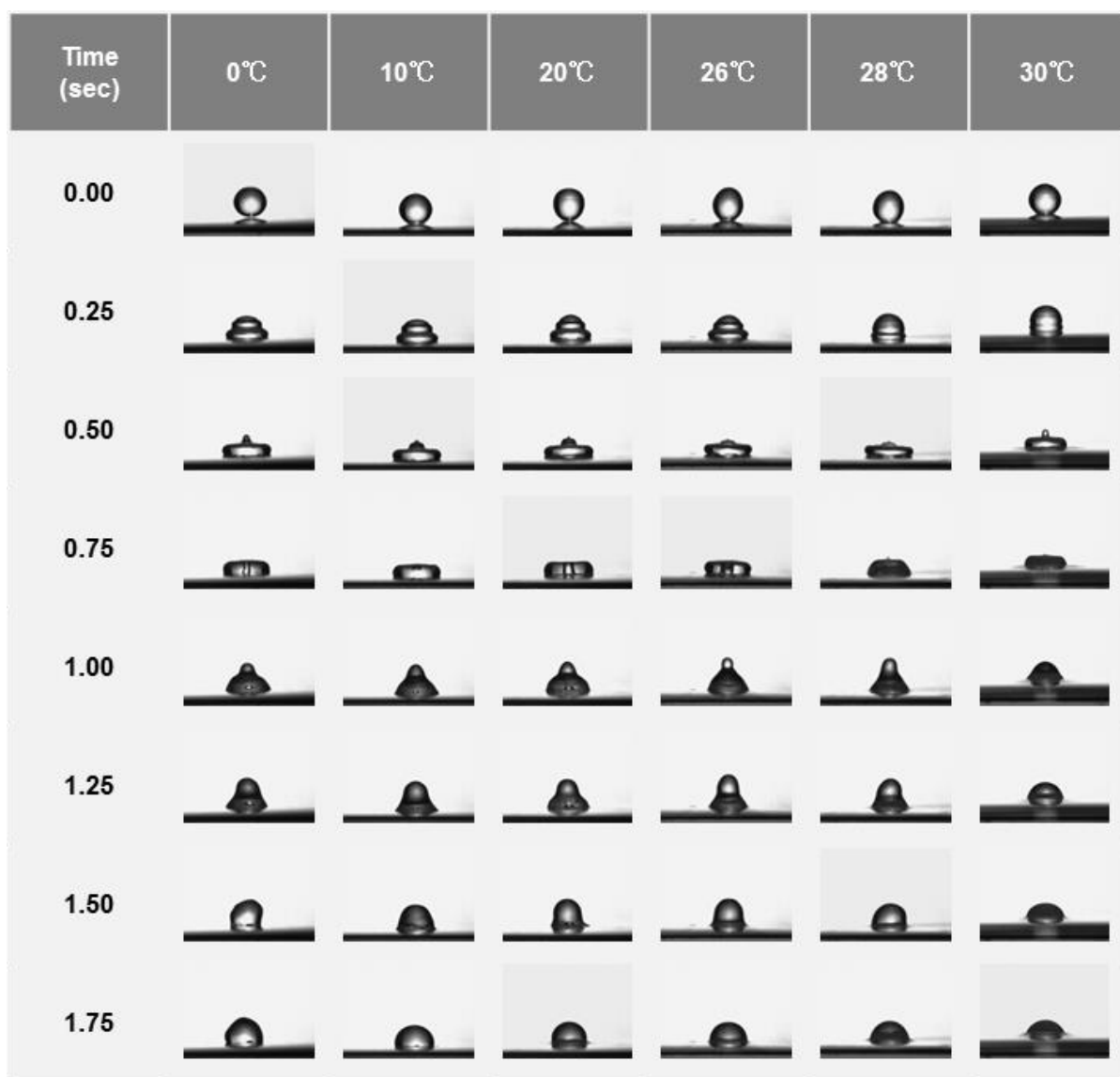


Figure 5-8. Time-resolved images taken with a high-speed camera showing TA-SLIPSs at various temperatures. Reproduced with permission from Ref [147]. Copyright 2016 American Chemical Society.¹⁴⁷

Integration of Berthelot's rule with the Young equation yielding enables determination of the surface tension of solidifiable/liquid paraffin:¹⁵⁰

$$\cos\theta = -1 + 2\sqrt{\gamma_{SV}/\gamma_{LV}} \quad (5-7)$$

The contact angle (θ) and liquid-vapour surface tension (γ_{LV}) enable calculation of the solid-vapour surface tension (γ_{SV}). The surface tension of solid and liquid paraffin can be determined as follows.

(i) *Paraffin in liquid state*

Liquid paraffin surface tension can be calculated as

$$\gamma_{oa} = 4\gamma_{sa}/(1 + \cos\theta_o)^2 \quad (5-8)$$

The porous underlayer (γ_{sa}) surface energy can be calculated as

$$\gamma_{sa} = (1 + \cos\theta_w)^2\gamma_{wa}/4 \quad (5-9)$$

When equations S3 and S4 are combined, the following is obtained

$$\gamma_{oa} = [(1 + \cos\theta_w)^2/(1 + \cos\theta_o)^2]\gamma_{wa} \quad (5-10)$$

(ii) *Paraffin in solid state*

Solid paraffin surface tension (γ_{oa}) can be calculated as

$$\gamma_{oa} = (1 + \cos\theta_w)^2\gamma_{wa}/4 \quad (5-11)$$

In the above, θ_w , denotes the contact angle of water on solid paraffin.

Since constant temperature water was used to determine θ_w and θ_{wr} , γ_{wa} had a fixed value of 72.1 mN/m. Differential scanning calorimetry (DSC) was applied to determine the melting temperature of every paraffin mixture (Figure 5-9). Figure 5-10 indicates the surface tension obtained for solidifiable/liquid paraffin. Compared to the measured melting points, the transition points on the TA-SLIPs with varying paraffin mixture volume ratio differed to a minor extent, as shown by the contact and sliding angle results (Figure 5-6a and b). The present study employed a contact angle meter on a TA-SLIP at various surface temperatures to determine the contact angle and the sliding angle of a 10- μ L droplet of water at room temperature to maintain the water surface tension stable at different temperatures. This was believed to attest to the occurrence of thermal transition at the interface between the droplet of water and TA-SLIP, causing the transition points associated with the contact angle and sliding angle to differ from the DSC-measured melting points.

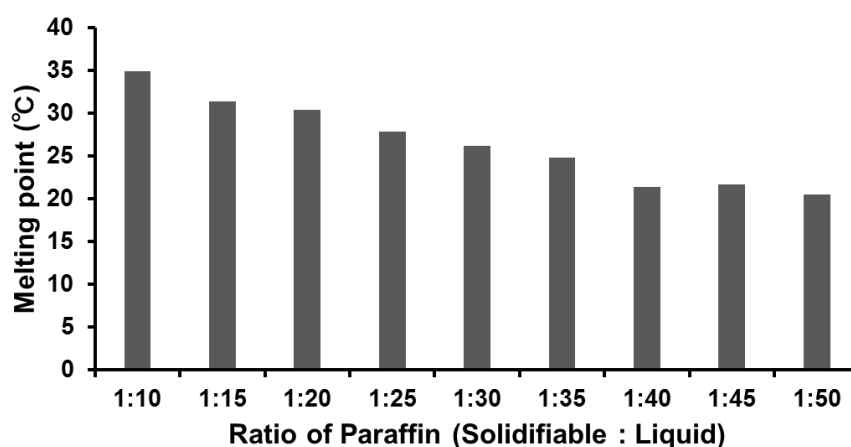


Figure 5-9. The melting point determined according to the paraffin mixture volume ratio. Reproduced with permission from Ref [147]. Copyright 2016 American Chemical Society.¹⁴⁷

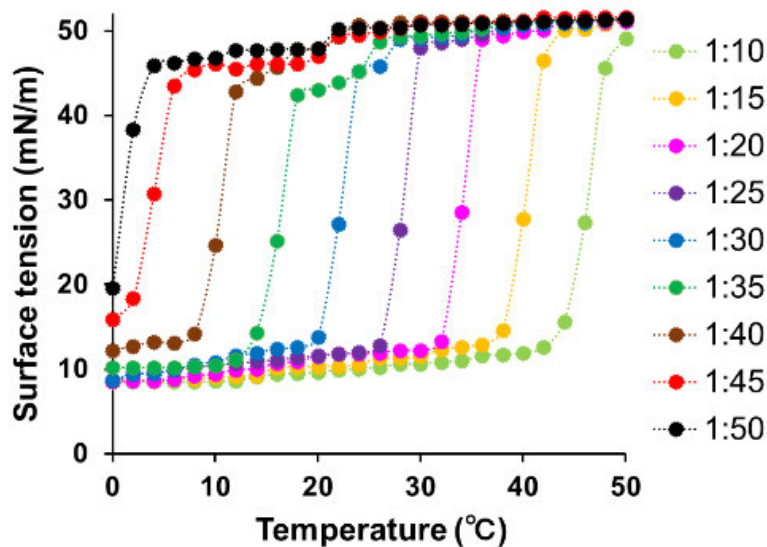


Figure 5-10. The effect of varying temperature on the paraffin mixture surface tension (solidifiable: liquid paraffin = 1:10, lime-green line; 1:15, yellow line; 1:20, pink line; 1:25, purple line; 1:30, blue line; 1:35, green line; 1:40, brown line; 1:45, red line; and 1:50, black line). Reproduced with permission from Ref [147]. Copyright 2016 American Chemical Society.¹⁴⁷

5.3.3 Optical properties of TA-SLIPSs

Several important observations were derived from the analysis of the TA-SLIP optical properties (Figure 5-11). The trends related to transmittance calculated at different temperatures underwent modifications due to the paraffin mixture volume ratio (Figure 5-11a). Based on the premise that solidified paraffin displayed macroscopic sphericity, when solidified paraffin changed into liquid paraffin, the cross-sectional area was decreased, engendering non-linear or quadratic behaviour. At 550 nm, the 4% transmittance of TA-SLIPS with 1:25 volume ratio increased to 91%. Furthermore, TA-SLIPS with this ratio exhibited broadband transmittance susceptible to temperature, as indicated by the results of UV-vis transmittance (Figure 5-11b). A rise in Rayleigh scattering with wavelength dependence meant that the

wavelength dictated the transmittance for surface temperatures between 0 and 10°C. The reason for this is that the TA-SLIP surface roughness acquired a larger root mean square (RMS) due to the lower surface temperatures.¹¹⁷ At wavelength exceeding 400 nm, there was a reduction in wavelength-based transmittance with the rise in temperature (Figure 5-12), the TA-SLIPSs being highly transparent and having more than 90% transmittance.

The optical parameters reflected how the TA-SLIPSs with 1:25 volume ratio performed from an optical perspective (Figure 5-11c). The trends exhibited by the parallel transmittance (P.T.) were not greatly different from those seen in Figure 5-11a and b. Although it rose from 0 to 6°, the diffusion (DIF) did not increase beyond its 6°C peak due to the fact that the solidified TA-SLIPSs microtopography caused backward scattering. Furthermore, the reduction in the wavelength-based scattering was signalled by the fact that, at temperatures lower than 10°C, the total transmittance (T.T.) rose significantly, but at temperatures exceeding 10°C its increase stopped.

The results obtained formed the basis for the optical scattering models that were created to reflect how TA-SLIPSs reacted to temperature (Figure 5-11d). Mie scattering caused forward and backward dispersal of incident light with low DIF at lower temperatures, whereas a rise in temperature caused a decline in backward dispersal and DIF. The DIF nearly vanished following conversion of the solid paraffin mixture to liquid, and P.T. made up most of the transmittance.

The paraffin mixture accumulated at the surface (Figure 5-11d). As anticipated by the optical theory summed up in the equation below,^{116,151,152} scattering was intensified by increased nano/microtopography and surface roughness, leading to reduced surface transmittance:

$$\ln(T/T_0) = -\{2\pi(n_{air} - n_{coating})\cos\theta\}^2(\sigma/\lambda)^2 \quad (5-12)$$

Coating transmittance with surface roughness is denoted by T , while coating transmittance

without surface roughness is denoted by T_0 . The refractive index of x , optical incidence angle of the outermost surface layer, surface roughness RMS and wavelength are respectively denoted by n_x , $\cos\theta$, σ and λ . This equation implies that transmittance is reduced as a result of elevated roughness σ . Provided that $n_{air} = 1.00$, $n_{coating} = 1.48$, and $\theta = 0$, then longer wavelengths should give higher transmittance. The previous observations are corroborated by this relationship.

Information regarding the optical properties could also be derived from the images showing how the TA-SLIPSs with a 1:25 volume ratio responded to temperatures in the range 0-30°C (Figure 5-11e).

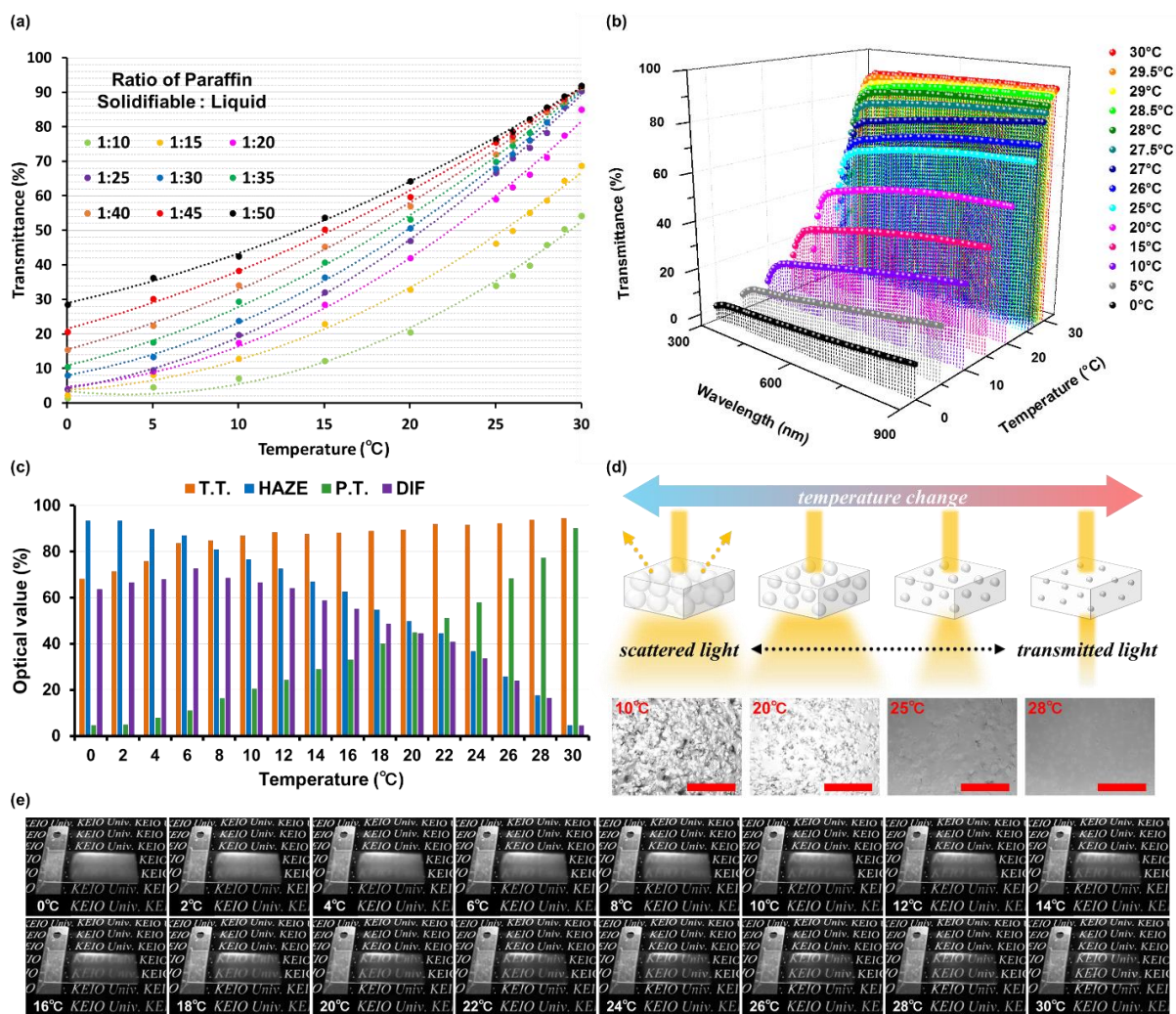


Figure 5-11. (a) The impact of paraffin mixture volume ratio (solidifiable: liquid paraffin = 1:10, lime-green dots; 1:15, yellow dots; 1:20, pink dots; 1:25, purple dots; 1:30, blue dots; 1:35, green dots; 1:40, brown dots; 1:45, red dots; and 1:50, black dots) at various temperatures on the transmittance of TA-SLIPSs at 550 nm. (b) Temperature-based changes in the transmittance of TA-SLIPSs with 1:25 volume ratio (0°C, black dots; 5°C, gray dots; 10°C, purple dots; 15°C, magenta dots; 20°C, pink dots; 25°C, sky-blue dots; 26°C, blue dots; 27°C, dark-blue dots; 27.5°C, dark-green dots; 28°C, green dots; 28.5°C, lime-green dots; 29°C, yellow dots; 29.5°C, orange dots; and 30°C, red dots). (c) Temperature-based T.T., HAZE, P.T. and DIF of TA-SLIPSs with 1:25 volume ratio, as respectively denoted by orange, blue, green and purple bars. The supporting information provides further explanation about the optical parameters. DIF divided by T.T. gave the HAZE, indicating how much light was dispersed with

the passing of light through the film. (d) Temperature-dependent models of TA-SLIP scattering and related digital microscopy imaging of TA-SLIPSs at various temperatures (100 μm scale bar). (e) The effect of temperature rise in the range of 0-30°C at 2°C intervals on the optical performance of TA-SLIPSs with 1:25 volume ratio. Reproduced with permission from Ref [147]. Copyright 2016 American Chemical Society.¹⁴⁷

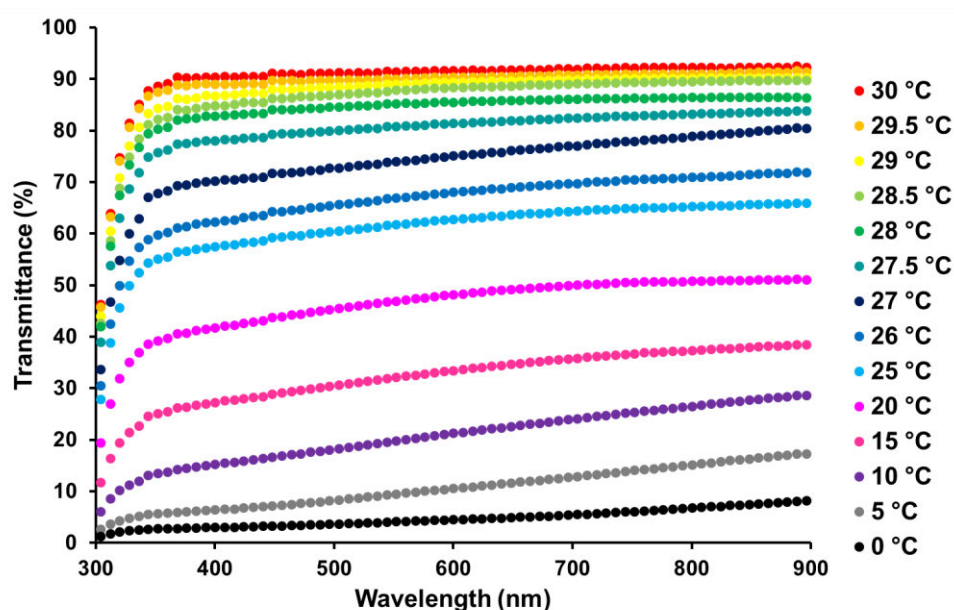


Figure 5-12. Temperature-dependent alterations in the transmittance of TA-SLIPSs with 1:25 volume ratio as seen in two-dimensional imaging (0°C, black dots; 5°C, grey dots; 10°C, purple dots; 15°C, magenta dots; 20°C, pink dots; 25°C, sky-blue dots; 26°C, blue dots; 27°C, dark-blue dots; 27.5°C, dark-green dots; 28°C, green dots; 28.5°C, lime-green dots; 29°C, yellow dots; 29.5°C, orange dots; and 30°C, red dots). Reproduced with permission from Ref [147]. Copyright 2016 American Chemical Society.¹⁴⁷

UV-vis spectroscopy in a quartz cell permitted measurement of paraffin mixture absorbance at various temperatures (Figure 5-13 and 14). The paraffin mixture was confirmed to possess transmittance, even in conditions of significant thickness, as absorbance declined with the rise in temperature.

In keeping with the optical theory (Equation 5-12), dispersal should be intensified by a nano/micro complex surface with high surface roughness in order to reduce transmittance. Equation (5-12) specifies that, provided that $n_{air} = 1.00$, $n_{coating} = 1.48$, and $\theta = 0$, transmittance should be diminished if the roughness σ is increased, longer wavelengths being associated with higher transmittance (Figure 5-15).

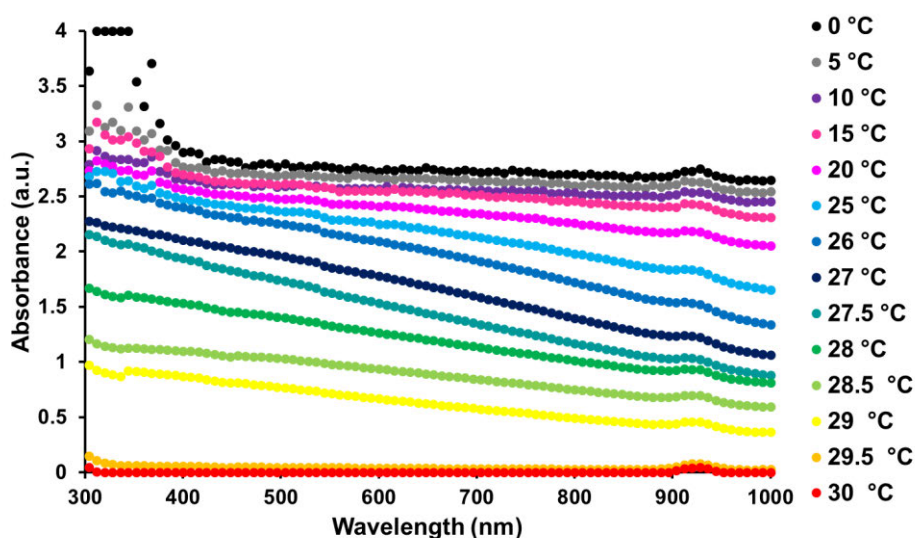


Figure 5-13. Two-dimensional imaging of temperature-based alterations of paraffin mixture absorbance in a quartz cell. Reproduced with permission from Ref [147]. Copyright 2016 American Chemical Society.¹⁴⁷

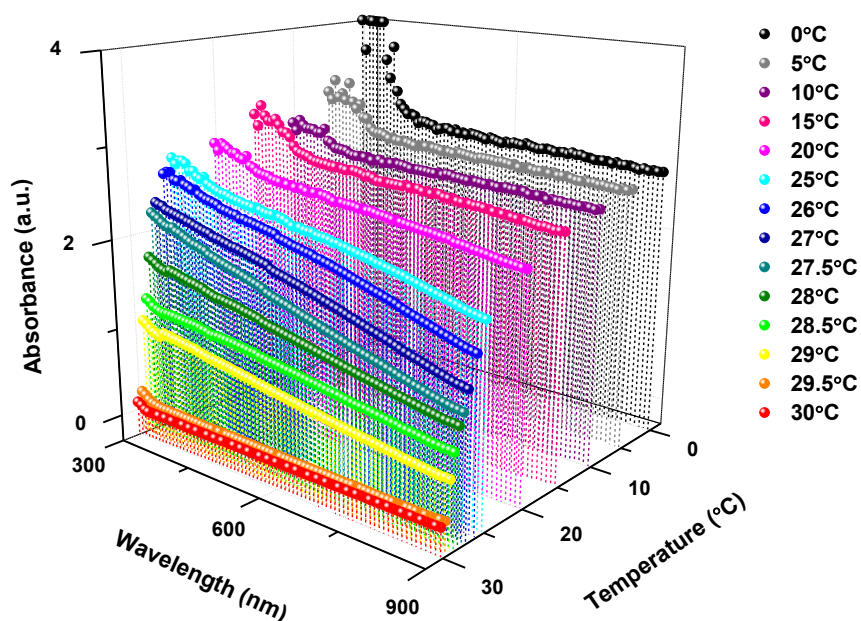


Figure 5-14. Three-dimensional imaging of temperature-based alterations of paraffin mixture absorbance in a quartz cell. Reproduced with permission from Ref [147]. Copyright 2016 American Chemical Society.¹⁴⁷

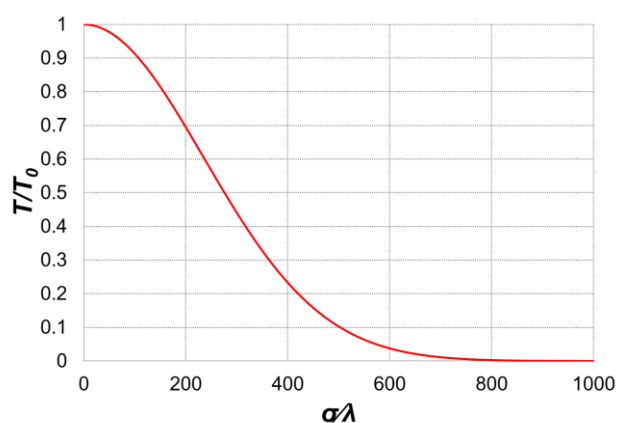


Figure 5-15. Surface roughness and transmittance correlation; T , T_0 , σ and λ respectively denote coating transmittance in the presence and absence of surface roughness, the RMS surface roughness, and the wavelength. Reproduced with permission from Ref [147]. Copyright 2016 American Chemical Society.¹⁴⁷

5.3.4 TA-SLIPS reversible transparency and adhesion switching

To be applicable in various different fields, these kinds of materials must demonstrate surface wettability and optical properties that adjust on an ongoing basis.^{153–155} Aside from being highly transparent, the TA-SLIPSs also showed reversible switching of water droplet attachment (Figure 5-16). Furthermore, modulation of the TA-SLIP transition temperature can be achieved by varying the volume ratio of the paraffin mixture, enabling adaptation of the TA-SLIPS properties in keeping with the specifications of each individual application. The transition temperature is close to 28°C in the case of TA-SLIPSs with 1:25 volume ratio. This ensures TA-SLIPS applicability in intelligent windows with transmittance that can be regulated according to the time of day. As smart coatings, TA-SLIPSs could be employed in medical devices (e.g. endoscopes) to prevent blood adherence and keep them transparent and protected thanks to the solidified paraffin surface.

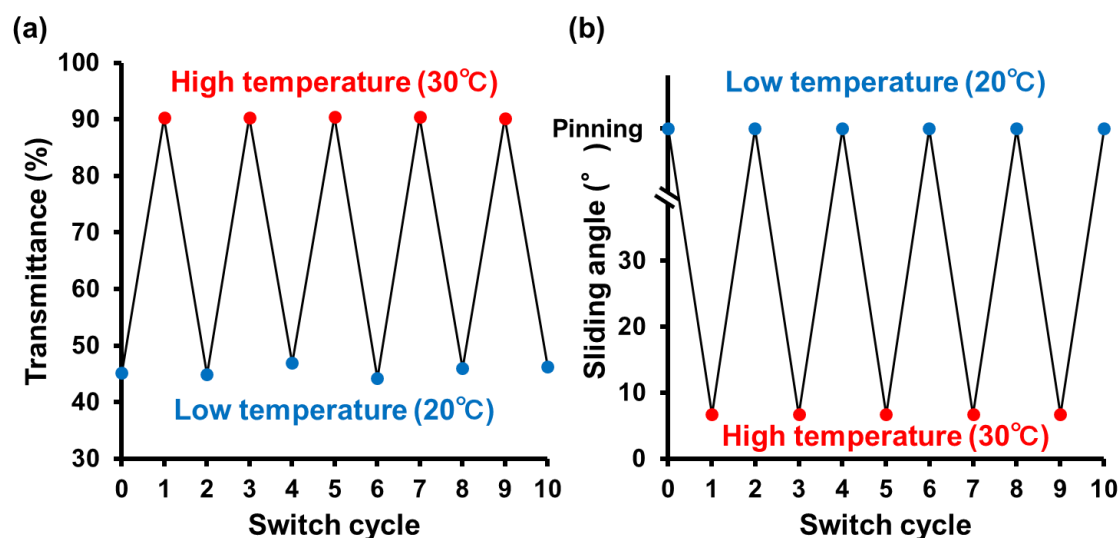


Figure 5-16. Repeated switching of the transparency (a) and attachment (b) of a 10 μL droplet of water on TA-SLIPS with 1:25 volume ratio at 30°C and 20°C. Reproduced with permission from Ref [147]. Copyright 2016 American Chemical Society.¹⁴⁷

5.4 Conclusions

TA-SLIPSs with a hydrophobized underlayer with porosity and a lubricant layer with paraffin mixture (solidifiable/liquid paraffin) were employed to develop multifunctional intelligent surfaces. The LbL self-assembly technique enabled the formation of the porous underlayer, giving rise to a nanofibrous membrane. It was possible to adjust the paraffin layer scattering factor and the thin film surface topography. At ambient temperature, these materials also displayed effective optical broadband transparency and wettability switching, both of which were amenable to adjustment. In solid state, the TA-SLIPSs trapped the water droplets, while the extensive light dispersal caused them to acquire opacity. In liquid state, by contrast, the TA-SLIPSs did not trap the water droplets and demonstrated diminished light dispersal. The ratio of solidifiable paraffin to liquid paraffin determined the transition temperature. Meanwhile, the light-transmission inhibitor in the lubricant layer suffered alterations in surface structure and size when the paraffin was in solid state. Hence, adjustment of the ratio of solidifiable to liquid paraffin enables regulation of droplet motion and light transmittance at various temperatures. Solid-to-liquid conversion ensures preservation of TA-SLIPS properties for extensive intervals, but they are disrupted by the sustained TA-SLIPS liquid state. Hence, further research is needed to elucidate mechanical properties and stability (e.g. weatherability and mechanical robustness). Anti-fouling applications could be improved and surfaces with adjustable optical transparency could be developed for use in novel medical applications and intelligent windows by designing and refining multifunctional systems with temperature dependence.

Chapter 6

Conclusion and Implications

6.1 Summary of findings

The present thesis demonstrated three functional SLIPS *via* LbL: the antireflection-SLIPS, the biocompatible antithrombogenic SLIPS, and the temperature-responsive SLIPS.

The antireflection-SLIPS has been demonstrated that light scattering at the long-wavelength side by Rayleigh scattering was circumvented by a slippery fluid-infused anti-reflective film comprising chitin nanofibres with a diameter smaller than 50 m, accomplishing transmittance in a proportion of 97.2%. The three distinct morphologies exhibited by films made of identical materials were superhydrophilicity with anti-reflection, superhydrophobicity and omniphobicity, and imitation of the biological structures of moth eyes, lotus leaves and pitcher plants. Research also evaluated how the films' property of frost formation prevention was affected by alterations in temperature and it was found that slippery fluid-infused antireflective films could prevent frost formation effectively.

Next, for the biocompatible antithrombogenic SLIPS, LbL underlayer based on biocompatible/biodegradable chitosan and alginate interacting electrostatically and hydrogen-bonding among alginate and polyvinylpyrrolidone (PVPON). Once chitosan and alginate were crosslinked, the pH was elevated to induce porosity from the hydrogen-bonding disintegration

and thus eliminate the PVPON. The underlayer displaying porosity was made hydrophobic and coated in almond oil demonstrating biocompatibility. Blood slid off this slippery liquid-infused porous surface demonstrating biodegradability and biocompatibility without difficulty and without staining. Furthermore, the material possesses environmental durability, has around 90% transmittance, and prevents clot formation. Hence, it constitutes a promising candidate for the cost-effective, sustainable and uncomplicated production of non-fouling medical devices.

As the temperature-responsive SLIPS, the temperature-activated solidifiable/liquid paraffin-infused porous surfaces (TA-SLIPSs) were achieved. The lubricant layer contains a light-transmission inhibitor that undergoes alterations in surface morphology and size when the paraffin solidifies. Consequently, the ratio of solidifiable paraffin to liquid paraffin determines the extent to which the droplet motion and light transmittance can be controlled at varying temperatures. These kinds of thermal-sensitive, multifunctional systems warrant more detailed investigation to contribute to anti-fouling applications and help create surfaces with adjustable optical transparency that could be used in such devices as smart windows and medical devices.

6.2 Future works

Several phenomena on SLIPS have not been fully revealed by this thesis, and some questions require further investigations to be resolved with more experimental effort. The following challenges should primarily be dealt with. At first, further optical enhancement of SLIPS should be processed. For instance, Infrared (IR) reflection underlayer easily generated by LbL will be applied to SLIPS to reflect target wavelength, which contributes to understanding the optical properties on SLIPS. The second challenge is applying responsive

underlayers to SLIPS. The present study demonstrated the responsive lubricant oil on the durable LbL films to control transparency and surface wettability. On the other hand, the responsive underlayers have potential abilities of precise regulation of optical properties and surface topography of SLIPS. For example, self-standing LbL underlayers with AR or IR reflection properties should achieve novel control method of optical transparency/reflection after elongated and contracted. The LbL films with humidity responsiveness should show the autonomic movement SLIPS with switching the wettability. Other functional underlayer such as conductive LbL films and responsive lubricant oil should lead the regulation of lubricant morphology.

In conclusion, the hydrophobic tailored nano-topography for SLIPS were achieved *via* LbL depending on intended applications, and these functional SLIPS would be valuable to solve various challenges, especially, in the areas of medical devices and energy management.

References

- (1) Lepora, N. F.; Verschure, P.; Prescott, T. J. The State of the Art in Biomimetics. *Bioinspir. Biomim.* **2013**, *8*, 13001.
- (2) Bhushan, B. Biomimetics: Lessons from Nature-an Overview. *Philos. Trans. A. Math. Phys. Eng. Sci.* **2009**, *367*, 1445–1486.
- (3) Sarikaya, M.; Tamerler, C.; Jen, A. K.-Y.; Schulten, K.; Baneyx, F. Molecular Biomimetics: Nanotechnology through Biology. *Nat. Mater.* **2003**, *2*, 577–585.
- (4) Sun, T.; Feng, L. I. N.; Gao, X.; Jiang, L. Bioinspired Surfaces with Special Wettability. *Acc. Chem. Res.* **2005**, *38*, 644–652.
- (5) Zhai, L.; Cebeci, F. C.; Cohen, R. E.; Rubner, M. F. Stable Superhydrophobic Coatings from Polyelectrolyte Multilayers. *Nano Lett.* **2004**, *4*, 1349–1353.
- (6) Miyauchi, Y.; Ding, B.; Shiratori, S. Fabrication of a Silver-Ragwort-Leaf-like Super-Hydrophobic Micro/nanoporous Fibrous Mat Surface by Electrospinning. *Nanotechnology* **2006**, *17*, 5151–5156.
- (7) Chung, K. K.; Schumacher, J. F.; Sampson, E. M.; Burne, R. A.; Antonelli, P. J.; Brennan, A. B. Impact of Engineered Surface Microtopography on Biofilm Formation of Staphylococcus Aureus. *Biointerphases* **2007**, *2*, 89–94.
- (8) Manabe, K.; Nishizawa, S.; Shiratori, S. Porous Surface Structure Fabricated by Breath Figures That Suppresses Pseudomonas Aeruginosa Biofilm Formation. *ACS Appl. Mater. Interfaces* **2013**, *5*, 11900–11905.
- (9) Huang, Y.-F.; Chattopadhyay, S.; Jen, Y.-J.; Peng, C.-Y.; Liu, T.-A.; Hsu, Y.-K.; Pan, C.-L.; Lo, H.-C.; Hsu, C.-H.; Chang, Y.-H.; *et al.* Improved Broadband and Quasi-Omnidirectional Anti-Reflection Properties with Biomimetic Silicon Nanostructures. *Nat. Nanotechnol.* **2007**, *2*, 770–774.

- (10) Forberich, K.; Dennler, G.; Scharber, M. C.; Hingerl, K.; Fromherz, T.; Brabec, C. J. Performance Improvement of Organic Solar Cells with Moth Eye Anti-Reflection Coating. *Thin Solid Films* **2008**, *516*, 7167–7170.
- (11) Hiller, J.; Mendelsohn, J. D.; Rubner, M. F. Reversibly Erasable Nanoporous Anti-Reflection Coatings from Polyelectrolyte Multilayers. *Nat. Mater.* **2002**, *1*, 59–63.
- (12) Parker, A. R.; Lawrence, C. R. Water Capture by a Desert Beetle. *Nature* **2001**, *414*, 33–34.
- (13) Zhai, L.; Berg, M. C.; Cebeci, F.; Kim, Y.; Milwid, J. M.; Rubner, M. F.; Cohen, R. E. Patterned Superhydrophobic Surfaces: Toward a Synthetic Mimic of the Namib Desert Beetle. *Nano Lett.* **2006**, *6*, 1213–1217.
- (14) Feng, X.; Jiang, L. Design and Creation of Superwetting/antiwetting Surfaces. *Adv. Mater.* **2006**, *18*, 3063–3078.
- (15) Autumn, K.; Liang, Y. A.; Hsieh, S. T.; Zesch, W.; Chan, W. P.; Kenny, T. W.; Fearing, R.; Full, R. J. Adhesive Force of a Single Gecko Foot-Hair. *Nature* **2000**, *405*, 681–685.
- (16) Ma, M.; Hill, R. M. Superhydrophobic Surfaces. *Curr. Opin. Colloid Interface Sci.* **2006**, *11*, 193–202.
- (17) Nishizawa, S.; Shiratori, S. Fabrication of Semi-Transparent Superoleophobic Thin Film by Nanoparticle-Based Nano-Microstructures on See-through Fabrics. *J. Mater. Sci.* **2013**, *48*, 6613–6618.
- (18) Nishizawa, S.; Shiratori, S. Water-Based Preparation of Highly Oleophobic Thin Films through Aggregation of Nanoparticles Using Layer-by-Layer Treatment. *Appl. Surf. Sci.* **2012**, *263*, 8–13.
- (19) Wang, F. J.; Lei, S.; Ou, J. F.; Xue, M. S.; Li, W. Superhydrophobic Surfaces with Excellent Mechanical Durability and Easy Repairability. *Appl. Surf. Sci.* **2013**, *276*, 397–400.

- (20) Bravo, J.; Zhai, L.; Wu, Z.; Cohen, R. E.; Rubner, M. F. Transparent Superhydrophobic Films Based on Silica Nanoparticles. *Langmuir* **2007**, *23*, 7293–7298.
- (21) Wong, T.; Sun, T.; Feng, L.; Aizenberg, J. Interfacial Materials with Special Wettability. *Mater. Res. Soc. Bull.* **2013**, *38*, 366–371.
- (22) Wong, T.-S.; Kang, S. H.; Tang, S. K. Y.; Smythe, E. J.; Hatton, B. D.; Grinthal, A.; Aizenberg, J. Bioinspired Self-Repairing Slippery Surfaces with Pressure-Stable Omniphobicity. *Nature* **2011**, *477*, 443–447.
- (23) Ma, W.; Higaki, Y.; Otsuka, H.; Takahara, A. Perfluoropolyether-Infused Nano-Texture: A Versatile Approach to Omniphobic Coatings with Low Hysteresis and High Transparency. *Chem. Commun.* **2013**, *49*, 597–599.
- (24) Kim, P.; Kreder, M. J.; Alvarenga, J.; Aizenberg, J. Hierarchical or Not? Effect of the Length Scale and Hierarchy of the Surface Roughness on Omniphobicity of Lubricant-Infused Substrates. *Nano Lett.* **2013**, *13*, 1793–1799.
- (25) Vogel, N.; Belisle, R. a; Hatton, B.; Wong, T.-S.; Aizenberg, J. Transparency and Damage Tolerance of Patternable Omniphobic Lubricated Surfaces Based on Inverse Colloidal Monolayers. *Nat. Commun.* **2013**, *4*, 2167.
- (26) Smith, J. D.; Dhiman, R.; Anand, S.; Reza-Garduno, E.; Cohen, R. E.; McKinley, G. H.; Varanasi, K. K. Droplet Mobility on Lubricant-Impregnated Surfaces. *Soft Matter* **2013**, *9*, 1772–1780.
- (27) Yao, X.; Hu, Y.; Grinthal, A.; Wong, T.-S.; Mahadevan, L.; Aizenberg, J. Adaptive Fluid-Infused Porous Films with Tunable Transparency and Wettability. *Nat. Mater.* **2013**, *12*, 529–534.
- (28) Hedrick, J. L.; Brown, K. A.; Kluender, E. J.; Cabezas, M. D.; Chen, P. C.; Mirkin, C. A. Hard Transparent Arrays for Polymer Pen Lithography. *ACS Nano* **2016**, *10*, 3144–3148.

- (29) Kim, J.; Staunton, J. R.; Tanner, K. Independent Control of Topography for 3D Patterning of the ECM Microenvironment. *Adv. Mater.* **2016**, *28*, 132–137.
- (30) Zhao, W.; Wang, L.; Xue, Q. Fabrication of Low and High Adhesion Hydrophobic Au Surfaces with Micro/nano-Biomimetic Structures. *J. Phys. Chem. C* **2010**, *114*, 11509–11514.
- (31) Søndergaard, T.; Novikov, S. M.; Holmgaard, T.; Eriksen, R. L.; Beermann, J.; Han, Z.; Pedersen, K.; Bozhevolnyi, S. I. Plasmonic Black Gold by Adiabatic Nanofocusing and Absorption of Light in Ultra-Sharp Convex Grooves. *Nat. Commun.* **2012**, *3*, 969.
- (32) Wang, H.; Goodrich, G. P.; Tam, F.; Oubre, C.; Nordlander, P.; Halas, N. J. Controlled Texturing Modifies the Surface Topography and Plasmonic Properties of Au Nanoshells. *J. Phys. Chem. B* **2005**, *109*, 11083–11087.
- (33) Vasquez, Y.; Kolle, M.; Mishchenko, L.; Hatton, B. D.; Aizenberg, J. Three-Phase Co-Assembly: In Situ Incorporation of Nanoparticles into Tunable, Highly Ordered, Porous Silica Films. *ACS Photonics* **2014**, *1*, 53–60.
- (34) Jun, I.; Chung, Y. W.; Heo, Y. H.; Han, H. S.; Park, J.; Jeong, H.; Lee, H.; Lee, Y. Bin; Kim, Y. C.; Seok, H. K.; *et al.* Creating Hierarchical Topographies on Fibrous Platforms Using Femtosecond Laser Ablation for Directing Myoblasts Behavior. *ACS Appl. Mater. Interfaces* **2016**, *8*, 3407–3417.
- (35) Passeri, D.; Tamburri, E.; Terranova, M. L.; Rossi, M. Polyaniline-Nanodiamond Fibers Resulting from the Self-Assembly of Nano-Fibrils: A Nanomechanical Study. *Nanoscale* **2015**, *7*, 14358–14367.
- (36) Huang, X.; Sun, Y.; Soh, S. Stimuli-Responsive Surfaces for Tunable and Reversible Control of Wettability. *Adv. Mater.* **2015**, *27*, 4062–4068.
- (37) Seo, S.; Lee, J.; Kwon, M. S.; Seo, D.; Kim, J. Stimuli-Responsive Matrix-Assisted Colorimetric Water Indicator of Polydiacetylene Nanofibers. *ACS Appl. Mater. Interfaces* **2015**, *7*, 20342–20348.

- (38) Decher, G. Fuzzy Nanoassemblies: Toward Layered Polymeric Multicomposites. *Science* (80-.). **1997**, *277*, 1232–1237.
- (39) Shiratori, S. S.; Rubner, M. F. pH-Dependent Thickness Behavior of Sequentially Adsorbed Layers of Weak Polyelectrolytes. *Macromolecules* **2000**, *33*, 4213–4219.
- (40) Wang, Y.; Angelatos, A. S.; Caruso, F. Template Synthesis of Nanostructured Materials via Layer-by-Layer Assembly. *Chem. Mater.* **2008**, *20*, 848–858.
- (41) Yang, S.; Zhang, Y.; Zhang, X.; Xu, J. The Influence of pH on a Hydrogen-Bonded Assembly Film. *Soft Matter* **2007**, *3*, 463–469.
- (42) Stockton, W. B.; Rubner, M. F. Molecular-Level Processing of Conjugated Polymers. 4. Layer-by-Layer Manipulation of Polyaniline via Hydrogen-Bonding Interactions. *Macromolecules* **1997**, *30*, 2717–2725.
- (43) Wang, L.; Wang, Z.; Zhang, X.; Shen, J.; Chi, L.; Fuchs, H. A New Approach for the Fabrication of an Alternating Multilayer Film of poly(4-Vinylpyridine) and Poly(acrylic Acid) Based on Hydrogen Bonding. *Macromol. Rapid Commun.* **1997**, *18*, 509–514.
- (44) Zhang, Y.; Guan, Y.; Yang, S.; Xu, J.; Han, C. C. Fabrication of Hollow Capsules Based on Hydrogen Bonding. *Adv. Mater.* **2003**, *15*, 832–835.
- (45) Kharlampieva, E.; Sukhishvili, S. A. Hydrogen-Bonded Layer-by-Layer Polymer Films. *J. Macromol. Sci. Part C Polym. Rev.* **2006**, *46*, 377–395.
- (46) Städler, B.; Price, A. D.; Chandrawati, R.; Hosta-Rigau, L.; Zelikin, A. N.; Caruso, F. Polymer Hydrogel Capsules: En Route toward Synthetic Cellular Systems. *Nanoscale* **2009**, *1*, 68–73.
- (47) Sukhishvili, S. A.; Granick, S. Layered, Erasable Polymer Multilayers Formed by Hydrogen-Bonded Sequential Self-Assembly. *Macromolecules* **2002**, *35*, 301–310.
- (48) Li, Q.; Quinn, J. F.; Caruso, F. Nanoporous Polymer Thin Films via Polyelectrolyte Templating. *Adv. Mater.* **2005**, *17*, 2058–2062.

- (49) Zhu, Z.; Sukhishvili, S. A. Temperature-Induced Swelling and Small Molecule Release with Hydrogen-Bonded Multilayers of Block Copolymer Micelles. *ACS Nano* **2009**, *3*, 3595–3605.
- (50) Kharlampieva, E.; Koziovskaia, V.; Sukhishvili, S. A. Layer-by-Layer Hydrogen-Bonded Polymer Films: From Fundamentals to Applications. *Adv. Mater.* **2009**, *21*, 3053–3065.
- (51) Kim, B. S.; Park, S. W.; Hammond, P. T. Hydrogen-Bonding Layer-by-Layer-Assembled Biodegradable Polymeric Micelles as Drug Delivery Vehicles from Surfaces. *ACS Nano* **2008**, *2*, 386–392.
- (52) Schmidt, D. J.; Hammond, P. T. Electrochemically Erasable Hydrogen-Bonded Thin Films. *Chem. Commun.* **2010**, *46*, 7358–7360.
- (53) Meng, F.; Zhong, Z.; Feijen, J. Stimuli-Responsive Polymersomes for Programmed Drug Delivery. *Biomacromolecules* **2009**, *10*, 197–209.
- (54) Zelikin, A. N.; Quinn, J. F.; Caruso, F. Disulfide Cross-Linked Polymer Capsules: En Route to Biodeconstructible Systems. *Biomacromolecules* **2006**, *7*, 27–30.
- (55) Zelikin, A. N.; Li, Q.; Caruso, F. Degradable Polyelectrolyte Capsules Filled with Oligonucleotide Sequences. *Angew. Chemie - Int. Ed.* **2006**, *45*, 7743–7745.
- (56) Zhao, N.; Shi, F.; Wang, Z.; Zhang, X. Combining Layer-by-Layer Assembly with Electrodeposition of Silver Aggregates for Fabricating Superhydrophobic Surfaces. *Langmuir* **2005**, *21*, 4713–4716.
- (57) Choi, J.; Rubner, M. F. Influence of the Degree of Ionization on Weak Polyelectrolyte Multilayer Assembly. *Macromolecules* **2005**, *38*, 116–124.
- (58) Krogman, K. C.; Cohen, R. E.; Hammond, P. T.; Rubner, M. F.; Wang, B. N. Industrial-Scale Spray Layer-by-Layer Assembly for Production of Biomimetic Photonic Systems. *Bioinspir. Biomim.* **2013**, *8*, 1–11.

- (59) Becker, A. L.; Johnston, A. P. R.; Caruso, F. Layer-by-Layer-Assembled Capsules and Films for Therapeutic Delivery. *Small* **2010**, *6*, 1836–1852.
- (60) Ding, C.; Xu, S.; Lin, J.; Hu, X.; Jian, W.; Wang, J.; Ma, J.; Feng, S. Controlled Loading and Release of Methylene Blue for Hydrogen-Bonded LbL Poly(vinyl Pyrrolidone)/poly (Acrylic Acid) Film. *J. Polym. Res.* **2012**, *19*, 9817.
- (61) Zhang, W.; Zhang, A.; Guan, Y.; Zhang, Y.; Zhu, X. X. Silver-Loading in Uncrosslinked Hydrogen-Bonded LBL Films: Structure Change and Improved Stability. *J. Mater. Chem.* **2011**, *21*, 548–555.
- (62) Leung, M. K. M.; Such, G. K.; Johnston, A. P. R.; Biswas, D. P.; Zhu, Z.; Yan, Y.; Lutz, J. F.; Caruso, F. Assembly and Degradation of Low-Fouling Click-Functionalized Poly(ethylene Glycol)-Based Multilayer Films and Capsules. *Small* **2011**, *7*, 1075–1085.
- (63) Quinn, J. F.; Caruso, F. Facile Tailoring of Film Morphology and Release Properties Using Layer-by-Layer Assembly of Thermoresponsive Materials. *Langmuir* **2004**, *20*, 20–22.
- (64) Johnston, A. P. R.; Caruso, F. Exploiting the Directionality of DNA: Controlled Shrinkage of Engineered Oligonucleotide Capsules. *Angew. Chemie - Int. Ed.* **2007**, *46*, 2677–2680.
- (65) Yang, S. Y.; Lee, D.; Cohen, R. E.; Rubner, M. F. Bioinert Solution-Cross-Linked Hydrogen-Bonded Multilayers on Colloidal Particles. *Langmuir* **2004**, *20*, 5978–5981.
- (66) Kozlovskaya, V.; Ok, S.; Sousa, A.; Libera, M.; Sukhishvili, S. A. Hydrogen-Bonded Polymer Capsules Formed by Layer-by-Layer Self-Assembly. *Macromolecules* **2003**, *36*, 8590–8592.
- (67) Pillai, O.; Panchagnula, R. Polymers in Drug Delivery. *Curr. Opin. Chem. Biol.* **2001**, *5*, 447–451.

- (68) Kozlovskaya, V.; Shamaev, A.; Sukhishvili, S. A. Tuning Swelling pH and Permeability of Hydrogel Multilayer Capsules. *Soft Matter* **2008**, *4*, 1499–1507.
- (69) Elsner, N.; Kozlovskaya, V.; Sukhishvili, S. A.; Fery, A.; Antipov, A. A.; Sukhorukov, G. B.; Sukhorukov, G. B.; Donath, E.; Moya, S.; Susa, A.; *et al.* pH-Triggered Softening of Crosslinked Hydrogen-Bonded Capsules. *Soft Matter* **2006**, *2*, 966–972.
- (70) Du, Y.; Luna, L. E.; Tan, W. S.; Rubner, M. F.; Cohen, R. E. Hollow Silica Nanoparticles in UV-Visible Antireflection Coatings for Poly(methyl Methacrylate) Substrates. *ACS Nano* **2010**, *4*, 4308–4316.
- (71) Podsiadlo, P.; Sui, L.; Elkasabi, Y.; Burgardt, P.; Lee, J.; Miryala, A.; Kusumaatmaja, W.; Carman, M. R.; Shtein, M.; Kieffer, J.; *et al.* Layer-by-Layer Assembled Films of Cellulose Nanowires with Antireflective Properties. *Langmuir* **2007**, *23*, 7901–7906.
- (72) Huang, X.; Chrisman, J. D.; Zacharia, N. S. Omniphobic Slippery Coatings Based on Lubricant-Infused Porous Polyelectrolyte Multilayers. *ACS Macro Lett.* **2013**, *2*, 826–829.
- (73) Mendelsohn, J. D.; Barrett, C. J.; Chan, V. V.; Pal, A. J.; Mayes, A. M.; Rubner, M. F. Fabrication of Microporous Thin Films from Polyelectrolyte Multilayers. *Langmuir* **2000**, *16*, 5017–5023.
- (74) Tsuge, Y.; Moriya, T.; Shiratori, S. Porous Transition of Polyelectrolyte Film through Reaction-Induced Phase Separation Caused by Interaction with Specific Metal Ions. *Langmuir* **2016**, *32*, 7219–7227.
- (75) Nuraje, N.; Asmatulu, R.; Cohen, R. E.; Rubner, M. F. Durable Antifog Films from Layer-by-Layer Molecularly Blended Hydrophilic Polysaccharides. *Langmuir* **2011**, *27*, 782–791.
- (76) Wang, Y.; Li, T.; Li, S.; Sun, J. Antifogging and Frost-Resisting Polyelectrolyte Coatings Capable of Healing Scratches and Restoring Transparency. *Chem. Mater.* **2015**, *acs.chemmater.5b03705*.

- (77) Krasowska, M.; Zawala, J.; Malysa, K. Air at Hydrophobic Surfaces and Kinetics of Three Phase Contact Formation. *Adv. Colloid Interface Sci.* **2009**, *147–148*, 155–169.
- (78) Nakajima, A. Design of Hydrophobic Surfaces for Liquid Droplet Control. *NPG Asia Mater.* **2011**, *3*, 49–56.
- (79) Cassie, A. B. D.; Baxter, S. Wettability of Porous Surfaces. *Trans. Faraday Soc.* **1944**, *40*, 546–551.
- (80) Nosonovsky, M.; Bhushan, B. Roughness Optimization for Biomimetic Superhydrophobic Surfaces. *Microsyst. Technol.* **2005**, *11*, 535–549.
- (81) Burton, Z.; Bhushan, B. Surface Characterization and Adhesion and Friction Properties of Hydrophobic Leaf Surfaces. *Ultramicroscopy* **2006**, *106*, 709–719.
- (82) Jung, Y. C.; Bhushan, B. Contact Angle, Adhesion and Friction Properties of Micro- and Nanopatterned Polymers for Superhydrophobicity. *Nanotechnology* **2006**, *17*, 4970–4980.
- (83) Liu, Y.; Chen, X.; Xin, J. H. Hydrophobic Duck Feathers and Their Simulation on Textile Substrates for Water Repellent Treatment. *Bioinspir. Biomim.* **2008**, *3*, 46007.
- (84) Sahoo, B. N.; Kandasubramanian, B. Recent Progress in Fabrication and Characterisation of Hierarchical Biomimetic Superhydrophobic Structures. *RSC Adv.* **2014**, *4*, 22053–22093.
- (85) Quéré, D. Non-Sticking Drops. *Reports Prog. Phys.* **2005**, *68*, 2495–2532.
- (86) Bonn, D.; Eggers, J.; Indekeu, J.; Meunier, J. Wetting and Spreading. *Rev. Mod. Phys.* **2009**, *81*, 739–805.
- (87) Zhang, J.; Wu, L.; Li, B.; Li, L.; Seeger, S.; Wang, A. Evaporation-Induced Transition from Nepenthes Pitcher-Inspired Slippery Surfaces to Lotus Leaf-Inspired Superoleophobic Surfaces. *Langmuir* **2014**, *30*, 14292–14299.

- (88) Gao, X.; Yan, X.; Yao, X.; Xu, L.; Zhang, K.; Zhang, J.; Yang, B.; Jiang, L. The Dry-Style Antifogging Properties of Mosquito Compound Eyes and Artificial Analogues Prepared by Soft Lithography. *Adv. Mater.* **2007**, *19*, 2213–2217.
- (89) Kim, P.; Wong, T.; Alvarenga, J.; Kreder, M. J.; Adorno-Martinez, W. E.; Aizenberg, J. Liquid-Infused Nanostructured Surfaces with Extreme Anti-Ice and Anti-Frost Performance. *ACS Nano* **2012**, *6*, 6569–6577.
- (90) Clapham, P. B.; Hutley, M. C. Reduction of Lens Reflexion by the “Moth Eye” Principle. *Nature* **1973**, *244*, 281–282.
- (91) Koo, H. Y.; Yi, D. K.; Yoo, S. J.; Kim, D.-Y. A Snowman-like Array of Colloidal Dimers for Antireflecting Surfaces. *Adv. Mater.* **2004**, *16*, 274–277.
- (92) Lvov, Y.; Decher, G.; Möhwald, H. Assembly, Structural Characterization, and Thermal Behavior of Layer-by-Layer Deposited Ultrathin Films of Poly(vinyl Sulfate) and Poly(allylamine). *Langmuir* **1993**, *9*, 481–486.
- (93) Matsuda, M.; Shiratori, S. Correlation of Antithrombogenicity and Heat Treatment for Layer-by-Layer Self-Assembled Polyelectrolyte Films. *Langmuir* **2011**, *27*, 4271–4277.
- (94) Lvov, Y.; Ariga, K.; Ichinose, I.; Kunitake, T. Assembly of Multicomponent Protein Films by Means of Electrostatic Layer-by-Layer Adsorption. *J. Am. Chem. Soc.* **1995**, *117*, 6117–6123.
- (95) Lu, Y.; Choi, Y. J.; Lim, H. S.; Kwak, D.; Shim, C.; Lee, S. G.; Cho, K. pH-Induced Antireflection Coatings Derived from Hydrogen-Bonding-Directed Multilayer Films. *Langmuir* **2010**, *26*, 17749–17755.
- (96) Zhang, L.; Sun, J. Layer-by-Layer Codeposition of Polyelectrolyte Complexes and Free Polyelectrolytes for the Fabrication of Polymeric Coatings. *Macromolecules* **2010**, *43*, 2413–2420.

- (97) Yuan, W.; Li, C. M. Exponentially Growing Layer-by-Layer Assembly to Fabricate pH-Responsive Hierarchical Nanoporous Polymeric Film and Its Superior Controlled Release Performance. *Chem. Commun.* **2010**, *46*, 9161–9163.
- (98) Nogueira, G. M.; Swiston, A. J.; Beppu, M. M.; Rubner, M. F. Layer-by-Layer Deposited Chitosan/silk Fibroin Thin Films with Anisotropic Nanofiber Alignment. *Langmuir* **2010**, *26*, 8953–8958.
- (99) Shimomura, H.; Gemici, Z.; Cohen, R. E.; Rubner, M. F. Layer-by-Layer-Assembled High-Performance Broadband Antireflection Coatings. *ACS Appl. Mater. Interfaces* **2010**, *2*, 813–820.
- (100) Qi, Z. D.; Saito, T.; Fan, Y.; Isogai, A. Multifunctional Coating Films by Layer-by-Layer Deposition of Cellulose and Chitin Nanofibrils. *Biomacromolecules* **2012**, *13*, 553–558.
- (101) Kim, J. H.; Fujita, S.; Shiratori, S. Design of a Thin Film for Optical Applications, Consisting of High and Low Refractive Index Multilayers, Fabricated by a Layer-by-Layer Self-Assembly Method. *Colloids Surfaces A Physicochem. Eng. Asp.* **2006**, *284–285*, 290–294.
- (102) Okada, I.; Shiratori, S. High-Transparency, Self-Standable Gel-SLIPS Fabricated by a Facile Nanoscale Phase Separation. *ACS Appl. Mater. Interfaces* **2014**, *6*, 1502–1508.
- (103) Li, Y.; Chen, S.; Wu, M.; Sun, J. Polyelectrolyte Multilayers Impart Healability to Highly Electrically Conductive Films. *Adv. Mater.* **2012**, *24*, 4578–4582.
- (104) Ma, Y.; Zhang, Y.; Wu, B.; Sun, W.; Li, Z.; Sun, J. Polyelectrolyte Multilayer Films for Building Energetic Walking Devices. *Angew. Chemie - Int. Ed.* **2011**, *50*, 6254–6257.
- (105) Ma, Y.; Sun, J. Humido- and Thermo-Responsive Free-Standing Films Mimicking the Petals of the Morning Glory Flower. *Chem. Mater.* **2009**, *21*, 898–902.

- (106) Manabe, K.; Nishizawa, S.; Kyung, K. H.; Shiratori, S. Optical Phenomena and Antifrosting Property on Biomimetics Slippery Fluid-Infused Antireflective Films via Layer-by-Layer Comparison with Superhydrophobic and Antireflective Films. *ACS Appl. Mater. Interfaces* **2014**, *6*, 13985–13993.
- (107) Ifuku, S.; Nogi, M.; Abe, K.; Yoshioka, M.; Morimoto, M.; Saimoto, H.; Yano, H. Preparation of Chitin Nanofibers with a Uniform Width as α -Chitin from Crab Shells. *Biomacromolecules* **2009**, *10*, 1584–1588.
- (108) Gopalan Nair, K.; Dufresne, A. Crab Shell Chitin Whisker Reinforced Natural Rubber Nanocomposites. 1. Processing and Swelling Behavior. *Biomacromolecules* **2003**, *4*, 657–665.
- (109) Fan, Y.; Saito, T.; Isogai, A. Individual Chitin Nano-Whiskers Prepared from Partially Deacetylated α -Chitin by Fibril Surface Cationization. *Carbohydr. Polym.* **2010**, *79*, 1046–1051.
- (110) Tan, W. S.; Du, Y.; Luna, L. E.; Khitass, Y.; Cohen, R. E.; Rubner, M. F. Templated Nanopores for Robust Functional Surface Porosity in Poly(methyl Methacrylate). *Langmuir* **2012**, *28*, 13496–13502.
- (111) Whyman, G.; Bormashenko, E. How to Make the Cassie Wetting State Stable? *Langmuir* **2011**, *27*, 8171–8176.
- (112) Eastman, J.; Bausmeister, P. The Microstructure of Polished Optical Surfaces. *Opt. Commun.* **1974**, *12*, 418–420.
- (113) Arnon, O. Loss Mechanisms in Dielectric Optical Interference Devices. *Appl. Opt.* **1977**, *16*, 2147–2151.
- (114) Bennett, H. E.; Porteus, J. O. Relation Between Surface Roughness and Specular Reflectance at Normal Incidence. *J. Opt. Soc. Am.* **1961**, *51*, 123–129.
- (115) Carniglia, C. K. Scalar Scattering Theory for Multilayer Optical Coatings. *Opt. Eng.* **1979**, *18*, 104–115.

- (116) Rönnow, D.; Roos, A. Diffuse Reflectance and Transmittance Spectra of an Interference Layer. 2. Evaluation of Tin Oxide-Coated Glass. *Appl. Opt.* **1994**, *33*, 7918–7927.
- (117) Kelly, K. L.; Coronado, E.; Zhao, L. L.; Schatz, G. C. The Optical Properties of Metal Nanoparticles: The Influence of Size, Shape, and Dielectric Environment. *J. Phys. Chem. B* **2003**, *107*, 668–677.
- (118) Cebeci, F. Ç.; Wu, Z.; Zhai, L.; Cohen, R. E.; Rubner, M. F. Nanoporosity-Driven Superhydrophilicity: A Means to Create Multifunctional Antifogging Coatings. *Langmuir* **2006**, *22*, 2856–2862.
- (119) Prevedello, D. M.; Doglietto, F.; Jane, J. a.; Jagannathan, J.; Han, J.; Laws, E. R. History of Endoscopic Skull Base Surgery: Its Evolution and Current Reality. *J. Neurosurg.* **2007**, *107*, 206–213.
- (120) Harrel, S. K.; Wilson, T. G.; Rivera-Hidalgo, F. A Videoscope for Use in Minimally Invasive Periodontal Surgery. *J. Clin. Periodontol.* **2013**, *40*, 868–874.
- (121) Kalra, G.; Keir, J.; Tahery, J. Prevention of Blood Staining of Endoscope Tip during Functional Endoscopic Sinus Surgery: Sleeve Technique. *J. Laryngol. Otol.* **2009**, *123*, 1358–1359.
- (122) Hennequin, L. M.; Joffre, F. G.; Rousseau, H. P.; Aziza, R.; Tregant, P.; Bernadet, P.; Salvador, M.; Chamontin, B. Renal Artery Stent Placement: Long-Term Results with the Wallstent Endoprosthesis. *Radiology* **1994**, *191*, 713–719.
- (123) Deconinck, E.; Sohier, J.; Scheerder, I. D. E.; Mooter, G. V. A. N. D. E. N. Pharmaceutical Aspects of Drug Eluting Stents. *J. Pharm. Sci.* **2008**, *97*, 5047–5060.
- (124) Sunny, S.; Vogel, N.; Howell, C.; Vu, T. L.; Aizenberg, J. Lubricant-Infused Nanoparticulate Coatings Assembled by Layer-by-Layer Deposition. *Adv. Funct. Mater.* **2014**, *24*, 6658–6667.

- (125) Wilson, P. W.; Lu, W.; Xu, H.; Kim, P.; Kreder, M. J.; Alvarenga, J.; Aizenberg, J. Inhibition of Ice Nucleation by Slippery Liquid-Infused Porous Surfaces (SLIPS). *Phys. Chem. Chem. Phys.* **2013**, *15*, 581–585.
- (126) Li, J.; Kleintschek, T.; Rieder, A.; Cheng, Y.; Baumbach, T.; Obst, U.; Schwartz, T.; Levkin, P. A. Hydrophobic Liquid-Infused Porous Polymer Surfaces for Antibacterial Applications. *ACS Appl. Mater. Interfaces* **2013**, *5*, 6704–6711.
- (127) Xiao, L.; Li, J.; Mieszkina, S.; Di Fino, A.; Clare, A. S.; Callow, M. E.; Callow, J. A.; Grunze, M.; Rosenhahn, A.; Levkin, P. A. Slippery Liquid-Infused Porous Surfaces Showing Marine Antibiofouling Properties. *ACS Appl. Mater. Interfaces* **2013**, *5*, 10074–10080.
- (128) Shenoy, D. B.; Antipov, A. A.; Sukhorukov, G. B.; Möhwald, H. Layer-by-Layer Engineering of Biocompatible, Decomposable Core–Shell Structures. *Biomacromolecules* **2003**, *4*, 265–272.
- (129) Alegre, M.; Garcés, J. R.; Puig, L. Bone Wax in Dermatologic Surgery. *Actas Dermosifiliográficas (English Ed.)* **2013**, *104*, 299–303.
- (130) Elder, R. L. The Cosmetic Ingredient Review—a Safety Evaluation Program. *J. Am. Acad. Dermatol.* **1984**, *11*, 1168–1174.
- (131) Choi, A. L.; Sun, G.; Zhang, Y.; Grandjean, P. Developmental Fluoride Neurotoxicity: A Systematic Review and Meta-Analysis. *Environ. Health Perspect.* **2012**, *120*, 1362–1368.
- (132) Manabe, K.; Kyung, K.-H.; Shiratori, S. Biocompatible Slippery Fluid-Infused Films Composed of Chitosan and Alginate via Layer-by-Layer Self-Assembly and Their Antithrombogenicity. *ACS Appl. Mater. Interfaces* **2015**, *7*, 4763–4771.
- (133) Wang, B. L.; Ren, K. F.; Chang, H.; Wang, J. L.; Ji, J. Construction of Degradable Multilayer Films for Enhanced Antibacterial Properties. *ACS Appl. Mater. Interfaces* **2013**, *5*, 4136–4143.

- (134) Guo, P.; Zheng, Y.; Wen, M.; Song, C.; Lin, Y.; Jiang, L. Icephobic/anti-Icing Properties of Micro/nanostructured Surfaces. *Adv. Mater.* **2012**, *24*, 2642–2648.
- (135) Leslie, D. C.; Waterhouse, A.; Berthet, J. B.; Valentin, T. M.; Watters, A. L.; Jain, A.; Kim, P.; Hatton, B. D.; Nedder, A.; Donovan, K.; *et al.* A Bioinspired Omniphobic Surface Coating on Medical Devices Prevents Thrombosis and Biofouling. *Nat. Biotechnol.* **2014**, *32*, 1134–1140.
- (136) Mandl, J.; Tanács, B.; Spolarics, Z.; Garzó, T.; Mucha, I.; Antoni, F.; Machovich, R.; Horváth, I. Uptake of Arachidonic Acid, Arachidic Acid, Oleic Acid and Their Incorporation into Phospholipids and Triacylglycerols of Isolated Murine Hepatocytes. Effect of Thrombin-Antithrombin III Complex. *Thromb. Res.* **1984**, *35*, 407–414.
- (137) Ros, E.; Mataix, J. Fatty Acid Composition of Nuts – Implications for Cardiovascular Health. *Br. J. Nutr.* **2006**, *96*, S29–S35.
- (138) Qing, G.; Sun, T. Chirality-Triggered Wettability Switching on a Smart Polymer Surface. *Adv. Mater.* **2011**, *23*, 1615–1620.
- (139) Li, J.; Li, L.; Du, X.; Feng, W.; Welle, A.; Trapp, O.; Grunze, M.; Hirtz, M.; Levkin, P. A. Reactive Superhydrophobic Surface and Its Photoinduced Disulfide-Ene and Thiol-Ene (Bio)functionalization. *Nano Lett.* **2015**, *15*, 675–681.
- (140) Fulghum, T. M.; Estillore, N. C.; Vo, C. D.; Armes, S. P.; Advincula, R. C. Stimuli-Responsive Polymer Ultrathin Films with a Binary Architecture: Combined Layer-by-Layer Polyelectrolyte and Surface-Initiated Polymerization Approach. *Macromolecules* **2008**, *41*, 429–435.
- (141) Urata, C.; Dunderdale, G. J.; England, M. W.; Hozumi, A. Self-Lubricating Organogels (SLUGs) with Exceptional Syneresis-Induced Anti-Sticking Properties against Viscous Emulsions and Ices. *J. Mater. Chem. A* **2015**, *3*, 12626–12630.

- (142) Hou, X.; Hu, Y.; Grinthal, A.; Khan, M.; Aizenberg, J. Liquid-Based Gating Mechanism with Tunable Multiphase Selectivity and Antifouling Behaviour. *Nature* **2015**, *519*, 70–73.
- (143) Wang, J.; Kato, K.; Blois, A. P.; Wong, T. S. Bioinspired Omniphobic Coatings with a Thermal Self-Repair Function on Industrial Materials. *ACS Appl. Mater. Interfaces* **2016**, *8*, 8265–8271.
- (144) Yao, X.; Ju, J.; Yang, S.; Wang, J.; Jiang, L. Temperature-Driven Switching of Water Adhesion on Organogel Surface. *Adv. Mater.* **2014**, *26*, 1895–1900.
- (145) Su, B.; Tian, Y.; Jiang, L. Bioinspired Interfaces with Superwettability: From Materials to Chemistry. *J. Am. Chem. Soc.* **2016**, *138*, 1727–1748.
- (146) Kreder, M. J.; Alvarenga, J.; Kim, P.; Aizenberg, J. Design of Anti-Icing Surfaces: Smooth, Textured or Slippery? *Nat. Rev. Mater.* **2016**, *1*, 15003.
- (147) Manabe, K.; Matsubayashi, T.; Tenjimayashi, M.; Moriya, T.; Tsuge, Y.; Kyung, K. H.; Shiratori, S. Controllable Broadband Optical Transparency and Wettability Switching of Temperature-Activated Solid/Liquid-Infused Nanofibrous Membranes. *ACS Nano* **2016**, *10*, 9387–9396.
- (148) Dai, X.; Stogin, B. B.; Yang, S.; Wong, T. S. Slippery Wenzel State. *ACS Nano* **2015**, *9*, 9260–9267.
- (149) Bhushan, B.; Jung, Y. C.; Koch, K. Micro-, Nano- and Hierarchical Structures for Superhydrophobicity, Self-Cleaning and Low Adhesion. *Philos. Trans. A. Math. Phys. Eng. Sci.* **2009**, *367*, 1631–1672.
- (150) Wang, L.; Zhao, Y.; Tian, Y.; Jiang, L. A General Strategy for the Separation of Immiscible Organic Liquids by Manipulating the Surface Tensions of Nanofibrous Membranes. *Angew. Chemie - Int. Ed.* **2015**, *54*, 14732–14737.

- (151) Roos, A.; R{nnow, D. Diffuse Reflectance and Transmittance Spectra of an Interference Layer: 1. Model Formulation and Properties. *Appl. Opt.* **1994**, *33*, 7908–7917.
- (152) Yamaguchi, T.; Tamura, H.; Taga, S.; Tsuchiya, S. Interfacial Optical Absorption in TiO₂–SiO₂ Multilayer Coatings Prepared by Rf Magnetron Sputtering. *Appl. Opt.* **1986**, *25*, 2703–2706.
- (153) Wong, W. S. Y.; Gutruf, P.; Sriram, S.; Bhaskaran, M.; Wang, Z.; Tricoli, A. Strain Engineering of Wave-like Nanofibers for Dynamically Switchable Adhesive/Repulsive Surfaces. *Adv. Funct. Mater.* **2016**, *26*, 399–407.
- (154) Kim, D.; Seo, J.; Shin, S.; Lee, S.; Lee, K.; Cho, H.; Shim, W.; Lee, H. B. R.; Lee, T. Reversible Liquid Adhesion Switching of Superamphiphobic Pd-Decorated Ag Dendrites via Gas-Induced Structural Changes. *Chem. Mater.* **2015**, *27*, 4964–4971.
- (155) Ge, D.; Lee, E.; Yang, L.; Cho, Y.; Li, M.; Gianola, D. S.; Yang, S. A Robust Smart Window: Reversibly Switching from High Transparency to Angle-Independent Structural Color Display. *Adv. Mater.* **2015**, *27*, 2489–2495.